PHYSIK-DEPARTMENT

On-Surface Synthesis of Two-Dimensional Organic Nanostructures

Dissertation

von

Johanna Elisabeth Eichhorn

TECHNISCHE UNIVERSITÄT
MÜNCHEN

Technische Universität München
Fakultät für Physik
Oskar-von-Miller Lehrstuhl für Wissenschaftskommunikation

On-Surface Synthesis of Two-Dimensional Organic Nanostructures

Johanna Elisabeth Eichhorn

Vollständiger Abdruck der von der Fakultät für Physik der Technischen Universität München zur Erlangung des akademischen Grades eines

Doktors der Naturwissenschaften
(Dr. rer. nat.)

genehmigten Dissertation.

Vorsitzender: Univ.-Prof. Dr. Martin Zacharias

Prüfer der Dissertation:

1. Priv.-Doz. Dr. Markus Lackinger
2. Univ.-Prof. Dr. Alexander Holleitner

Die Dissertation wurde am 03.11.2014 bei der Technischen Universität München eingereicht und durch die Fakultät für Physik am 08.01.2015 angenommen.

Abstract

The synthesis of two-dimensional organic nanostructures on metal surfaces is studied under ultra-high vacuum conditions. Scanning tunneling microscopy and X-ray photoelectron spectroscopy are used for characterization, allowing complementary analysis of molecular structures and chemical states. The surface-supported nanostructures are synthesized by means of molecular self-assembly and on-surface polymerization, resulting in the formation of non-covalent and covalent assemblies, respectively.
A systematic series of coexisting porous structures is obtained by self-assembly of triply amino substituted heptazine rings (melem). All polymorphs can be described by only two distinct binding motifs. The origin of the polymorphism is attributed to relatively strong molecule–substrate interactions arising from the large heptazine backbone and the greater versatility of large molecules as melem to form various different intermolecular interactions.
For on-surface polymerization of covalent nanostructures different coupling reactions, substrate materials, and reaction parameters are investigated. Coupling of terminal alkynes has the advantage to release either hydrogen or no byproduct at all, whereby the surface is not contaminated by adsorbing byproducts. On Cu(111), however, a variety of different reaction pathways is observed without a clear preference for a specific coupling reaction. On Cu(111) it is not possible to improve the selectivity of the diethynylbenzene polymerization by variation of the reaction parameters.
In surface-assisted Ullmann coupling on metal substrates, halogen atoms are split off from the molecular precursor and adsorb on the surfaces. In a subsequent coupling step, the dehalogenated molecules interlink *via* covalent bonds to 2D networks. The kinetically controlled polymerization results in the formation of covalent networks with high defect densities. On Au(111) direct and hierarchical polymerization are studied using an aromatic precursor functionalized with both iodine and bromine. The network quality can be improved by optimizing different reaction parameters such as substrate temperature, heating rate, or deposition rate, respectively.
In contrast to Au(111), Ullmann coupling on Ag(111) results in covalent networks with a higher degree of regularity. The main difference is attributed to the occurrence of metastable intermediates based on reversible organometallic bonds. The temperature for the formation of organometallic intermediates is lower than the temperature required for the conversion into covalent networks. This characteristic opens up the possibility of employing self-assembly and error correction of organometallic networks prior to covalent coupling for improving the network qualities.

Zusammenfassung

Die Synthese von zweidimensionalen, organischen Nanostrukturen auf Metalloberflächen wird unter Ultrahochvakuum-Bedingungen untersucht. Die Charakterisierung erfolgt mittels Rastertunnelmikroskopie und Röntgenphotoelektronenspektroskopie zur komplementären Analyse von Struktur und chemischer Zusammensetzung. Auf Oberflächen können sowohl kovalente Netzwerke durch Polymerisation als auch nichtkovalent gebundene Strukturen mittels Selbstassemblierung synthetisiert werden.
Eine systematische Abfolge koexistierender, poröser Strukturen wird bei Selbstassemblierung von Melem beobachtet, einem amino-funktionalisierten Heptazin-Ring. Alle Polymorphe können durch nur zwei verschiedene Bindungmotive beschrieben werden. Der Polymorphismus entsteht einerseits aufgrund der relativ starken Molekül-Substrat Wechselwirkungen bedingt durch das große Heptazine-Gerüst, andererseits können große Moleküle wie Melem auf vielfältigste Weise miteinander wechselwirken.
Für die oberflächenbasierte Polymerisation von kovalenten Netzwerken werden verschiedene Substrate, Kupplungsreaktionen und Reaktionsparameter untersucht. Von Vorteil bei der Kupplung von endständigen Alkinen ist, dass entweder Wasserstoff oder gar kein Nebenprodukt freigesetzt und somit die Substratoberfläche nicht durch Adsorbate verunreinigt wird. Auf Cu(111) werden jedoch viele unterschiedliche Reaktionen beobachtet, ohne eindeutige Präferenz für eine bestimmte Kupplungsreaktion. Durch Variation der Reaktionsparameter kann keine Verbesserung der Selektivität der Kupplungsreaktion von Diethynylbenzene auf Cu(111) erreicht werden.
Bei Ullmann Kupplung auf Metallsubstraten werden Halogenatome vom molekularen Baustein abgespalten, die dann auf der Oberfläche adsorbieren. Die kinetisch kontrollierte Polymerisationsreaktion führt zu kovalenten Netzwerken mit hoher Defektdichte. Auf Au(111) werden die direkte und hierarchische Polymerisation mittels eines mit Iod und Brom funktionalisiertem, aromatischem Moleküls realisiert. Die Optimierung der Reaktionsparameter wie z.B. Substrattemperatur, Heizrate oder Depositionsrate führt zu einer Verbesserung der Netzwerkqualität.
Im Gegensatz dazu können auf Ag(111) kovalente Netzwerke mit einem höherem Maß an Regelmäßigkeit synthetisiert werden. Maßgeblich dafür ist die Ausbildung von metastabilen Zwischenstrukturen basierend auf reversiblen organometallischen Bindungen. Organometallische Zwischenprodukte entstehen im Vergleich zu kovalenten Netzwerken bei niedrigeren Temperaturen. Eine Verbesserung der Netzwerkqualität kann erreicht werden, indem Selbstassemblierung und Fehlerkorrektur in organometallischen Netzwerken vor der kovalenten Vernetzung ausgenutzt wird.

Contents

List of Abbreviations

(hkl)	Miller indices of crystallographic planes
1D	one-dimensional
2D	two-dimensional
AO	atomic orbital
APCN	average pore coordination number
B3LYP	Becke 3-parameter, Lee, Yang and Parr functional
BE	binding energy
BDBA	1,4-benzenediboronic acid
BIB	1,3-bis(*p*-bromophenyl)-5-(*p*-iodophenyl)benzene
BTB	1,3,5-tris(*p*-carboxyphenyl)benzene
CHP	cyclohexa-*m*-phenylene
CHPR	cyclohexa-*m*-phenylene radical
COF	covalent organic framework
DEB	1,4-diethynylbenzene
DFT	density functional theory
FWHM	full-width at half-maximum
HE-SGM	high energy-spherical grating monochromator
HOPG	highly oriented pyrolytic graphite
HPB	1,3,5-trikis(*p*-carboxylphenyl)-2,4,6-trikis(*p*-tert-butylphenyl)-benzene
IMPF	inelastic mean free path
LanL2DZ	DFT basis set
LDOS	local density of states
LEED	low energy electron diffraction
MC	Monte Carlo
MM	molecular mechanics
MO	molecular orbital
MOF	metal organic framework
NEXAFS	near-edge X-ray absorption fine structure
OMBE	organic molecular beam epitaxy
PPB	poly(phenylene butadiynylene)
PTCDI	perylene tetra-carboxylic di-imide
QCMB	quartz crystal microbalance
RT	room temperature
SSR	surface stabilized radical
STM	scanning tunneling microscope/microscopy

TBB	1,3,5-tris(*p*-bromophenyl)benzene
TBQ	3,3”’-5,5”’-tetra(*p*-bromophenyl)-1,1’:4’,1”:4”,1”’-quaterphenyl
TEB	1,3,5-triethynylbenzene
TEPB	1,3,5-tris(*p*-ethynylphenyl)benzene
TMA	trimesic acid = 1,3,5-benzenetricarboxylic acid
TMEDA	N,N,N’,N’-tetramethylethylenediamine
TSP	titanium sublimation pump
TPR	temperature programmed reaction
UHV	ultra-high vacuum
UV	ultra-violet
VT STM	variable temperature scanning tunneling microscope
XPS	X-ray photoelectron spectroscopy

Chapter 1

Introduction

Until 2004 single layer 2D materials were presumed to be thermodynamically unstable.[1] However, the point of view had changed dramatically by the experimental discovery of graphene, a single layer of graphite. Since the Nobel prize in 2010 [2], graphene has received tremendous interest and is now the best known 2D material.[3] Graphene features many desirable physical properties such as mechanical and chemical robustness, but also high crystal quality and unprecedented charge carrier mobility even at room temperature.[1] Therefore, graphene is considered as a promising material for ultrafast, low power nanoelectronic devices in the "post-silicon" era. However, the applications of graphene are limited by the semimetallic behavior resulting from the vanishing bandgap.[1, 4] Applications in sensors or transistors ideally require a high current ratio between ON and OFF state.[5, 6] Graphene-based transistors, however, exhibit a high leakage current already in the OFF state.[7] This poses the challenge to create semiconducting, single layer 2D materials with a non-zero bandgap and high charge carrier mobility.

One strategy is the bottom-up fabrication of 2D materials by surface-mediated growth on metal substrates. As molecular building blocks especially planar aromatic molecules gained interest, because of their conjugated backbone. The emergence of 1D or 2D arrangements is driven by directional intermolecular interactions between the molecules. Accordingly, the molecular precursor largely determines the form and function of the resulting structure. Depending on the type of intermolecular interactions, non-covalent and covalent assemblies are distinguished.

Non-covalent assemblies are stabilized by the interplay of molecule–surface interactions and relatively weak molecule–molecule bonds such as hydrogen [8, 9] or halogen bonds [10, 11]. The relative strength and directionality of the intermolecular interactions can be used to control the formation of desired molecular architectures. The prediction of self-assembled structures on surfaces, however, is still a challenge in surface science due to the competition of various intermolecular and adsorbate–substrate interactions. Self-assembled structures are suitable for various applications such as host-guest-networks, or growth templates.[11, 12, 13, 14] However, their possible utilizations are restricted due to poor thermal and chemical stability as well as limited charge transport.

Hence, the application-driven demand of more stable structures has triggered an increasing interest in covalently bonded structures that provide improved chemical and mechanical stability. Interestingly, covalent nanostructures can also exhibit relatively high charge carrier mobilities due to their strong intermolecular bonds between the molecular building blocks. Covalent bonds between molecular precursors can be formed by on-surface polymerization resulting in surface-confined 2D nanostructures. In this respect, organic materials have the advantage to be extremely versatile and tuneable concerning structure, composition, and functional properties.[15] Their adjustable electronic band gap and the high charge carrier mobility, for example, make organic 2D materials highly interesting for applications in nanoscale (opto)electronic devices. Furthermore, the possibility to design porous molecular structures with atomically precise pore dimensions enables applications in membranes or sensors.[15, 16, 17, 18]

Up to now, on-surface polymerization already allows to synthesize well defined covalent chains such as poly(*para*-phenylene) [19] or graphene nanoribbons [20]. However, the synthesis of 2D organic nanostructures still suffers from high defect densities and the lack of long-range order.[18] To overcome this challenge, the scientific goal of this thesis is to improve the understanding of molecular reactions on surfaces, which is required for the tailored synthesis of desired structures. Thereby, the main focus lies on polymerization on metal surfaces, wherefore different substrate materials, coupling reactions, and reaction parameters are studied with the aim to enhance the quality of the covalent networks.

The characterization of 2D organic nanostructures requires detailed knowledge about structural aspects at the molecular scale such as orientation or bond configuration. For this purpose, scanning tunneling microscopy is perfectly suited as a local real-space technique with the capability of providing atomic resolution. Additionally, X-ray photoelectron spectroscopy as a space-averaging surface-sensitive analysis technique is applied to determine the chemical state of the adsorbed molecular structures on the surface. The combination of both measurement techniques allows the complementary characterization of molecular structures and chemical states.

The dissertation continues with a short description of scanning tunneling microscopy and X-ray photoelectron spectroscopy (chapter 2), whereby in particular the basic principle, the theoretical background, and the experimental setup are described. In the following two chapters, an introduction to molecular self-assembly and to on-surface polymerization is given. The experimental results are presented in chapter 5 to 7. Thereby, both approaches, molecular self-assembly as well as on-surface polymerization, are applied for the fabrication of 2D organic nanostructures on metal surfaces. Section 6.2 and chapter 7 tackle the question to improve the quality of covalent networks. Therefore, different on-surface polymerization reactions are investigated and the influence of different reaction parameters is intensively studied. In chapter 8, the experimental results are summarized and a new strategy towards controlled on-surface polymerization of tailored structures is discussed.

Chapter 2

Surface Analysis Techniques

The analysis of adsorbed molecules on surfaces or of surface-supported 2D nanostructures requires surface sensitive measurement techniques. In this context, often a combination of scanning tunneling microscopy (STM) and X-ray photoelectron spectroscopy (XPS) is used for a complementary characterization. STM reveals structural information, which is supported by information about the chemical state obtained from the XPS measurements. The focus of the following chapter is to introduce the basic principles as well as the corresponding experimental setups of both analysis techniques.

2.1 Scanning Tunneling Microscopy

Scanning tunneling microscopy (STM) is a surface sensitive, real-space analysis technique with a resolving power down to single atoms. Thereby, a local probe is used to image surface structures such as steps, single defects, or adsorbed molecules on surfaces. In contrast to diffraction techniques such as low energy electron diffraction (LEED), STM enables the determination of periodic as well as nonperiodic, disordered arrangements. These characteristics provide powerful imaging capabilities for the investigation of molecular self-assembly or polymerization reactions on metal surfaces. In the presented work, STM measurements are used to identify the molecular orientation and the intermolecular interactions between adsorbed molecules. The distance between adjacent molecules is representative for the bond length, which is characteristic for a particular type of bond. In context of on-surface polymerization, reaction intermediates are resolved and the reaction progress is monitored. Reaction intermediates can be distinguished from the final covalent structure by their elongated bond length. For both intermediate and finial structures, however, the formation of branched and disordered arrangements is often observed. Furthermore, STM measurements can also be applied to study the influence of synthesis parameters on the network structure by imaging the resulting molecular arrangements obtained for different preparation protocols.

2.1.1 Basic Principle

STM is based on the quantum mechanical tunneling effect. In quantum mechanics a particle can "tunnel" with a finite probability through an energy barrier larger than the particle's total energy. According to classical physics, however, the region inside the barrier is forbidden and the particle can not cross the barrier. In an STM, tunneling occurs between a sharp metal tip and a conducting sample separated by a vacuum barrier of width d (Fig. 2.1). An applied external voltage V between tip and sample shifts the respective Fermi levels relative to each other. Electrons in the energy range of eV below E_{FS} can tunnel from occupied states of one side to unoccupied states of the opposite side, resulting in a net tunneling current I_T.[21, 22] Depending on the polarity of the voltage V, electrons tunnel from the sample into the tip as shown in Fig. 2.1 or *vice versa*. The height of the vacuum barrier is in the order of the average work function of tip and sample φ.

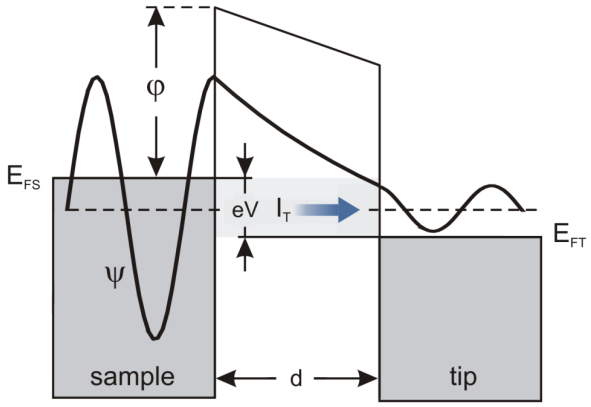

Figure 2.1: Sketch of a one-dimensional tunneling barrier with the width d. A bias voltage V is applied between sample and tip shifting the Fermi level of sample E_{FS} and tip E_{FT}. Adapted from Ref. [23].

Tunneling processes are fundamental to quantum mechanics and follow directly from the solution of Schrödinger's equation. For a one-dimensional rectangular barrier the solution results in an exponential decay of the wave function ψ within the barrier region.[21, 24] The tunneling current is proportional to the transmission probability of electrons tunneling through the barrier as shown in Eq. 2.1.

$$I_T \propto \sum_{E_{\mathrm{n}}=E_{\mathrm{F}}-eV}^{E_{\mathrm{F}}} |\psi_0|^2 e^{-2\kappa d} \tag{2.1}$$

with the decay constant $\kappa^2 = 2m(\varphi - E)/\hbar^2$, the energy of the state E, the electron mass m, and the barrier potential φ.
Accordingly, the tunneling current decays exponentially with the barrier width d. For typical work functions of around 5 eV, the tunneling current is extremely sensitive to distance changes between tip and sample. Vacuum barrier variations of

1 Å, for example, change the tunneling current by nearly one order of magnitude. Consequently, for a sharp tip a dominant contribution to the tunneling current arises from the foremost row of atoms, which is closest to the sample. This effect accounts for the high vertical resolution of the STM.

2.1.2 Tunneling Theory

Since the invention of STM by Binnig *et al.*,[25, 26] several methods for theoretical calculation of the tunneling current have been reported. Tunneling theory can be explained by Bardeen's transfer Hamiltonian approach,[27] which was applied to the STM by Tersoff and Hamann.[28, 29] First-order time dependent perturbation theory results in the following equation for the tunneling current:

$$I_T = \frac{2\pi e}{\hbar} \sum_{\mu\nu} f(E_\mu)[1 - f(E_\nu + eV)] \mid M_{\mu\nu} \mid^2 \delta(E_\mu - E_\nu) \tag{2.2}$$

with the applied bias voltage V and the tunneling matrix element $M_{\mu\nu}$ between the state ψ_μ and ψ_ν of the respective electrodes. E_μ and E_ν are the corresponding energies of the state ψ_μ and ψ_ν. The Fermi function $f(E)$ describes the occupation of the states since only tunneling can occur from filled into empty states. The δ-function expresses the energy conservation for elastic tunneling, *i.e.* electrons tunnel without energy loss inside the barrier.[30, 31] In principle, inelastic tunneling is also a possible mechanism, whereby electrons lose energy inside the barrier. Thus, the total tunneling current can feature contributions from elastic and inelastic tunneling. Inelastic tunneling can occur, for example, *via* excitation of a vibrational mode of a molecule resulting in an increased tunnel conductivity.[30]
According to Bardeen,[27] the tunneling matrix element $M_{\mu\nu}$ can be evaluated by the wave functions of two non-interacting electrodes as

$$M_{\mu\nu} = \frac{\hbar^2}{2m} \int d\vec{S}(\psi_\mu^* \vec{\nabla}\psi_\nu - \psi_\nu \vec{\nabla}\psi_\mu^*) \tag{2.3}$$

where the integral is calculated over an arbitrary surface lying entirely within the vacuum barrier region separating tip and sample. Since most experiments are performed at relatively low temperatures and at small voltages, Tersoff and Hamann suggested the following simplification:

$$I_T = \frac{2\pi}{\hbar} e^2 V \sum_{\mu\nu} \mid M_{\mu\nu} \mid^2 \delta(E_\mu - E_F)\delta(E_\nu - E_F) \tag{2.4}$$

where E_F is the Fermi energy. The calculation of the tunneling current, however, requires knowledge of the wave functions of both electrodes namely surface and tip. Since the tip wave function is usually not known, an assumption is required to calculate the tunneling current. Tersoff and Hamann approximated a spherical

tip with local radius R.[28, 29] In this context, the tunneling matrix element was only evaluated for a single s-type tip wave function, whereby the possible angular dependence of wave functions was neglected. Considering these assumptions, Eq. 2.4 of the tunneling current reduces to: [29]

$$I_T \propto \sum_{\nu} \mid \psi_{\nu}(\vec{r}_0) \mid^2 \delta(E_{\nu} - E_F) \equiv \rho(\vec{r}_0, E_F) \tag{2.5}$$

Accordingly, the tunneling current directly corresponds to the local density of states $\rho(\vec{r}_0, E_F)$ (LDOS) at the Fermi level E_F, *i.e.* the charge density from electronic states at E_F. $\vec{r}_0$ must be interpreted as the position of the probe and refers to the effective center of curvature of the tip.
In contradiction to the predicted resolution limit of Ref. [29], atomic distances can be resolved in experimental STM images. Chen *et al.* presented a theory that explained atomic resolution by using localized surface states on the tip such as p_z (*e.g.* for silicon) and d_{z^2} (*e.g.* for Pt, Ir, W) dangling-bond states.[32] The tunneling current is attributed to an overlap of the tip wave function with the wave function of the sample surface.

2.1.3 Experimental Apparatus

All STM experiments presented in this work were carried out under ultra-high vacuum conditions. The low base pressure has the advantage to minimize surface contamination from the surrounding atmosphere over a reasonable period of time. Furthermore, the use of solvents is not required as for STM measurements under ambient conditions, which can influence the formation of the resulting structure by incorporation of solvent molecules. UHV conditions, instead, enable the direct investigation of molecules on surfaces without influences arising from co-adsorbed molecules such as gas atoms or solvent molecules.

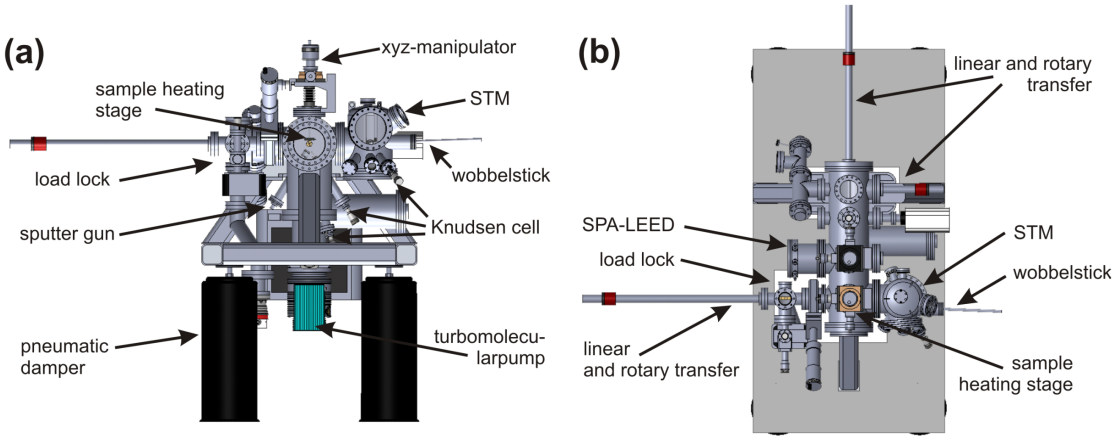

Figure 2.2: Schematic side (a) and top (b) view of the UHV system.

The applied UHV apparatus (Fig. 2.2) is a multi-chamber system consisting of a load lock and a main chamber with a base pressure of 5×10^{-8} mbar and 2×10^{-10} mbar, respectively. The whole chamber is mounted on four pneumatic dampers in order to isolate the system from external vibrations. The main chamber and the load lock are pumped independently by an oil-free forepump unit, a turbomolecular pump and an ion getter pump. Additionally, a titanium sublimation pump (TSP) is integrated within the main chamber to enhance the pumping rate.

For surface analysis the main chamber is equipped with an STM and a spot profile analysis LEED (SPA-LEED) system. All STM data presented in this work were acquired under ultra-high vacuum conditions either with a commercially available *Omicron NanoTechnology* variable temperature STM (VT STM) or a home-built STM. A scheme of the home-built STM is shown in Fig. 2.3. The STM scan head consists of a nanopositioner and a piezo scanner, which is mounted on a base plate together with the sample holder. The base plate is integrated in a damping system for vibrational isolation, which consists of metal springs, copper elements and permanent magnets. For detailed information about the home-built STM see Ref. [33]. All STM data were recorded at room temperature with a SPM 100 control electronics from RHK using the XPM Pro 2.0.1.5 software. The STM was calibrated in lateral direction with atomically resolved topographs of highly oriented pyrolytic graphite(0001) (HOPG). For the calibration in z-direction, on the other hand, topographs of step edges on a Au(111) single crystal were used.

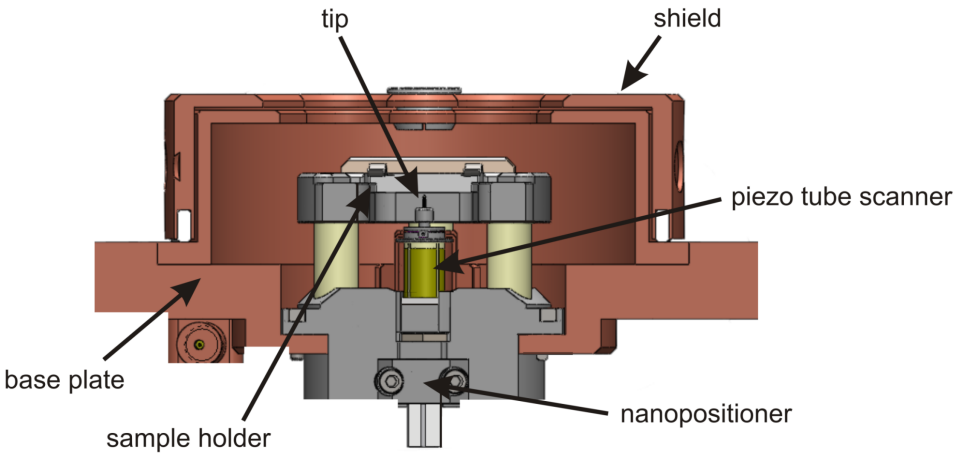

Figure 2.3: Scheme of the home-built STM unit. The STM scan head consists of a nanopositioner and a piezo tube, which carries the tungsten tip on top. The sample holder and the STM scan head are mounted on a base plate. Adapted from Ref. [33]

The tungsten tips and the substrates such as metal single crystals or HOPG are stored in a carousel within the main chamber. For manipulation between storage carousel, preparation stage, and STM a wobbelstick is used, whereas for the transfer to the load lock or the SPA-LEED a magnetic linear and rotary transfer is applied.

In addition to the surface analysis tools, the main chamber is equipped with standard components for sample preparation such as a sputter gun and a three-axes manipulator with a radiatively heated sample stage. Single crystal surfaces are prepared by cycles of Ar^+-ion sputtering at 500 eV and annealing at 500 °C. The cleanliness of the substrate is always verified by STM prior to molecular deposition. The tungsten tips can be cleaned *in vacuo* by means of an ion-sputtering and electron-beam annealing device (*cf.* Fig. 1b in Ref. [34]).

Furthermore, evaporators for metal as well as for organic molecular beam epitaxy (OMBE) are attached to the chamber. The metal evaporator is a commercially available *Omicron* EFM 3i evaporator. The home-built Knudsen cell is described in detail elsewhere.[35] The Knudsen cell is equipped with a quartz crystal microbalance (QCMB) which is integrated in the beam shutter. Thereby, the eigenfrequency decline $\Delta f/\Delta t$ of the QCMB serves as a quantitative measure of the deposition rate. The eigenfrequency decline for 1,3-bis(*p*-bromophenyl)-5-(*p*-iodophenyl)benzene (BIB) at different sublimation temperatures is shown in Fig. 2.4. The slope $|\Delta f|/\Delta t$ increases with the sublimation temperature from 0.05 (145 °C) to 1.4 (167 °C). On Au(111) substrates, deposition of BIB at 167 °C for 3 min yields a surface coverage of $\sim 60\%$. Accordingly, an eigenfrequency decline of 1.4 corresponds to a deposition rate of about 0.2 monolayer min^{-1}.

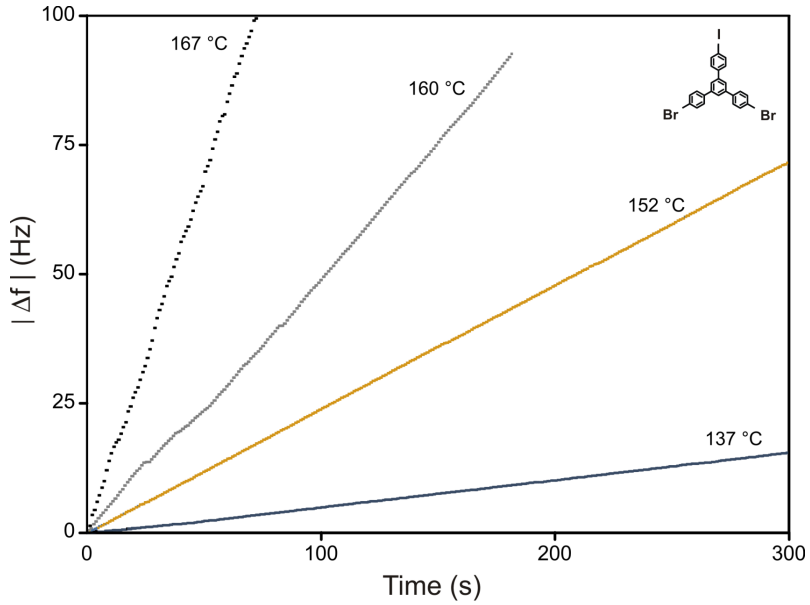

Figure 2.4: Eigenfrequency decline of the QCMB as a function of deposition time at different sublimation temperatures, *i.e.* crucible temperature of the deposition source. The inset shows the chemical structure of the sublimated molecule 1,3-bis(*p*-bromophenyl)-5-(*p*-iodophenyl)benzene (BIB).

2.2 X-Ray Photoelectron Spectroscopy

Scanning tunneling microscopy reveals the structure and the orientation of adsorbed molecules on surfaces, but also provides information about possible phase transitions during on-surface reactions. However, often details about chemical state and environment of adsorbates are required for a complete identification of the molecular structure or to reveal chemical changes. Therefore, X-ray photoelectron spectroscopy (XPS) is used as complementary, chemically and surface sensitive technique. The chemical state of surfaces can be identified by electromagnetic irradiation with high energy X-rays (1.0 - 1.5 keV) under UHV conditions.
In contrast to STM, XPS has a limited spatial resolution and integrates over square millimeters of sample area. In the following, the basic principle of X-ray photoelectron spectroscopy is presented, beginning with the theoretical background. Additionally, the quantitative analysis of XP spectra and the emergence of chemical shifts in the binding energy are discussed.

2.2.1 Theoretical Background

XPS is based on the photoelectric effect, which was systematically studied by Heinrich Rudolf Hertz in 1887 for ultra-violet (UV) light and theoretically explained by Albert Einstein in 1905.[36] The photoelectric effect describes the emission of photoelectrons from a metal surface upon exposure to electromagnetic radiation. In XPS the emission of photoelectrons from the core level is triggered by X-ray radiation. The photoionization process consists of three steps: photon absorption, generation of a photoelectron, and escape of the photoelectron into the vacuum resulting in the formation of a positive ion. The kinetic energy of the emitted photoelectron is given by: [37, 38]

$$E_{\mathrm{Kin}} = \hbar\omega - E_{\mathrm{B}} - \phi \tag{2.6}$$

where $\hbar\omega$ is the energy of the absorbed photon, E_{B} the binding energy of the electron relative to the Fermi level, and ϕ the work function of the spectrometer (Fig. 2.5). Accordingly, the kinetic energy E_{Kin} of the emitted photoelectrons depends on the photon energy and reveals information about E_{B} of occupied sample states.
For XPS measurements, laboratory radiation sources with characteristic energies are usually applied such as non-monochromatic Mg K_α ($\hbar\omega = 1253.6\,\mathrm{eV}$) or monochromatic Al K_α ($\hbar\omega = 1486.7\,\mathrm{eV}$),[37, 38] but also synchrotron-based radiation sources with tuneable energy are typically used. Monochromatic X-ray sources obtain a narrower energy distribution compared to unfiltered X-ray lines. The advantage of using monochromatic X-rays is that the resolution of photoelectron peaks is improved. Furthermore, additional photoelectron peaks are removed in the XP spectrum, which are produced by minor X-ray lines of the light source.

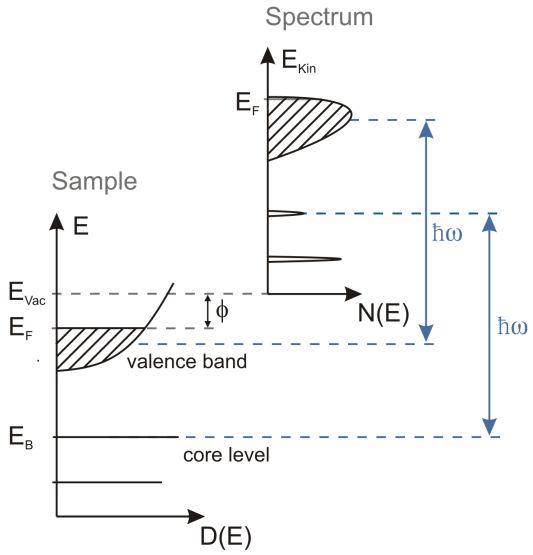

Figure 2.5: Schematic principle of XP spectroscopy with photon energy $\hbar\omega$. The relation between the energy levels in the sample and the electron energy distribution in a XP spectrum is shown. $D(E)$ is the density of state and $N(E)$ the signal intensity, *i.e.* the number of detected electrons. Adapted from Ref. [39].

Generally, in XPS measurements the kinetic energy of the emitted photoelectrons is determined. In the corresponding XP spectra (*cf.* Fig. 2.6), however, the binding energy calculated by means of Eq. 2.6 is shown. Accordingly, zero binding energy corresponds by definition to the Fermi level.

The detected electrons are mainly emitted from core levels, which are not directly involved in chemical bonding. Core levels are essentially localized at the atoms with characteristic binding energies for each element.[40, 41] Thus, XPS measurements result in a spectrum of sharp peaks with specific binding energies, which are representative for the chemical composition of the sample. In Fig. 2.6 a XP spectrum of a Au(111) surface is shown. The photoelectron peak near E_F corresponds to the valence band, whereas Au 4f, 4d, 4p are core level peaks. Besides the characteristic Au peaks, a C 1s core level peak is present, indicating surface contamination.

XPS is a surface-sensitive analysis technique due to the limited inelastic mean free path λ_in (IMFP) of electrons in solids on the order of nm.[37, 38] The IMFP is the average distance that an electron travels between two inelastic scattering events. Thus, the majority of detected electrons arise from a depth of less than or equal to three times λ_in, whereas the photoionization occurs up to a depth of a few microns. In XP spectra, the electrons which leave the surface without energy loss contribute to the characteristic spectrum, whereas the inelastically scattered electrons account for the background.

The IMFP depends strongly on the kinetic energy of the electrons with a minimum at around 50 eV.[37, 41] Interestingly, the energy dependence of the IMFP changes only slightly for various materials.[39] Typically, the IMFP is in the order of 0.5 nm to 2 nm for kinetic energies of 50 eV to 2000 eV.[37, 41]

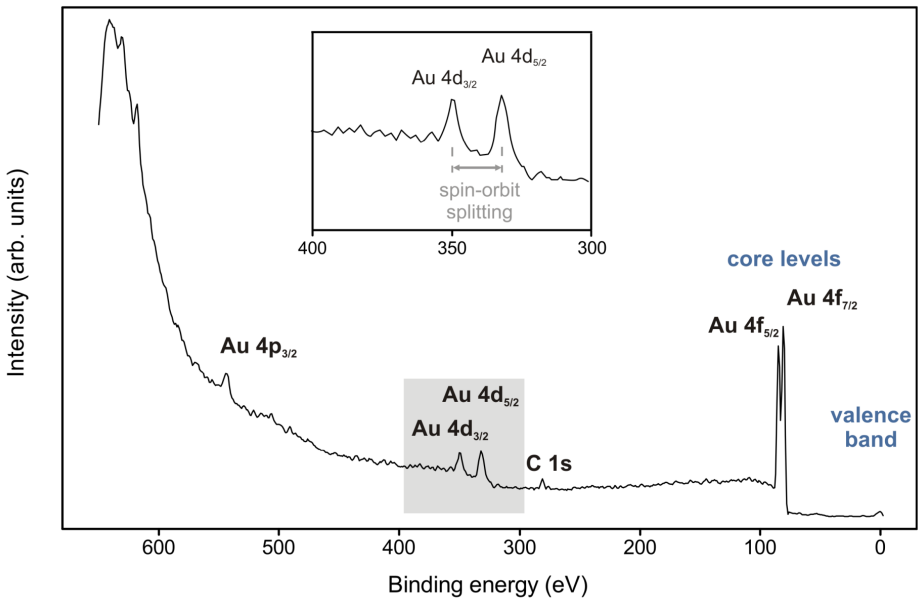

Figure 2.6: XP spectrum from a Au(111) surface for $0\,\text{eV} \leq E_\text{B} \leq 650\,\text{eV}$. The valence band and the core level peaks are clearly discernable. Beside the characteristic Au peaks, a C 1s peak is present indicating organic impurities on the surface. The background increases clearly with increasing E_B. The inset shows the grey highlighted region of the spectrum in more detail.

The width of a single XPS peak originates from a convolution of three main contributions: the natural line width ΔE_n, the FWHM of the exciting X-ray source ΔE_x, and the analyzer resolution ΔE_a: [37, 42, 43]

$$\Delta E = (\Delta E_\text{n}^2 + \Delta E_\text{x}^2 + \Delta E_\text{a}^2)^{1/2} \tag{2.7}$$

ΔE corresponds to the full-width at half-maximum (FWHM) of a XPS peak. ΔE_n is determined by the limited core hole lifetime τ in the ionized state produced by photoelectron emission. The natural line width ΔE_n can be calculated from the uncertainty principle:

$$\Delta E_\text{n} = \frac{h}{\tau} \tag{2.8}$$

where h is the Planck's constant and τ is the lifetime of the core hole in the ionized state.[37, 42] The lifetime normally varies between 10^{-15} s and 10^{-13} s resulting in a ΔE_n between 4 eV and 0.04 eV.[37]

In addition to first-order photoelectron peaks, the XP spectrum can also contain Auger peaks as a de-excitation product of the primary core level. Auger electrons are emitted as a consequence of a three-electron process. Initially an electron from a core level is emitted by absorption of a photon. The resulting core hole is refilled by

an electron transition from a higher energy level and an Auger electron is emitted by transferring the gained energy to a third electron. In contrast to first-order photoelectron peaks, the energy of the Auger peak is independent of the excitation energy.

2.2.2 Quantitative Analysis

XPS measurements allow to determine the chemical composition of surfaces as well as the relative concentrations of the various constituents. For the quantitative analysis the intensity or the area of photoelectron peaks in a XP spectrum are used. The number of photoelectrons per second of a homogeneous sample is given by: [38]

$$I_i = n_i \; f \; \sigma_i \; \theta \; y_i \; \lambda_{\text{in}} \; A \; T = n_i \; S_i \tag{2.9}$$

where n_i is the number of atoms per cm^3 of an element i, f is the X-ray flux, σ_i the photoionization cross-section for the core level of interest, θ the angular efficiency factor for the instrument, y_i the efficiency in the photoelectron formation process, λ_{in} the inelastic mean free path of the photoelectrons, A the analysis area on the sample, and T the detection efficiency. In this context, the atomic sensitivity factor S_i is introduced summarizing all parameters in Eq. 2.9 except for the concentration n_i. S_i varies for different elements, but also depends on the specific core level and the photon energy.
A general expression for the determination of the concentration c_x of a single constituent x in a sample can be obtained by extending Eq. 2.10 to: [38]

$$c_x = \frac{n_x}{\Sigma n_i} = \frac{I_x/S_x}{\Sigma I_i/S_i} \tag{2.10}$$

2.2.3 Chemical Shifts

In XPS measurements, the elemental composition of a surface or of adsorbed molecules can be identified by the accurate determination of the core level binding energies which are characteristic for the corresponding element. Typically, core levels are not directly involved in chemical bonds to other atoms, but are influenced by the chemical environment, oxidation or bonding states.[40, 41] Thereby, changes in the valence electron density can cause a positive or a negative partial charge on an atom. As a consequence, the potential of the core electrons is affected resulting in small chemical shifts of the core electron binding energy (typically 0 - 3 eV).[37] Bonds to more electronegative atoms, for example, decrease the electron density of the valence states resulting in a positive partial charge on the atom and an increased binding energy of the core level electrons. Accordingly, the identification of chemical states in XPS measurements is only possible due to the occurrence of chemical shifts.

2.2.4 Spin-Orbit Splitting

Spin-orbit coupling is an initial state effect, which can be intuitively understood in a semiclassical picture. It occurs due to interactions between spin magnetic momentum and orbital angular momentum. In the electron rest frame, the positive charged nucleus circulates around the electron. The relative motion of the nucleus causes a circular current generating a magnetic field B_L. The induced magnetic field B_L is proportional and parallel to the orbital angular momentum $L = r \times p$ of the electron. Within the magnetic field B_L the magnetic spin moment of the electron can have two spatial orientations. According to the two spin directions, the energy level is split into two components.[44]

In XPS measurements core levels are investigated, which are described by the quantum number n, orbital quantum number l, and spin quantum number s. However, in presence of spin-orbit coupling the total angular momentum j of the core level is essential. For $s = \frac{1}{2}$ the total angular momentum amounts to $j_{\pm} = l \pm \frac{1}{2}$.
For core levels with $l = 0$ single XPS peaks without spin-orbit splitting are obtained (*cf.* C 1s in Fig. 2.6). For $l > 0$ the level splits into two levels with different energies *e.g.* Au $4d_{3/2}$ and Au $4d_{5/2}$ in Fig. 2.6 (inset). To separately resolve both peaks in the XP spectrum, however, high energy resolution and large spin-orbit coupling energies are required. The relative intensity ratio of the two peaks of a spin-orbit split doublet is given by the ratio of the multiplicity of each level:

$$\frac{2j_- + 1}{2j_+ + 1} \tag{2.11}$$

For p spin-orbit doublets the peak area ratio is 1:2, for d spin-orbit doublets the ratio is 2:3.[45, 46] The doublet of an Au 4d level is shown in the inset of Fig. 2.6. The two peaks are separated by an energy difference of 18 eV, [38] whereby Au $4d_{3/2}$ obtains a higher binding energy as compared to Au $4d_{5/2}$. Generally, the magnitude of spin-orbit splitting decreases with increasing quantum numbers n for the same l value and with increasing l for the same principal quantum number n.[44, 47] Accordingly, the splitting of Au $4d_{3/2}$/Au $4d_{5/2}$ is larger than the splitting of Au $4f_{5/2}$/Au $4f_{7/2}$ as shown in the XP spectrum of a Au(111) surface in Fig. 2.6.

2.2.5 Experimental Apparatus

All XPS data presented in this work were measured at the HE-SGM beamline of the synchrotron radiation facility BESSY II in Berlin.[48] The synchrotron radiation source BESSY II covers a wide energy range from terahertz to hard X-rays. For experiments, multiple different beamlines are connected to the storage ring. Depending on the beamline, different beam characteristics such as energy range and polarization are available.[48]

The HE-SGM beamline is a dipole magnet beamline named after the implemented High Energy-Spherical Grating Monochromator (HE-SGM). The X-ray light is horizontally polarized with a degree of 91 % at a flux of up to 5×10^{11} photons/(s · 100 mA).[48] The HE-SGM beamline offers photon energies in the range of 100 eV to 750 eV with an energy resolution $E/\Delta E$ between 500 and 2500.[48] The X-ray flux as well as the resolution depend on the photon energy and the monochromator grating (*cf.* Ref. [48] for details). The size of the elliptical spot on the sample surface amounts to $(1.2 \times 0.5)\,\mathrm{mm}^2$.
At the HE-SGM beamline a permanent experimental end station is installed which is shown in Fig. 10.6 and 10.7 of Ref. [49]. The end station is a multi-chamber UHV system and consists of four different chambers used for transfer, preparation, analysis, or as load lock. The base pressures in the preparation chamber and in the analysis chamber are about 2×10^{-9} mbar and 7×10^{-10} mbar, respectively.
In the UHV end station different surface analytic tools are combined such as low energy electron diffraction (LEED), near-edge X-ray absorption fine structure (NEXAFS), and XPS. Additionally, the UHV system is equipped with standard facilities for sample preparation and provides space for up to five evaporators for metal or organic molecular beam epitaxy (OMBE). The installed continuous-flow liquid He-cryostat allows sample cooling down to 50 K.[49] The samples can also be annealed up to 1000 K by electron beam or resistive heating depending on the sample holder.[48, 49] The samples are mounted in a five-axes manipulator with three translational and two rotational degrees of freedom.
For XPS measurements a VG Scienta R3000 high resolution, hemispherical energy analyzer is implemented in the analysis chamber, which allows the measurement of kinetic energies from 0.5 eV to 1500 eV.[50] The analyzer axis is normal to the sample surface, whereas the X-ray beam has an incidence angle of 45° relative to the surface normal. In contrast to conventional laboratory X-ray sources, synchrotron radiation enables XPS measurements with high X-ray fluxes facilitating high elemental sensitivities. Additionally, the continuous energy spectrum of synchrotron radiation allows the selection of specific photon energies. Thus, the photon energy can be tuned for optimum photoionization cross-sections. The photoionization cross-section σ varies considerably depending on element, core level, and photon energy.[51] For Br 3d, for example, σ decreases by roughly two orders of magnitude upon increasing the photon energy from ∼300 eV to ∼1300 eV.[52] Accordingly, the use of synchrotron radiation sources improves the relative detection limit for probing the Br 3d core level compared to laboratory X-ray sources with typical photon energies >1000 eV.
Prior to the XPS measurements, the samples are similarly prepared as in the STM experiments. Single crystal surfaces are prepared by cycles of Ar^+-ion sputtering at 1000 eV and annealing at 450 °C. The cleanliness of the substrate is verified by XPS in the analysis chamber. Subsequently, the substrates are transferred to the preparation chamber for organic molecular beam epitaxy by means of a home-built Knudsen cell [35] .

Chapter 3

Molecular Assembly on Surfaces

Molecular assembly on solid surfaces is an established approach for the bottom-up fabrication of 2D organic nanostructures. Confining molecules to a 2D surface eliminates several degrees of translational, rotational and vibrational freedom.[53] Organic molecules are often confined in a planar geometry and molecular interactions direct the formation to 1D or 2D nanostructures on the surface.
An elementary step in the formation of molecular assemblies is diffusion and 2D rotation of the molecular building blocks on the surface. Both diffusion and rotation require thermal activation to overcome the associated energy barriers.[13] For molecular assemblies, generally, the adsorption energy of the molecules on the surface needs to be higher than the energy barrier for diffusion. Otherwise, the molecules would preferentially desorb from the surface before the formation of 1D or 2D structures can take place.

The emergence of molecular structures is governed by the interplay of molecule-surface interactions and direct molecule–molecule bonds.[54, 55] In dependence on the type of the intermolecular bonds, covalent and non-covalent assemblies are distinguished.
Non-covalent assemblies are usually based on relatively weak intermolecular interactions such as van der Waals interactions, halogen or hydrogen bonds (*cf.* section 3.1). The reversibility of these interactions allows error correction processes through elimination of defective structures resulting in the formation of almost defect-free, long-range ordered self-assemblies.[13, 53] The formed self-assembled structures, however, do not facilitate intermolecular charge transport as well as suffer from poor thermal and chemical stability due to the comparably weak interaction energies. These characteristics restrict potential technological applications of non-covalent assemblies.[56, 57]
Covalent assemblies, on the other hand, are usually 1D or 2D polymers, which are stabilized by strong covalent bonds (*cf.* subsection 3.1.4). The synthesis of covalent nanostructures by means of on-surface polymerization is discussed in chapter 4 in detail. Compared to hydrogen or halogen bonds, covalent bonds exhibit a significantly higher binding energy restricting rearrangement and self-correction processes. The irreversibility of covalent bonds prevents the formation of equilibrium

structures resulting in ill defined geometries. Covalent structures, however, posses interesting electronic properties in combination with remarkable chemical and mechanical stability. Both characteristics facilitate the application of low dimensional covalent organic materials in the field of nanotechnology.

For the controlled synthesis of non-covalent and covalent structures, the building blocks are specifically designed by tailored functionalization. Thus, site-specific and complementary molecular interactions between functional groups direct the lateral assembly process and lead to the formation of targeted structures. On the other hand, molecule-surface interactions can affect the mobility and conformation of the molecules depending on substrate reactivity, symmetry, and electronic properties.[13] Consequently, the *ab initio* prediction of the resulting structure is complicated by the interplay and the competition of various interactions.
In the following, an overview of intermolecular interactions, thermodynamics and kinetic effects is given. The focus lies on the formation of molecular structures on single crystal metal surfaces using organic molecules as building blocks.

3.1 Intermolecular Interactions

The formation of supramolecular assemblies on surfaces is driven by intermolecular interactions between molecular building blocks. The molecules can be functionalized with equal or different types of side groups. Depending on the type of functional group, different intermolecular interactions with remarkably different binding energies and geometries are favored. For the on-surface formation of stable supramolecular structures at RT, adsorption energies per molecule higher than $\sim$1 eV are required to prevent significant thermal desorption of the molecules from the surface.[13]
In the presented thesis, a variety of non-covalent (chapter 5, 6, 7) and covalent nanostructures (chapter 6, 7) is synthesized. The characteristics and properties of the underlying bond types are discussed in the following section. Thereby, the focus lies on intermolecular interactions between planarly adsorbed organic molecules on surfaces.

3.1.1 Hydrogen Bonds

Hydrogen bonds are attractive, directional, non-covalent interactions between a hydrogen atom H and an electronegative atom Y such as N, O, or F.[58, 59, 60] The hydrogen atom is covalently bound to a more electronegative atom X, resulting in a polarized X$-$H bond with a partially positively charged H atom.[61] The hydrogen bond acceptor Y is usually an atom or a molecule fragment, that belongs to the same or to a different molecule as the hydrogen atom. The formed bond interlinks two atoms X and Y *via* a bridging hydrogen atom, which is generally abbreviated as

X−H···Y. Hydrogen bonds have several contributions from electrostatics, polarization, van der Waals, or covalent interactions.[62, 63] Typical interaction energies span a wide range up to ∼40 kJ mol^{-1},[55, 58, 62, 64]. The corresponding bond lengths between a hydrogen atom H and an acceptor Y are typically in the order of ∼0.12 - 0.32 nm.[65]
The bond strength of the hydrogen bond increases with the electronegativity of X and Y.[61, 63, 66] Thus, weak (C−H···O, C−H···N) and strong (O−H···O, N−H···O) hydrogen bonds can be distinguished.[60, 66] In strong hydrogen bonds (20 - 40 kJ mol^{-1}) X and Y are both strongly electronegative such as in N−H···O. By constrast, in weak hydrogen bonds (2 - 20 kJ mol^{-1}) at least one of the atoms exhibits only moderate or low electronegativity as in C−H···O.[63]

Owing to their strength and directionality, hydrogen bonds play an important role as stabilizing interactions between functional groups in non-covalent assemblies on surfaces. However, the self-assembled structures are usually formed by the interplay of numerous different hydrogen bonds,[60] which makes it rather challenging to control self-assembled arrangements by tailored design and functionalization of molecular building block. In the context of supramolecular engineering, organic molecules are often functionalized with carboxylic acid groups (–COOH) to direct the structure formation.[8, 67, 68] Carboxylic acids form hydrogen bonds in a self-complementary manner *via* double O−H···O hydrogen bonds, but also different synthons containing both O−H···O and C−H···O interactions are possible.[63]
Two-fold hydrogen bonds can also be formed between ethynyl groups (C≡C−H··· C≡C, Fig. 6.1, section 6.1). Thereby, the hydrogen acts as a donor and the aromatic triple bond as a multi-atom acceptor.[66, 69] In this context, additional stabilization arises from intermolecular interactions between ethynyl groups and adjacent phenyl rings.
Multiple types of hydrogen bonds are also identified in self-assembled structures of 2,5,8-triamino-1,3,4,6,7,9,9b-heptaazaphenalene, a triply amino substituted heptazine (C_6H_7) ring (Fig. 5.1(b), chapter 5). The formed structures are stabilized by two equivalent cyclic N_{amino}−H···$N_{heptazine}$ hydrogen bonds either in a head-to-tail or side-by-side arrangement (Fig. 5.5).

3.1.2 Halogen Bonds

Halogen bonds are attractive highly-directional and non-covalent interactions between covalently-bonded halogen atoms (R−X) and a negative site (nucleophile D) like N, O, Cl, Br, or I.[70, 71] The general scheme of halogen bonding is abbreviated as D···X−R, where R can be either another halogen atom or a molecule fragment. Calculations of the halogen bond strength suggest interaction energies of ∼33 kJ mol^{-1}.[72]
The halogen interaction originates from the non-spherical charge distribution around the halogen atom. As a consequence, the effective atomic radius of X perpendicular to the C−X bond axis is longer than the radius along the axis (*cf.* Fig. 3.1(a)).[73, 74] The

electrostatic potential on the surface of Cl, Br, and I atoms is positively charged δ^+ at the tip of the halogen atom (σ-hole), while a belt around the R−X bond is negatively charged δ^- (Fig. 3.1(a)).[72, 75, 76] By contrast, the electrostatic surface potential of a F atom is usually entirely negative unless it is linked to strongly electron-withdrawing groups.[77] Thus, halogen bonding can be explained in terms of electrostatic attraction between an electrophilic and a nucleophilic site.

Due to the non-spherical electrostatic potential, halogen atoms can simultaneously act as both halogen bond acceptors and -donors. This characteristic facilitates interhalogen interactions R−X···X−R, so called halogen-halogen bonds. Thereby, the halogen atom binds in a linear configuration with nucleophiles and in a sidewise configuration with electrophiles as shown in Fig. 3.1(b).[11, 78]

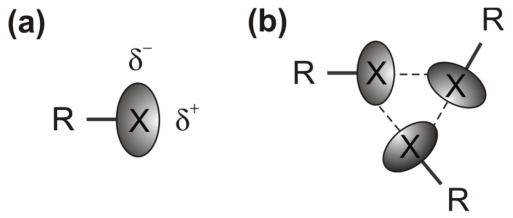

Figure 3.1: (a) Electrostatic potential in a R−X bond with a positive charged cap (white) and a negative charged belt (gray) of the X-atom. (b) X-bond interaction scheme of three halogen groups.

The positive potential is determined by the electron-withdrawing effect of the neighboring group R,[79] and the polarizability as well as the electronegativity of the halogen atom X. For similar R, the positive potential at the halogens increases in order of F < Cl < Br < I, accompanied by larger polarizability and lower electronegativity.[71, 75] These characteristic facilitates variation of the halogen bond strength by the choice of halogen atom.[10]

In the context of tailored self-assembly on surfaces, halogen bonds represent a suitable alternative to hydrogen bonding due to their selectivity, directionality, and tuneability. The possibility to determine the final structure by tailored halogenation of the building blocks was already investigated by Pham *et al.* [10]. Furthermore, the formation of supramolecular structures stabilized by cyclic threefold halogen-halogen-halogen bonds was reported for trihalomesitylene molecules (Fig. 3.1(b)).[78] The triangular bonding schemes are based on three cooperative donor-acceptor interactions, whereby the halogen atoms interact with nucleophiles in a head-on and with electrophiles in a side-on arrangement. Depending on the type of halogen, the distance between adjacent halogen atoms changes slightly from ∼0.39 nm for iodine to ∼0.36 nm for bromine and chlorine.[78] Besides triangular trihalogen interactions, also fourfold halogen interactions are observed for rod-like molecules such as 4,4”-dibromo-*p*-terphenyl.[70]

3.1.3 Organometallic Bonds

Organometallic bonds are metal–carbon bonds (M−C), whereby inorganic metal species interact with organic molecules. The character of the organometallic bond is classified as ionic and covalent.[80] The respective contribution to the bond depends on ionization potential of the metal, the size of the ion, properties of the ligands and their structure.[81] Usually, the metal atom is more electropositive than the carbon atom of the molecular backbone. The covalent character decreases with increasing difference in electronegativity between metal and organic component.

The formation of M−C bonds is already known from organometallic chemistry, a subfield of coordination chemistry.[82] Nowadays, organometallic bonds are also identified as a reaction intermediate in on-surface Ullmann coupling under UHV conditions.[57, 83] Subsequent to dehalogenation, the surface stabilized radicals (SSRs) couple to adatoms of the metal substrates, resulting in the formation of C−M bonds. Depending on the substrate material, the formed organometallic structures can be disordered *e.g.* on copper,[83, 84, 85] but also partially ordered *e.g.* on silver [86]. On gold, on the other hand, organometallic intermediates are only rarely observed.[87]
Compared to classic C−C bonds with a typical length of ∼0.15 nm and a bond energy of ∼350 kJ mol^{-1},[88, 89] metal–carbon bonds are weaker (∼45 - 200 kJ mol^{-1}) and the corresponding bond length is significantly longer (∼0.2 nm).[13, 90, 91] The difference between organometallic and covalent interlinks can clearly be distinguished in STM measurements as shown in Fig. 7.2 (chapter 7).

For RT deposition of 1,3,5-tris(*p*-carboxyphenyl)benzene (BIB) on Cu(111) (Fig. 3.2) and Ag(111) (*cf.* chapter 7), for example, usually linear intermolecular C−M−C bonds are formed. Thereby, two SSRs interlink *via* a common copper or silver adatom, respectively. The STM images in Fig. 3.2 show the same sample area, however, with different contrast resulting from different bias voltages. In Fig. 3.2(a) the copper atoms are clearly resolved as bright dots, whereas the organic backbones appear as depressions. In Fig. 3.2(b), on the other hand, the copper adatoms are barely visible and the organic backbones appear as protrusion. In addition to the organometallic network also the split-off halogen atoms are discernible as bright dots in the STM image (Fig. 3.2(b)).

In accordance with previous studies, RT deposition of BIB onto Cu(111) results in the formation of disordered organometallic structures (Fig. 3.2), whereas on Ag(111) a great variety of coexisting partly ordered arrangements is obtained (Fig. 7.1, chapter 7). The observation of partially ordered structures on Ag(111) can be seen as indication for the reversibility of C−Ag bonds at room temperature enabling structural rearrangement. On Cu(111), however, only disordered structures are formed, suggesting the irreversibility of C−Cu bonds. The binding energy of C−Cu is normally higher compared to C−Ag bonds.

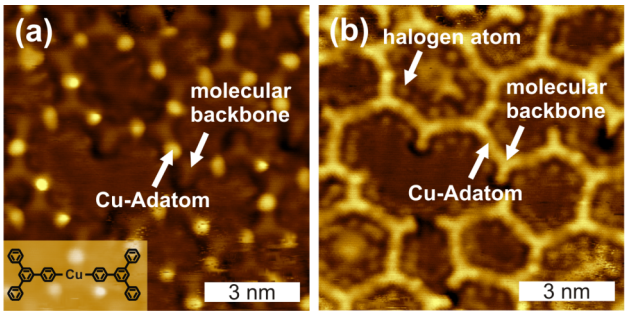

Figure 3.2: STM images of organometallic structures prepared by RT deposition of BIB onto Cu(111). In both images the organic backbone as well as the Cu adatoms are clearly discernable. The inset in (a) shows schematically the corresponding structure of the organometallic interlink. ((a) +2.2 V, 6.2 pA, (b) +1.3 V, 6.2 pA)

3.1.4 Covalent Bonds

Covalent bonds are directional and stable chemical bonds between atoms with a bond strength of ∼200 - 800 kJ mol^{-1}.[64] The corresponding bond length is characteristic for every covalent bond and is usually in the range of ∼0.07 - 0.2 nm.[64] The character of covalent bonds is influenced by the electronegativity of the binding partners. Binding of unequal elements *e.g.* HCl leads to polar covalent bonds, whereas nonpolar covalent bonds are formed between atoms of the same element *e.g.* H_2.

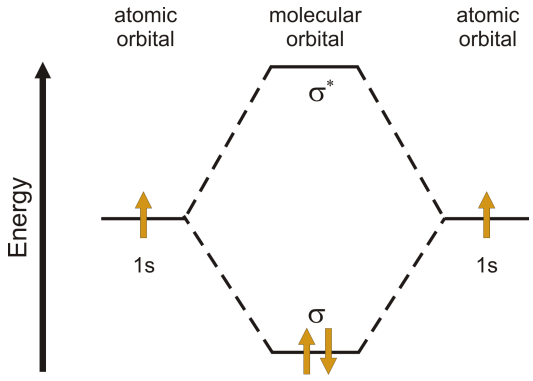

Figure 3.3: Energy levels of the initial 1s atomic orbitals as well as of the bonding (σ) and antibonding (σ^*) orbitals formed in the hydrogen molecule. Adapted from Ref. [92]

Covalent bonding results from the overlap of atomic orbitals (AO) of different atoms forming molecular orbitals (MO).[93, 94] The overlap of the atomic orbitals can be constructive or destructive, leading to bonding and antibonding MOs, respectively.[93, 95] Bonding MOs feature an enhanced electron density between the two nuclei. In this region, the electrons interact simultaneously with both nuclei and stabilize the molecule. Antibonding MOs, on the other

hand, exhibit a diminished electron density between the nuclei and destabilize the molecule by weakening the bond. Compared to the original atomic orbitals, the energy of bonding MOs is lower and of antibonding MOs is higher. In Fig. 3.3 the corresponding energy level diagram is schematically shown for the formation of H_2.

Covalent bonds are characterized by geometric parameters, whereby two major types of bonds are distinguished: σ- and π-bonds.[93, 96] Atomic orbitals form σ-bonds by head-to-head or end-to-end overlap, leading to an increase of electron density along the bond axis. π-bonds, instead, resulting from the formation of molecular orbitals by lateral or side-to-side overlap of atomic orbitals. Consequently, the electron density is localized in regions above and below the connecting axis of the nuclei. π-bonds are weaker than σ-bonds and are only formed when two atoms are already connected by a σ-bond.

In chapter 6 different on-surface polymerization reactions are investigated to form covalent bonds between molecular building blocks. Thereby, covalent bonds can be identified in STM images by means of their unique, relatively short bond length compared to other intermolecular interactions, as shown in Tab. 3.1.

Table 3.1: Summary of typical interaction energies and bond lengths for different types of intermolecular interactions. (The corresponding references are given in the main text.)

Intermolecular bonds	Energy range ($kJmol^{-1}$)	Bond length (nm)
Hydrogen bonds	~2 - 40	~0.12 - 0.32
Halogen bonds	~33	~0.35 - 0.40
Organometallic bonds	~45 - 200	~0.20
Covalent bonds	~200 - 800	~0.07 - 0.20

3.2 Thermodynamics

Self-assembly in general, but also on surfaces can be a thermodynamically controlled process. The system evolves towards a minimum of Gibbs free energy ΔG by a multitude of bond formation and bond breaking processes. Under isothermal and isobaric conditions the change in free energy ΔG is expressed as

$$\Delta G = \Delta H - T\,\Delta S \tag{3.1}$$

where ΔH is the enthalpy change and ΔS the entropy change of the system. Under UHV conditions, adsorbed molecules on a surfaces can be considered as a thermodynamic system. Molecules form ordered assemblies *via* intermolecular interactions, which constrains their freedom of motion, causing a reduction of the total entropy

$\Delta S < 0$.[75] On the other hand, the overall enthalpy of the system is reduced by optimization of molecule–molecule and molecule–substrate interactions. To reach the thermodynamic equilibrium a high degree of reorientation and rearrangement has to take place. The formed structures are very often long-range ordered assemblies.
The formation of thermodynamically stable structures requires $\Delta G < 0$. Weakly or moderately bound complexes are often unstable due to the dominance of $-T\,\Delta S$ over ΔH, resulting in $\Delta G > 0$. However, relatively strong interactions with a more negative ΔH promote thermodynamically stable assemblies with $\Delta G < 0$.

Hydrogen or halogen bonds, for example, permit rearrangement and error correction processes already at room temperature. These types of intermolecular interactions allow molecules to self-assemble into their thermodynamic equilibrium and to form long-range ordered structures. In contrast to hydrogen or halogen bonds, covalent bonds are usually irreversible, impairing error correction processes and thus the formation of thermodynamic equilibrium structures. The corresponding structures often suffer from a high defect density and rather small domain sizes.[84, 97]

Actually, self-assembled structures are only thermodynamically stable within a certain range of pressure and temperature due to the temperature and pressure dependence of ΔG.[98] Consequently, phase transitions between different structures can occur upon variation of pressure and/or temperature.
In general, molecular self-assembly can take place at the liquid/solid as well as at the vacuum/solid interface. At the liquid/solid interface, the structure formation is determined by a dynamic equilibrium between adsorbed and dissolved molecules. At the vacuum/solid interface, on the other hand, self-assembled structures are not stabilized by an adsorption/desorption equilibrium. Accordingly, changes in the ambient pressure would hardly affect the structure formation on the surface. At the liquid/solid interface, molecular self-assembly can be influenced by varying the concentration of the molecular building blocks in solution. Thereby, the adsorption/desorption equilibrium may be changed resulting in the emergence of different structures, which are stable under the altered conditions.[12] In other words, at the liquid/solid interface solution concentration and temperature can be used to initiate phase transitions, whereas at the vacuum/solid interface only the temperature significantly influences the structure formation. For instance, phase transitions from a porous to a densely packed structure are observed for 1,3,5-tris(*p*-carboxyphenyl)benzene (BTB) in nonanoic acid at the liquid/solid interface upon increasing the substrate temperature.[68]

3.3 Kinetics

The term molecular self-assembly implies the formation of structured arrangements under equilibrium conditions.[13, 54] However, the system can also be trapped in a

state far from thermodynamic equilibrium.[12, 13] In this case, the thermal energy is insufficient to activate, for example, dynamic processes or to disintegrate non-equilibrium arrangements. The kinetically stabilized phases are metastable and can rearrange with a marginal rate over time into thermodynamically more stable structures.[12, 98] According to the Arrhenius equation, the rate constant k for thermally activated processes is described as

$$k = k_0 e^{-E_{\text{barrier}}/RT} \tag{3.2}$$

where E_{barrier} is the activation energy, T the temperature and k_0 the pre-exponential factor.[98]
Under UHV conditions the growth of adsorbed molecules into structures is primarily influenced by their deposition F and diffusion rate D on the surface.[54, 99] Consequently, the ratio of diffusion to deposition rate D/F is characteristic for the type of growth. For large ratios, the molecules have enough time to rearrange and to reach the thermodynamically favored equilibrium structure. Small ratios, *i.e.* high fluxes, on the other hand, can result in the formation of kinetically trapped structures, when a local energetic minimum is reached faster than the thermodynamic global minimum.

Kinetic control also provides the possibility to influence the structure formation by the specific choice *e.g* of external growth parameters. Each process is associated with a characteristic energy barrier, whereby some are energetically more costly than others. This energetic hierarchy of the barriers can be used to selectively activate or suppress processes and to influence the structure growth.[99] The influence of different kinetic reaction parameters on the morphology and quality of covalent networks, for example, was studied for on-surface Ullmann coupling of BIB on Au(111) in section 6.2.

Chapter 4

On-Surface Synthesis of 2D Polymers

In contrast to self-assembled structures, 2D polymers are stabilized by strong covalent bonds between the molecular building blocks. Hence, covalently linked 2D structures exhibit unprecedented chemical and mechanical stability. In combination with their tunable electronic properties, 2D polymers are promising candidates for applications in (opto)electronic devices.[17, 18]
The following chapter aims to provide a detailed understanding of the network formation process during on-surface polymerization. In this context, the characteristics of different polymerization reactions are highlighted. Furthermore, effects of synthesis parameters and substrate properties on the network formation process, morphology, and quality are exemplified by density functional theory (DFT) calculations and Monte Carlo (MC) simulations.

4.1 Polymerization Reactions

In principle, a variety of chemical reactions can be applied for the synthesis of covalently linked structures on surfaces. In this section, a summary of commonly used coupling reactions is given with a focus on polymerization of covalent 2D nanostructures on surfaces, comparing conventional solution chemistry to the corresponding on-surface variant. The detailed discussion of different polymerization reactions shall provide a deeper understanding of the underlying reaction mechanisms.

4.1.1 Ullmann Coupling

Ullmann coupling is a well-known solution coupling reaction for aryl halides in the presence of copper as catalyst (Fig. 4.1).[100] The assumption that the reaction occurs on the surface of the copper catalyst, motivated the transfer of the Ullmann reaction to single crystal copper substrates under UHV conditions.

Nowadays, the on-surface variant of Ullmann coupling is an established route for the tailored synthesis of 1D and 2D nanostructures. The reaction is extremely versatile due to the possibility of pre-defining the topology of covalent structures by the substitution pattern of the precursor. 1D structures, such as poly(para-phenylene) chains [19] or graphene nano-ribbons [57], are fabricated from two-fold halogenated building blocks, whereas for 2D networks multiply halogenated monomers are used [84, 101].

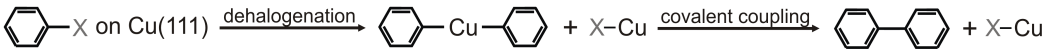

Figure 4.1: Reaction scheme of on-surface Ullmann coupling. Subsequent to deposition of aromatic halides on Cu(111), the halogen atoms are split off and an organometallic intermediate is formed. Finally, the organometallic intermediate releases the Cu atom and recombines to biphenyls, whereby the halogen atoms are chemisorbed on the surface.

On-surface Ullmann coupling was intensely studied for iodobenzene and bromobenzene on a Cu(111) surface to identify the exact pathway of the reaction.[102, 103] The formation of biphenyls occurs in two steps (Fig. 4.1): First, the dehalogenation of the aryl halides takes place subsequent to deposition, whereby the split off halides chemisorb on the surface. The dehalogenated monomers form so called surface-stabilized radicals (SSRs) as an intermediate, which are characterized by their unpaired electrons.[104] The radicals are stabilized on the surface by coupling at their dehalogenated sites to the free electrons of the surface. On Cu(111) the SSRs can bind to Cu adatoms and form metastable organometallic structures based on carbon–metal–carbon bonds. In a second reaction step at increased temperatures, the covalent coupling takes place. Thus, the organometallic bonds are converted into covalent bonds by the release of the Cu adatoms leading to the formation of biphenyls. In the resulting covalent structure the buildings blocks are interlinked at their previously halogenated sites as shown in Fig. 4.1.

Functional Groups

The initial step of on-surface Ullmann coupling is the dissociation of the halogen atoms X from the precursor. In comparison to the C−C bonds of the molecular backbone, the carbon–halogen (C−X) bonds possess a lower binding energy. The difference between the binding energies allows the selective dissociation of the comparatively weaker C−X bonds without destroying the molecular backbone. These characteristics facilitate the formation of SSRs, which can subsequently couple *via* covalent bonds to organic nanostructures. To this end, the molecular building blocks are often functionalized with bromine,[83, 105] iodine,[56, 106] or combinations of both [107, 108]. Chlorine and fluorine, on the other hand, are rather occasionally investigated side groups in context of on-surface polymerization.[103, 109]

The strength of C−X bonds depends on the type of halogen and increases in order of I < Br < Cl < F. The bond dissociation energies for the dehalogenation of C_6H_5−X, for example, are 280 kJ mol^{-1} for iodine, 351 kJ mol^{-1} for bromine, 406 kJ mol^{-1} for chlorine, and 531 kJ mol^{-1} for fluorine.[110] The bond dissociation energy is specific for the type of halogen resulting in different activation temperatures for the respective dehalogenation. In this context, DFT simulations reveal a clear difference of ∼0.3 eV between the energy barriers E_{barrier} for deiodination and debromination on Au(111), Ag(111) and Cu(111).[111] The calculated energy barriers E_{barrier} from Ref. [111] are summarized in Tab. 4.1.

Table 4.1: Computed reaction energies E_{react} and energy barriers E_{barrier} for the dehalogenation of bromobenzene and iodobenzene by means of DFT. Adapted from Ref. [111].

Substrate	Debromination		Deiodination	
	E_{react} (eV)	E_{barrier} (eV)	E_{react} (eV)	E_{barrier} (eV)
Cu(111)	-0.68	0.66	-0.81	0.40
Ag(111)	-0.50	0.81	-0.67	0.52
Au(111)	-0.16	1.02	-0.44	0.71

Accordingly, tailored functionalization of molecular building blocks with different types of halogen atoms can be used to steer the on-surface polymerization reaction. The different halogens can selectively be split off in order of their increasing bond dissociation energies by annealing at the corresponding activation temperatures. In section 6.2, hierarchical polymerization is studied on a Au(111) surface using an asymmetrical aromatic precursor functionalized with iodine and bromine (1,3-bis(*p*-bromophenyl)-5-(*p*-iodophenyl)benzene, BIB). Thereby, iodine is split off after RT deposition, whereas debromination requires further annealing above 175 °C.

Role of Catalytically Active Substrates

In addition to the type of halogen, on-surface Ullmann coupling relies also on the catalytic properties of the metal substrate. Depending on the substrate material, different annealing temperatures are required to split off the halogen substituents. In addition to the prototypical copper surface, also (111) facets of silver and gold are investigated as catalytically active surfaces. Recent studies have shown, that analogous coupling reactions can be performed on silver [83] or on gold substrates [112].

DFT calculations of Ullmann coupling on different substrates indicate, that the energy barrier E_{barrier} as well as the reaction energy E_{react} follows the trend of the catalytic reactivity of the surfaces.[111] E_{barrier} and E_{react} increase for debromination and deiodination in order of Cu(111), Ag(111), and Au(111) (Tab. 4.1).[111] Due to

the lower energy barrier E_{barrier} on Cu(111), the complete dissociation of iodine [56] and bromine [83, 84] can take place already at RT. This effect is also observed for BIB on Cu(111) (*cf.* Fig. 3.2, subsection 3.1.3), where organometallic structures of SSRs are already obtained subsequent to RT deposition indicating complete deiodination and debromiation. On Ag(111) and Au(111) additional thermal activation can become necessary to facilitate the C−X bond dissociation arising from the increased E_{barrier} in comparison to Cu(111). RT deposition on Ag(111) and Au(111) surfaces, already results in spontaneous deiodination,[106, 108] whereas bromine is partially split off on silver,[85, 108] and not at all on gold [112]. Accordingly, Cu(111) has the highest activity for dehalogenation. The dehalogenation progress of deiodination and debromination after RT deposition on Cu(111), Ag(111), and Au(111) is summarized in Tab. 4.2. For each combination also the resulting molecular structures are specified.

Table 4.2: Summary of the dissociation progress in debromination and deiodination at RT on Cu(111), Ag(111), and Au(111). For each parameter set also the resulting structures on the corresponding surfaces are given.

Substrate	Debromination	Deiodination
Cu(111)	Complete	Complete
	→ Protopolymers	→ Protopolymers
Ag(111)	Partial	Complete
	→ Protopolymers	→ Protopolymers
Au(111)	No	Complete
	→ Self-assembly	→ Covalent Networks

On metal substrates, the network formation process is also influenced by the adatom reactivity. Subsequent to dehalogenation, the formed SSRs can bind to the metal adatoms on the surface and form metastable organometallic structures, which are commonly observed on copper and silver substrates. The conversion of organometallic into covalent bonds can be activated by thermal annealing. On copper substrates, however, this is not always possible due to the higher thermal stability of the C−Cu bonds compared to the covalent bonds of the molecular backbone. The temperatures required for the finial polymerization can already break the C−S bond of the thiophene ring in the molecular backbone resulting in the formation of C−S−Cu bonds.[85]

4.1.2 Homo-Coupling of Terminal Alkynes

Homo-coupling of terminal alkynes was first reported by C. Glaser in 1896 (Fig. 4.2).[113] Phenylacetylene dehydrogenates in the presence of CuCl and forms copper(I) phenylacetylide. Exposure to air results in oxidative dimerization of this intermediate to diphenylacetylene interlinked by a butadiyne bridge.[114]

The original Glaser coupling was substantially modified by Hay in 1962 [115] who performed acetylenic coupling in presence of the bidentate ligand N,N,N',N'-tetramethylethylenediamine (TMEDA). Under these conditions, the coupling reaction proceeds considerably faster and produces phenylacetylene with a yield of 97%.[115] Additionally, TMEDA has the advantage to be very dissolvable in many organic solvents.

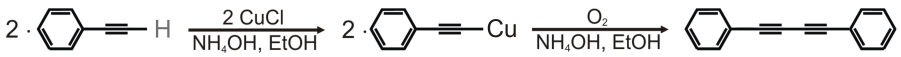

Figure 4.2: Reaction scheme of Glaser coupling.[113] Copper mediated coupling of phenylacetylene leads to the formation of diphenyldiacetylene *via* a copper-phenylacetylide intermediate.

Later, the dimerization of terminal alkynes was co-catalysed by Pd/Cu. In addition to the dimerization, however, side reactions were already reported resulting in the formation of cross-linked enynes in small amounts.[116, 117, 118] Interestingly, the use of dicobalt octacarbonyl as catalyst facilitates the trimerization to benzene instead of forming a butadiyne bridge *via* dimerization.[119] In contrast to cross-coupling and dimerization, the trimerization is not accompanied by the release of hydrogen as byproduct.

Recent studies reported the transfer of the coupling reaction to various single-crystal metal surfaces under UHV conditions.[120, 121, 122, 123, 124] On Cu(100) and Cu(110) coupling of acetylene is highly selective, but yields butadiene and cyclooctatetraene as byproducts on Cu(111).[120] A variety of side reactions is also observed for 1,3,5-triethynylbenzene (TEB) and 1,3,5-tris-(*p*-ethynylphenyl)benzene on Ag(111). The polymerization results in irregularly branched structures, whereby up to five monomers can be covalently interlinked.[124] Homo-coupling of terminal alkynes on Ag(877), however, inhibits side reactions and improves the regioselectivity.[124] On the stepped silver surface, 4,4"-Diethynyl-1,1':4',1"terphenyl is parallel aligned to the step edges, whereby the dimerization becomes favored over branching side reactions. Contrary on Au(111), polycyclotrimerization is reported for coupling of 4,4'-diethynyl-1,1'-biphenyl, resulting mainly in the formation of two isomeric configurations interlinked by a trisubstituted benzene derivative.[123]

The observation of various side reactions for on-surface coupling of terminal alkynes induced the requirement for a deeper understanding of the underlying reaction mechanism to improve the regioselectivity. In this respect, DFT calculations based on transition state calculations are used to resolve the reaction pathway of TEB dimerization on Ag(111).[104] Interestingly, covalent coupling between two precursors is proposed as the initial reaction step and not the expected dehydrogenation of the monomers. The thereby formed dimer represents an intermediate reaction product which undergoes two subsequent dehydrogenation steps until the final covalent

structure is reached.[104] This reaction mechanism is suggested for Ag(111), however, the reaction pathway may be completely different on other substrates or in solution chemistry.

4.1.3 Condensation Reaction

Polymerization of reactants or reactive groups can also proceed as a condensation reaction. Thereby, at least two molecules with appropriate functional groups covalently interlink to a single main product under the release of a small byproduct *e.g.* water, ethanol, or ammonia. In this respect, the interlinking of identical molecules is known as self-condensation.

In this context, especially the condensation of bronic acid building blocks gained research interest for the solvothermal synthesis of 2D and 3D covalent organic frameworks (COFs).[125, 126] Thereby, three boronic acid groups cyclotrimerize to a six-membered boroxine ring (B_3O_3) accompanied by the elimination of three water molecules (Fig. 4.3). The solvothermal synthesis is performed in a closed reaction system to sustain the availability of H_2O for maintaining reversible reaction conditions to allow self-repair processes. Additionally, the nucleation of crystalline materials is facilitated by the use of solvents with sparse solubility for the precursor monomer.[125] The combination of poor solvents and a closed reaction system results in the growth of crystalline 2D and 3D materials with high yield. The condensation of 1,4-benzenediboronic acid (BDBA) results in layered covalent organic frameworks composed of planar hexagonal sheets. The single layers are shifted relative to each other obtaining an AB-stacking order similar to graphite.[125]
Besides bronic acid condensation, also other reversible condensation reactions have been explored for the synthesis of layered 2D and 3D COFs.[127] Imine-linked 2D and 3D COFs, for example, are synthesized by interlinking aldehydes (–CHO) with amines ($–NH_2$).[128, 129] This condensation reaction results in the formation of imine bonds (–CH=N–) and the release of H_2O. In contrast to BDBA, the condensation of 1,3,5-triformylbenzene and 1,4-diaminobenzene leads to the formation of layered 2D COFs with eclipsed stacking.[128]

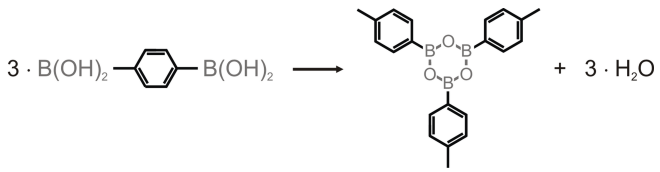

Figure 4.3: Reaction scheme of boronic acid condensation. Three boronic acid groups combine to a boroxine ring under the release of water.

Analogous, to surface-assisted Ullmann and Glaser coupling, boronic acid condensation is also successfully transferred to surfaces. In contrast to on-surface Ullmann

coupling, however, two-fold funcionalized monomers such as BDBA already yield 2D networks due to the cyclotrimerization of three boronic acid groups. Zwaneveld *et al.* employed the condensation reaction for the synthesis of 2D covalent networks on Ag(111) surfaces under UHV conditions. The formed byproduct (H_2O) immediately desorbs from the surface, disabling reversible self-repair processes. Hence, the resulting networks are affected by high defect densities.[130]

4.2 Surface Mobility and Coupling Affinity

The synthesis of extended and regular covalent networks is still a major challenge in surface chemistry. This is partially related to the fact, that the formation of covalent bonds is usually an irreversible process, which inevitably leads to the formation of irregular structures with high defect densities. For the improvement of the network quality, first the network formation process has to be understood. This knowledge would facilitate the possibility to influence and to control on-surface reactions in order to obtain the desired reaction product. In this context, computational studies such as DFT and MC simulations can help to resolve details in the reaction pathway and to design possible molecular precursors.

In section 4.1 it was already shown, that different polymerization reactions can be used for the synthesis of 2D networks. In principle, two different reaction concepts can be distinguished: during the polymerization process, the functional groups either couple with each other under the release of a byproduct or are split off and form SSRs. In a subsequent coupling step, the SSRs can bind to surface adatoms forming metastable organometallic structures or directly interlink by covalent bonds. Both reaction mechanisms can occur over several steps and are limited by the rate of the slowest reaction step, determining the overall reaction rate.[131] On-surface Ullmann coupling, for example, depends on the dehalogenation or coupling step, but also on the diffusion on the surface. Coupling of small molecules, *i.e.* halogen-based benzene derivatives, is expected to be limited by the dehalogenation step, whereas during polymerization of larger molecules, *i.e.* halogen-substituted macrocycle cyclohexa-*m*-phenylene, rather diffusion or coupling act as rate-limiting step.[56, 111]

In general, the reaction rate ν of thermally activated processes such as diffusion or coupling can be obtained by the Arrhenius relation (Eq. 4.1), where T is the temperature and E_{barrier} the reaction barrier for the corresponding process. Based on transition state theory, the exponential prefactor A is commonly approximated as $10^{13}\,\mathrm{s}^{-1}$ at room temperature.[104, 111, 132, 133]

$$\nu = A\, e^{-E_{\mathrm{barrier}}/k_{\mathrm{B}}T} \tag{4.1}$$

4.2.1 Monte Carlo Simulations

Reprinted with permission from J. Eichhorn, D. Nieckarz, O. Ochs, D. Samanta, M. Schmittel, P. S. Szabelski, and M. Lackinger. On-Surface Ullmann coupling: The influence of kinetic reaction parameters on the morphology and quality of covalent networks. *ACS Nano.* 8 (2014), 7880-7889. Copyright 2014 American Chemical Society. The Monte Carlo simulations were performed by P. S. Szabelski and co-workers.

In principle, Monte Carlo (MC) simulations are suitable to investigate the network formation process on surfaces for different building blocks and reaction parameters. However, they are limited to ideal structures and do not account for defects such as irregular pores, *i.e.* tetragonal, pentagonal, heptagonal, and octagonal pores.

The network growth is simulated on a lattice of equivalent adsorption sites and is performed by iterative addition of molecules.[134] Initially, a seed molecule is fixed at the center of the grid and serves as a nucleation site for the network growth. Additionally, an annular launch zone around the seed can be defined, where the molecules start surface diffusion at a random position within the launch zone. On the simulated lattice, the molecules are free to perform a random walk, *i.e.* with equal probability for short-range jumps and in-plane rotation. After encountering the growing network at a possible binding site an uniformly distributed random number $\in (0, 1)$ is generated, which can be compared to the preset coupling probability $0 \leq p \leq 1$.[134] Relatively lower values result in irreversibly incorporation into the cluster, otherwise, further molecular diffusion and rotation are allowed.
The coupling probability p describes the affinity of the molecules to bind to the already formed molecular aggregate, which is interpreted as the ratio between the coupling rate v_c and the total reaction rate of coupling and diffusion $v_c + v_d$:

$$p = \frac{v_c}{v_c + v_d} \quad \text{with} \quad 0 \leq p \leq 1 \tag{4.2}$$

Thus, low coupling probabilities ($p \approx 0$) correspond to high surface mobility of the monomers compared to the incorporation probability into the growing network. High coupling probabilities ($p \approx 1$), on the other hand, indicate immediate and irreversible C−C bond formation once the molecule is integrated into the network.

In the context of on-surface Ullmann coupling, MC simulations are performed for different coupling probabilities p, to investigate the network growth under different reaction conditions such as different substrate materials, molecular building blocks, or annealing temperatures. MC simulations of cyclohexa-*m*-phenylene radicals (CHPRs) by Bieri *et al.*, for example, reveal that the network morphology changes from branched to compact for decreasing coupling probabilities p.[56] Low coupling

probabilities promote monomer diffusion along the island and allow equilibration into energetically more favorable structures, which often results in more densely packed networks.

For the polymerization of CHPR, Bieri *et al.* matched the MC simulations with experimentally grown networks on Cu(111), Ag(111) and Au(111).[56] The STM images clearly show that the morphology of the network improves from Cu(111) to Ag(111), whereby more densely packed structures are obtained on Ag(111). These combined studies underpin the important role of the substrate in the network formation process concerning the corresponding diffusion and/or coupling properties. Thereby, diffusion-limited processes result in branched networks, while densely packed structures are obtained for coupling-limited processes.

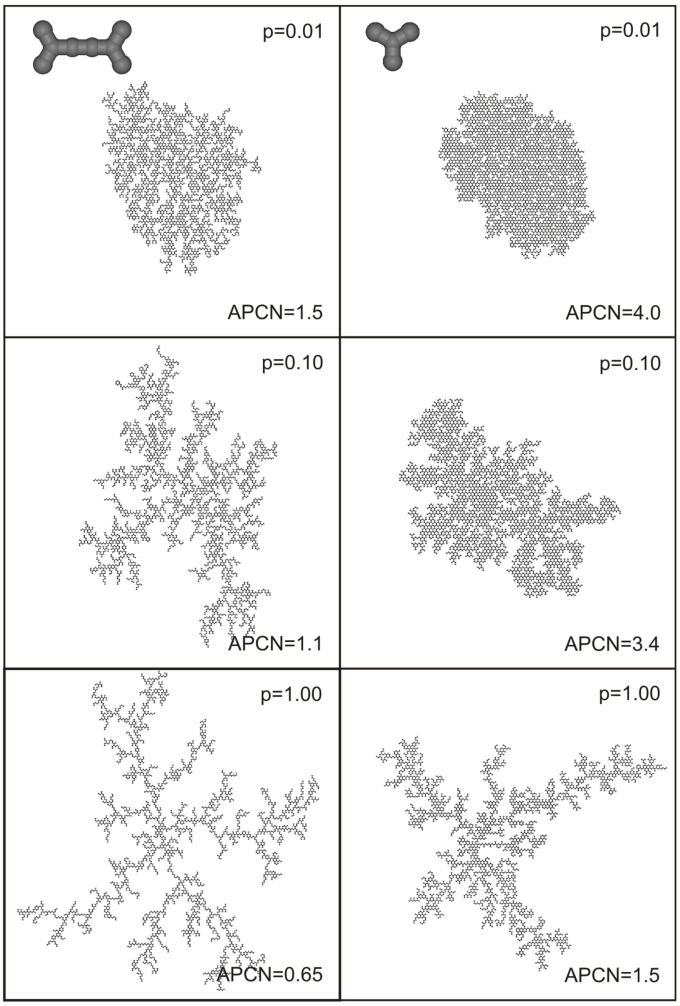

Figure 4.4: MC simulations of the network growth in on-surface polymerization using tripod- and dumbbell-shaped molecular precursors. For both monomers the network morphology changes from close packed to branched with increasing coupling probability p. The APCN is given as a measure for the compactness of the networks. (Reprinted with permission from Ref. [134]. Copyright 2014 American Chemical Society.)

MC simulations by Eichhorn *et al.* investigated 1,3-bis(*p*-bromophenyl)-5-(*p*-iodophenyl)benzene (BIB) and 3,3"',5,5"'-tetra(*p*-bromophenyl)-1,1':4',1":4",1"'-quaterphenyl (TBQ) as molecular building blocks, which are modeled as tripod- and dumbbell-shaped molecules. The resulting network structures of both monomers are summarized in Fig. 4.4 for different coupling probabilities p with values of 0.01, 0.1 and 1. The network morphologies are branched for higher coupling probabilities, whereas more compact networks are obtained for lower coupling probabilities. The dependence of the network morphology on the coupling probability is similar to the observations reported by Bieri *et al.* for CHPR.
Apart from the coupling probability p, also the average pore coordination number (APCN) of the simulated networks is given in Fig. 4.4. The APCN is defined as the average number of the next nearest neighbors of closed pores, which is used as a measure for the compactness of the networks. The MC simulations exhibit that the ACPN decreases with increasing p for BIB and TBQ. Thereby, the APCNs for the BIB networks are generally higher as for the TBQ structures (Fig. 4.4). Additionally, the simulated network structures contain 1D chains and strings of pores, which are also frequently observed in the corresponding experimental results for the polymerization of TBQ (*cf.* section 6.2, Fig. 6.8).
The MC simulations of BIB and TBQ focus on the influence of the surface temperature on the network quality.[108] Thereby, the enhanced lateral mobility for low coupling probabilities p is assigned to higher surface temperatures and not to different substrate materials as in the MC simulations performed by Bieri *et al.* as discussed above [56]. The comparison of the MC simulation (Fig. 4.4) with the experimental results presented in section 6.2 indicates decreasing coupling probabilities p for decreasing surface temperatures T. However, a direct conversion of p into surface temperatures T is not possible.

4.2.2 Density Functional Theory Calculations

In contrast to MC simulations, density functional theory (DFT)-based transition-state calculations provide detailed insights into reaction pathways for recombination or diffusion processes by determination of reaction energies or barriers.[111, 104]
For the experimental synthesis of 2D nanostructures, Ullmann coupling is already an established route. In particular, halogen-based on-surface Ullmann coupling is also extensively studied by theoretical DFT calculations. Björk *et al.* computationally studied the coupling reaction of iodo- and bromobenzene to biphenyls on the close-packed (111) facets of Au, Ag and Cu.[111] The DFT calculations are performed for all relevant reaction steps such as dehalogenation and coupling of the dehalogenated precursors.
Diffusion of iodo- and bromobenzene can occur by sliding or flipping between two adsorption sites. In sliding diffusion, the monomers have the same orientation before and after the sliding step. During flipping diffusion the molecules turn from one site to another, whereby the orientation of the molecules is reversed. With increasing

molecular size, diffusion in a more planar orientation with respect to the surfaces can be favored and flipping becomes unlikely. The sliding diffusion barriers on Au(111) and Ag(111) are similar, whereas the diffusion barrier on Cu(111) is significantly higher. Calculations of the coupling barriers, instead, indicate smaller barriers for Au(111) and Cu(111) as compared to Ag(111) (*cf.* Tab. 4.1). Based on these DFT results, Björk *et al.* assume that a small diffusion barrier combined with a large recombination barrier might be favorable for the formation of regular ordered 2D networks. In this context, also the reaction rates for the recombination of two SSRs are calculated. The results reveal that on Cu(111) the process depends on the diffusion rate, whereas on Ag(111) the rate-limiting step is assigned to the coupling step.[111] Interestingly, these DFT calculations are in agreement with the results obtained by the MC simulations of CHPR Ullmann coupling,[56] where the diffusion process on Cu(111) and the coupling step on Ag(111) are rate-limiting.

In addition to the identification of reaction pathways, DFT calculations can also be used to optimize isolated molecular structures in geometry and energy as demonstrated in chapter 6 and 7. For this purpose, simple gas phase calculations are performed, whereby the surface influence is often approximated by confining the molecular structures to a planar conformation. The direct comparison of DFT geometry optimized structures and experimental STM data allows the identification of different bonding motifs based on the calculated molecular size and the corresponding intramolecular binding distances.

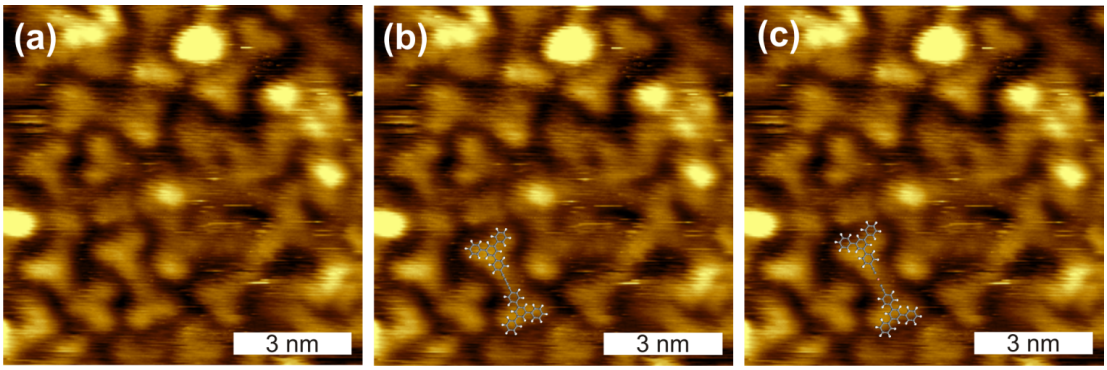

Figure 4.5: (a) STM image (+0.80 V, 1.2 pA) of DEB on Cu(111) after annealing to 300 °C with scaled overlay of DFT geometry optimized structures of (b) the covalently linked dumbbell and (c) the organometallic complex. Obviously, the metal-coordination complex does not match the experimental data. (Copyright (2013) by The Royal Society of Chemistry - Reproduced by permission of The Royal Society of Chemistry from Ref. [135].)

For on-surface coupling of 1,4-diethynylbenzene on Cu(111) (section 6.1), for example, DFT calculations of organometallic complexes and covalently interlinked structures are used to confirm the formation of covalent bonds between the molecular building blocks. The calculated length difference of 0.24 nm between metal-coordinated and covalently interlinked structures can be distinguished in the experimental STM data.

As evident from the scaled overlay of both DFT geometry optimized structures and the STM data (Fig. 4.5), the size of the molecular network is consistent with covalently interlinked structures. In a similar manner, DFT calculations can be used for on-surface Ullmann coupling to distinguish organometallic intermediates from covalently interlinked structures (section 6.2 and chapter 7). In this context, DFT geometry optimized structures also allow to determine the length of not further connected molecular lobes. The calculated length difference of 0.20 nm between brominated and debrominated lobes, for example, facilitates the identification of respective molecular sites within STM images (*cf.* Fig. 6.17, section 6.2).

Chapter 5

Non-Covalent Assembly of Porous 2D Structures

J. Eichhorn, S. Schlögl, B. V. Lotsch, W. Schnick, W. M. Heckl, and M. Lackinger. Self-assembly of melem on Ag(111)-emergence of porous structures based on amino-heptazine hydrogen bonds. *CrystEngComm.* 13 (2011), 5559-5565.

Self-assembly of melem on Ag(111) was studied by scanning tunneling microscopy in ultra-high vacuum resulting in a great structural variety. In total, five porous and two densely packed polymorphs were observed. All structures are stabilized by different intermolecular hydrogen bonds with only few basic motifs. Six out of seven polymorphs can be described by a unified concept.

5.1 Introduction to Two-Dimensional Self-Assembly

Porous surface-supported supramolecular structures have gained substantial interest [53] due to potential applications as host-networks for the incorporation of guests or as organic templates for the size selected growth of metal nanoparticles. In the design of porous organic networks, crystal engineers often take advantage of the relative strength and directionality of hydrogen bonds, whereby porous structures can become favored over densely packed polymorphs. In this respect, the carboxylic acids are a powerful functional group [8] due to the usual formation of double $O_{hydroxyl}-H\cdots O_{carbonyl}$ hydrogen bonds in a self-complementary manner. The high formation probability of cyclic double hydrogen bonds between two carboxylic acid groups allows a certain degree of predictability of the final structure and aides in the design of building blocks in "supramolecular retro-synthesis". Yet, competing interactions in molecular self-assembly of carboxylic acids can also promote alternative hydrogen bond patterns.[136] So far surface-confined hydrogen bonded networks

of carboxylic acids have only been studied on fairly unreactive substrates such as graphite or noble metal surfaces. On more reactive substrates carboxylic acid groups tend to deprotonate. The resulting carboxylate group preferably forms bonds with the substrate or takes part in metal-coordination bonds, when coordination centers become available. For instance, trimesic acid (TMA, 1,3,5-tricarboxybenzene) self-assembles into porous hydrogen bonded flower and chickenwire structures on graphite.[9, 67] Instead, on Cu(100) [137] and even on Au(111) under electrochemical control,[138] TMA adsorbs upright and is anchored through a carboxylate-surface bond. Furthermore, 1,3,5-benzenetribenzoic acid, a larger analogue of TMA also with threefold symmetry, self-assembles into porous networks at the solution-graphite interface,[139] and on Ag(111) for RT deposition under UHV conditions.[140] However, upon annealing to 50 °C and 150 °C respectively, two phase transitions result in more densely packed structures and are explained by a stepwise deprotonation of all carboxylic groups.

So far various 2D porous networks with different pore sizes, shapes, and arrangements have been demonstrated, hence the next rewarding step would be the identification and realization of applications. In this respect, a very intriguing and promising application idea envisages porous networks as growth templates for size selected, surface supported metal nanoparticles. While these metal nanoparticles might be relevant for heterogeneous catalysis, it is well established that the supporting substrate can also contribute to their size dependent catalytic activity. Gold nanoparticles on TiO_2 are a prominent example thereof.[141] A next step towards this application would be to design and study molecular building blocks which bear the potential to self-assemble into porous molecular networks on more reactive substrates. The aim of this study was to investigate supramolecular building blocks equipped with less reactive functional groups which are suitable for self-assembly into hydrogen bonded porous networks on more reactive surfaces. To this end, we targeted the combination of amino groups as hydrogen bond donors and heterocyclic aromatic nitrogen atoms as hydrogen bond acceptors.

In this respect, melamine (1,3,5-triazine-2,4,6-triamine, Fig. 5.1(a)) is an archetypical building block, whose homomeric two-dimensional self-assembly has already been studied on Au(111) [142] and Ag(111).[140, 143] For both substrates two different porous melamine structures are reported, while on Au(111) an additional close packed polymorph is observed. All melamine structures are stabilized by the targeted $N_{amino}-H\cdots N_{triazine}$ hydrogen bonds. However, the pore sizes of melamine networks around ∼1.0 nm are comparatively small,[143] and even inclusion of further melamine molecules as guests within the pores already causes a substantial distortion of the network. The pore size can be increased dramatically by combining melamine with perylene tetra-carboxylic di-imide (PTCDI) as demonstrated both under UHV conditions [144, 145] and at the liquid-solid interface [146]. In the corresponding heteromeric hexagonal monolayer melamine molecules act as vortices, while PTCDI molecules interconnect the vortices by means of triple hydrogen bonds. Yet, the

preparation of heteromeric systems features stoichiometry and deposition sequence as further degrees of freedom and is much more challenging.

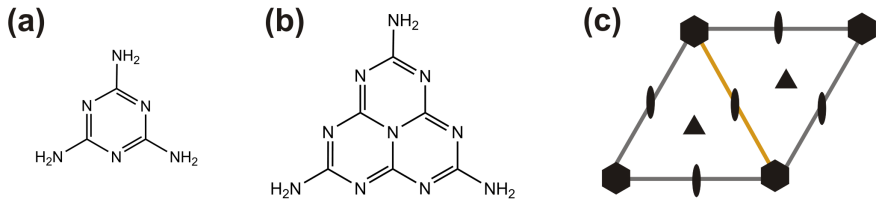

Figure 5.1: Comparison of the chemical structures of (a) melamine and (b) melem; (c) arrangement of symmetry elements within a unit cell for the plane symmetry group *p6*.

A further, effective strategy for increasing the pore diameter is to rely on isotopological networks. In other words, the length of a spacer group or molecule is increased, whereas the underlying blueprint of the structure remains similar. This fundamental principle of crystal engineering has been proven to work in the reticular synthesis of metal organic framework (MOF) bulk crystals,[147] but could also be transferred to 2D networks on surfaces. In this context, already the synthesis of *e.g.* metal-coordination networks based on dicarbonitrile-polyphenyl linker molecules,[148] hydrogen bonded networks of tricarboxylic acids,[8] heteromeric self-assembly of melamine and the homologous series of fatty acids has been reported.[149]

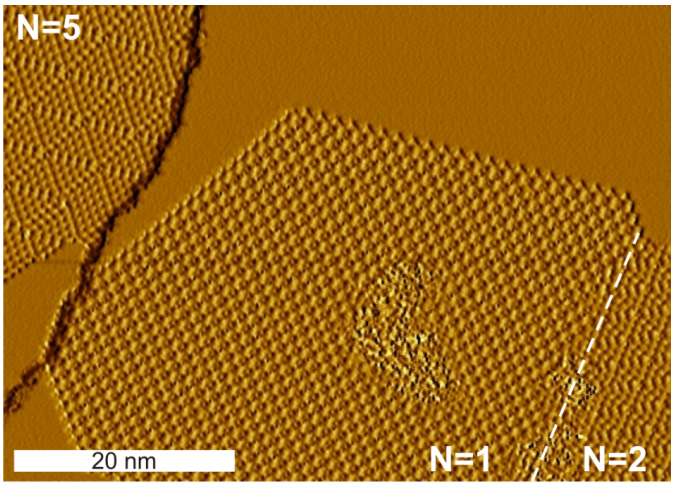

Figure 5.2: Overview STM image (gradient) illustrating the co-existence of three different melem structures (+1.3 V, 39 pA). The dashed line in the lower left corner marks a domain boundary, and domains are labeled with their respective N value (*vide infra*).

Following the proposed approach, starting from melamine (*cf.* Fig. 5.1(a)), we did not increase the length of a linear spacer, but the size of the molecular backbone from triazine (C_3N_3) to heptazine (C_6N_7). Thereby, the symmetric substitution with three amino groups ($-NH_2$) is retained and accordingly also the three-fold symmetry of the molecule. Self-assembly of the resulting compound melem (*cf.* Fig. 5.1(b) for

structure) is anticipated to exhibit similarities with melamine self-assembly with regard to intermolecular hydrogen bonds. On the other hand, the intermolecular bond motifs of the larger compound melem are expected to feature greater versatility and the overall stability of the networks will additionally benefit from the enhanced molecule–substrate interactions. In order to study melem self-assembly, Ag(111) was chosen as substrate, representing an intermediate test bed for a more reactive metal surface.

5.2 Experimental Details

All experiments were conducted under UHV conditions with a base pressure of 3×10^{-10} mbar. Ag(111) single crystal surfaces were prepared by successive cycles of Ar^+-ion sputtering and subsequent annealing at 550 °C. Melem was synthesized by thermal condensation of melamine,[150, 151, 152] and deposited from a home-built Knudsen cell [35] with a crucible temperature of 300 °C onto the Ag(111) surface held at RT. Samples were characterized *in situ* by scanning tunneling microscopy with a VT-STM from *Omicron NanoTechnology* driven by a SPM 100 control electronics from RHK. All measurements were performed at room temperature using electrochemically etched tungsten tips, post-processed in UHV by electron-beam annealing. STM images were acquired in the constant-current mode of operation and images were processed by line-wise leveling only, if not indicated otherwise.

5.3 Self-Assembly of Melem on Ag(111)

Melem (2,5,8-triamino-1,3,4,6,7,9,9b-heptaazaphenalene) is a triply amino substituted heptazine (C_6H_7) ring. The molecule is essentially planar, has a threefold symmetry, and possesses an equilateral triangular footprint. Each baseline of the melem triangle features a D−A−A−D arrangement of hydrogen bond donors (D: NH_2) and acceptors (A: $N_{heptazine}$). Self-assembly of melem on Ag(111) is extremely versatile and reveals a great variety of long-range ordered self-assembled structures. In numerous experimental runs identical preparation protocols are applied yielding various different, mostly coexisting melem polymorphs. An STM overview image depicted in Fig. 5.2 illustrates the co-existence of three different melem structures. In total up to seven different structures emerge, representative STM images of each observed polymorph are reproduced in Fig. 5.3(a)-(g). Among those, five melem polymorphs are porous and two are densely packed. Unit cell parameters, molecular area densities, and number of melem molecules per unit cell are summarized in Tab. 5.1. In all structures melem adsorbs planar, *i.e.* with the heptazine ring parallel to the surface. Melem is very suitable for STM-based self-assembly studies, because of its size and even more its characteristic triangular footprint allows inferring the mutual position and azimuthal orientation of adjacent melem molecules. From the relative arrangement

of interconnected melem molecules it is possible to deduce intermolecular bond motifs. In the following, first the porous and densely packed polymorphs are described, and then the underlying intermolecular hydrogen bond patterns are analyzed.

Table 5.1: Summary of crystallographic parameters of the observed melem polymorphs.

Structure	Lattice parameter (nm) Experiment	Theory	Packing density (Molecules/nm^2)	(Molecules/unit cell)
$N \to \infty$	0.90 ± 0.1	–	1.43	1
Row structure	$a = 0.75 \pm 0.1$	–	2.13	2
	$b = 1.45 \pm 0.1$			
$N = 1$	1.45 ± 0.1	1.45	1.10	2
$N = 2$	2.40 ± 0.1	2.35	1.20	6
$N = 3$	3.12 ± 0.1	3.25	1.42	12
$N = 5$	4.90 ± 0.1	5.05	1.44	30
$N = 12$	10.54 ± 0.1	11.40	1.62	156

Owing to their electron lone pair, nitrogen atoms in supramolecular building blocks can act either as hydrogen bond acceptors or as electron rich ligands for metal-coordination. However, on Ag(111) - without additional supply of reactive extrinsic coordination centers - comparable compounds form only intermolecular hydrogen bonds. Recent examples include terphenyl-4,4"-dicarbonitrile which assembles into a densely packed structure stabilized by N···H−C hydrogen bonds with phenyl hydrogen atoms.[153] N,N-Diphenyloxalic amide self-assembles into a chain structure based on N−H···O hydrogen bonds.[154]
Apparently, intrinsic Ag adatoms are not reactive enough to coordinate supramolecular building blocks through their nitrogen atoms. Since in the present study contrast features indicating coordination by Ag atoms have never been observed and the experimental intermolecular bond distances are consistent with a hydrogen bond scenario, formation of metal-coordination bonds can be excluded.

All porous polymorphs are hexagonal and belong to the chiral plane symmetry group *p6*. In each polymorph the pores feature a similar size (∼0.8 nm inner van der Waals diameter), while the experimental interpore spacing, *i.e.* the lattice parameter, varies from 1.45 nm up to 10.5 nm. From the STM images it is discernable that each pore is bordered by six melem molecules, but also a more detailed analysis of the corresponding intermolecular hydrogen bond motifs becomes possible. With increasing lattice parameter of the porous structures the number of melem molecules per unit cell increases.

Besides the porous polymorphs, two densely packed polymorphs were also observed. One is a relatively simple trigonal structure with one molecule per unit cell, while the second, densely packed polymorph features two molecules per unit cell.

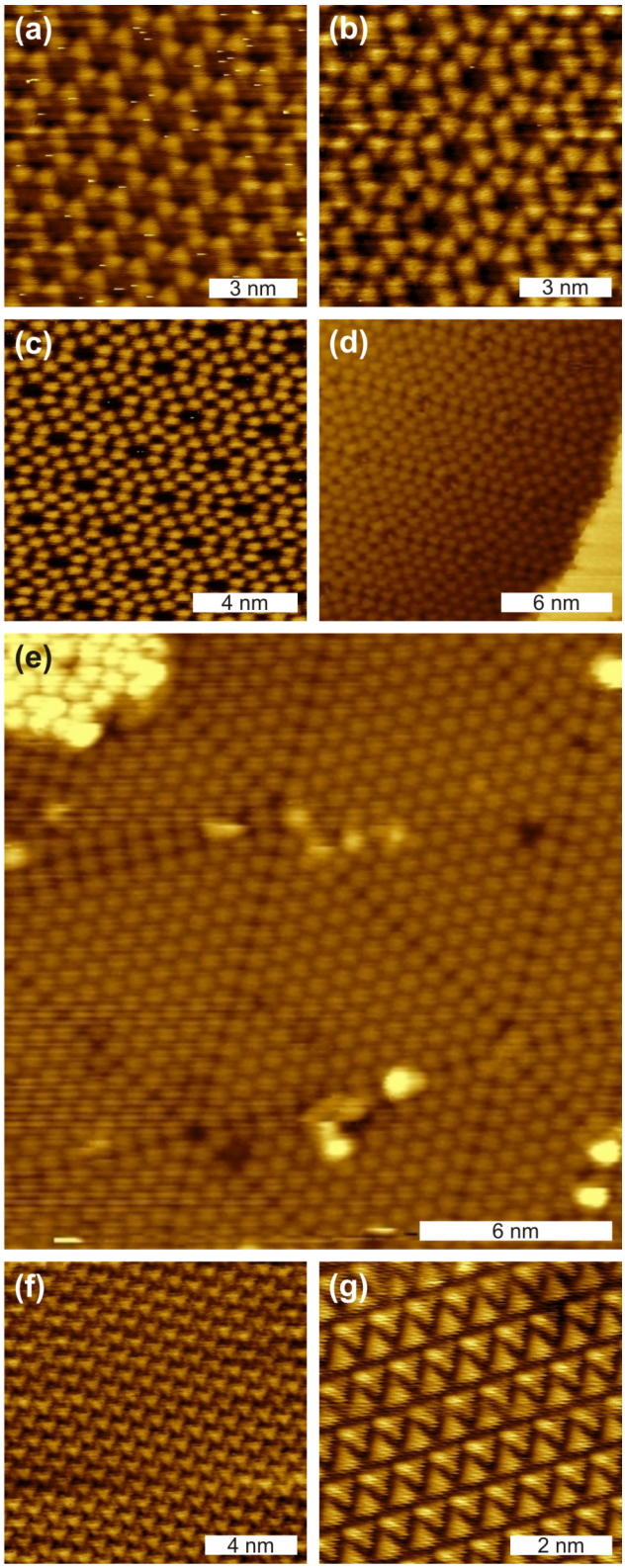

Figure 5.3: High resolution STM images of all observed melem polymorphs on Ag(111). N corresponds to the number of melem molecules along the direct connection between two adjacent pores. (a) $N = 1$ (+0.40 V, 45 pA), (b) $N = 2$ (+1.0 V, 48 pA), (c) $N = 3$ (+0.90 V, 74 pA), (d) $N = 5$ (+1.3 V, 40 pA), (e) $N = 12$ (+2.2 V, 1.1 pA), (f) triagonal densely packed polymporph (+0.10 V, 75 pA), and (g) densely packed row structure (+0.20 V, 97 pA).

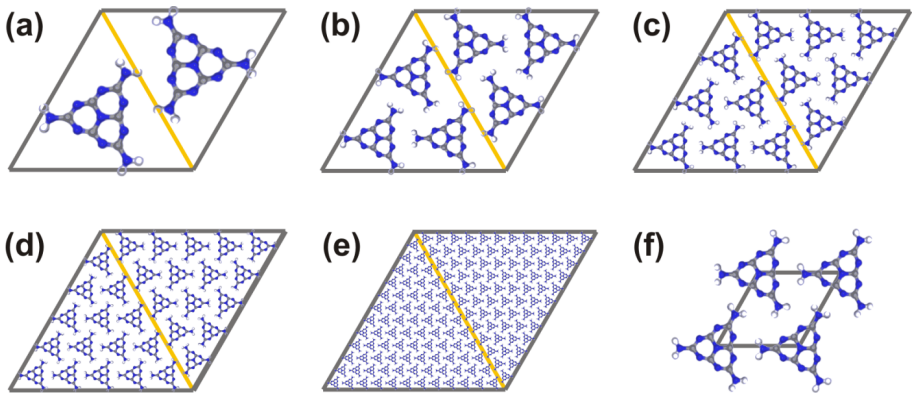

Figure 5.4: Tentative models of the systematic series of melem polymorphs on Ag(111); for each polymorph the arrangement of melem molecules in one unit cell is shown. (a) $N = 1$, (b) $N = 2$,(c) $N = 3$,(d) $N = 5$,(e) $N = 12$, and (a) $N \to \infty$.

Tentative models of all structures based on the STM data are depicted in Fig. 5.4 and 5.7. Although the number of melem polymorphs is comparatively large, all porous structures can be described by a systematic series. Each porous polymorph belongs to the plane symmetry group *p6* (*cf.* Fig. 5.1(c) for unit cell structure), with the sixfold rotation points centered at the pore. In each half of the unit cell (equilateral triangle) melem molecules adopt similar azimuthal orientation and are arranged in a trigonal densely packed structure. On each side, where those triangular halves of the unit cells adjoin, a clearly visible seam (*cf.* Fig. 5.4(d) and (e)) indicates a different type of intermolecular melem–melem bond. The porous polymorphs can also be classified by the number N of melem molecules countable along the direct connection between two adjacent pores. In our experiments, porous polymorphs with $N = 1, 2, 3, 5$, and 12 were observed. Interestingly, only two different intermolecular hydrogen bond patterns account for the structural versatility of the five porous polymorphs. The two basic intermolecular melem–melem bonds are denoted as head-to-tail and side-by-side. Different mutual arrangements of two hydrogen bonded melem molecules were simulated by molecular mechanics (MM), results are depicted in Fig. 5.5. In the head-to-head arrangement (*cf.* Fig. 5.5(a)) the center-to-center distance of melem is ∼0.92 nm, while in the side-by-side arrangement (*cf.* Fig. 5.5(b)) the center-to-center distance amounts to ∼0.82 nm. Both basic hydrogen bond patterns feature two equivalent cyclic N_{amino}–H···$N_{heptazine}$ hydrogen bonds. In the head-to-tail motif both hydrogen atoms of the same amino group bind to two adjacent heterocyclic nitrogen atoms of the heptazine ring through two parallel hydrogen bonds. Since this bond pattern requires two adjacent hydrogen bond acceptors, an equivalent hydrogen bond arrangement is not possible for the smaller analogue melamine. In the side-by-side arrangement, one amino group and one heterocyclic nitrogen atom of each melem molecule form the double hydrogen bonds. Side-by-side was also identified as a preferred binding motif in the 3D crystal structure of melem [155] and is comparable to a similar intermolecular bond pattern

of the smaller analogue melamine.[142, 145, 156] The head-to-tail arrangement features mirror symmetry, while the side-by-side arrangement is two-fold symmetric and chiral. Melem by itself is a non-chiral molecule and even remains non-chiral after adsorption on Ag(111), *i.e.* melem is also non-prochiral. Due to the chirality of the side-by-side hydrogen bond motif, however, each structure which includes this motif becomes chiral. For instance, the arrangement of six melem molecules bordering one pore is based on the side-by-side motif, and thus chiral. A single dimer is already chiral, and resulting six-membered rings can have a clockwise or counterclockwise arrangement. High resolution STM images of both enantiomeric melem arrangements around the pore for the $N = 1$ polymorph are presented in Fig. 5.6, along with the corresponding right- and left-handed models of the melem hexamer. Right- and left-handed forms of the supramolecular arrangement are energetically equivalent, and hence observed with equal probability.

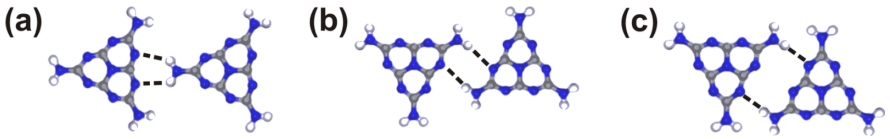

Figure 5.5: Basic melem-melem binding motifs: (a) head-to-tail, (b) side-by-side, and (c) alternative side-by-side. The dashed lines indicate $N_{heptazine}\cdots H{-}N_{amino}$ hydrogen bonds.

In the structurally simplest porous polymorph for $N = 1$, melem molecules are exclusively interconnected side-by-side, whereby each melem molecule binds to three next nearest neighbors on each of its baselines. According to the unit cell structure of *p6*, melem molecules must be centered at the threefold rotational points. Consequently, their mutual distance obeys a fixed relation to the lattice parameter $a{:}d_{melem\text{–}melem} = a/\sqrt{3}$, yielding an experimental value $d_{melem\text{-}melem}$ of $1.45\,nm/\sqrt{3} = 0.84\,nm$. This value is very close to the MM results for the side-by-side arrangement depicted in Fig. 5.5(b). In contrast, the alternative side-by-side arrangement shown in Fig. 5.5(c) yields a smaller $d_{melem\text{-}melem} = 0.74\,nm$, and the corresponding lattice parameter would only account to 1.28 nm, *i.e.* would be smaller than the experimental value. Also the angle of 28.5° between one melem baseline and the unit cell vector of the side-by-side motif in Fig. 5.5(b) is in better agreement with the experimental value of $28 \pm 2°$. Accordingly, we propose the side-by-side arrangement of Fig. 5.5(b) as intermolecular bond scheme in the porous polymorphs.

For the porous polymorphs with $N > 1$ a second hydrogen bond motif is required. As shown in the structural models, melem molecules in each half of the unit cells are exclusively interconnected in the head-to-tail arrangement, whereas at the three boundaries of the unit cell halves the side-by-side arrangement is prevalent. According to the *p6* plane symmetry group, both halves of the unit cell are related by a two-fold rotational symmetry with the symmetry point at the center of the shorter diagonal (*cf.* Fig. 5.1(c)). This two-fold symmetry reflects the symmetry of the

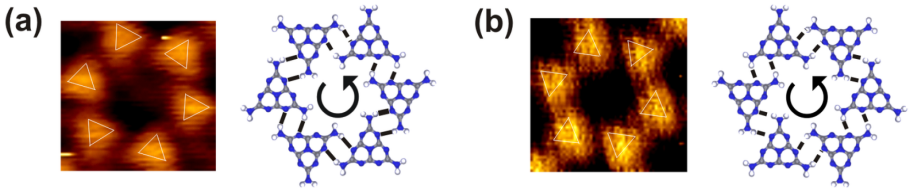

Figure 5.6: STM tophographs and models of chiral melem hexamers based on the side-byside arrangement (a) clockwise and (b) counter-clockwise.

overall arrangement of molecules in the unit cell, but also the symmetry of the side-by-side arrangement. The six melem molecules, which form the pores at the corners of the unit cell, are all interconnected side-by-side. Comparable, internally hydrogen bonded hexamers were also observed for homomeric self-assembly of melamine on Au(111),[142] but also as structural motif in heteromeric self-assembly of melamine and fatty acids.[149]

Starting from the simplest porous polymorph with only two molecules per unit cell and $N = 1$, the next element of the series can be obtained by introducing an additional melem molecule in the direction along the lattice parameter in a head-to-tail arrangement. Accordingly, the lattice parameter increases in increments of 0.9 nm, *i.e.* by the center-to-center distance of the head-to-tail arrangement from one element of the series to the next. The lattice parameter a obeys the following equation:

$$a = 1.45\,\text{nm} + 0.9\,\text{nm} \cdot (N - 1) = 0.55\,\text{nm} + 0.9\,\text{nm} \cdot N \tag{5.1}$$

However, when N increases by 1 not only one melem molecule is added to the unit cell, but a row of melem molecules running parallel to the shorter diagonal. Since the number of melem molecules in this additional row increases with increments of 1, the number of molecules per unit cell as a function of N corresponds to:

$$\text{melem per unit cell} = 2\sum_{i=1}^{N} i = N(N+1) \tag{5.2}$$

From Eq. 5.1 the unit cell area can be deduced as a function of N, and combination with Eq. 5.2 yields the N dependence of the molecular area density:

$$\text{packing density} = \frac{2}{\sqrt{3}} \frac{N^2 + N}{(0.55\,\text{nm})^2 + 0.99\,\text{nm}^2 \cdot N + 0.81\,\text{nm}^2 \cdot N^2} \tag{5.3}$$

From Eq. 5.3 it can be deduced that the molecular area density, and hence the packing density, increases monotonically with increasing N. The area density approaches a constant value of 1.43 molecules per nm^2 for $N \to \infty$. This is obvious since each unit cell of all polymorphs contains only one pore with fixed dimension, while the unit cell area increases monotonically with N. In principle

the intermolecular hydrogen bonds do not impose any restriction on the values of N, and any integer number should be possible. Why experiments yielded only distinct values of N is not clear at this point and a possible influence of the substrate through epitaxial relations cannot be ruled out. Yet, observation of polymorphs with $N = 12$ and accordingly 156 melem molecules per unit cell indicates extensibility of this systematic series up to very large unit cells. On the other hand, dislocations, *i.e.* additional or missing rows in one half of the unit cell in this structure, point towards a predisposition for defects for high N structures.

Similarly, systematic series of porous polymorphs with constant pore sizes but increasing lattice parameters, number of molecules per unit cell, and packing densities have already been observed for TMA on Au(111) [9, 157] and 1,3,5-trikis(4'-carboxylphenyl)-2,4,6-trikis(4'-tert-butylphenyl)-benzene (HPB) on Au(111).[158] In accordance with the melem results, the systematic series of TMA networks is equally based on only two different intermolecular hydrogen bond patterns and two different azimuthal orientations of molecules. The emergence of specific TMA polymorphs was dependent on the surface coverage, where higher coverages yielded more densely packed polymorphs with higher N value. For TMA, neither coexistence of polymorphs nor emergence of structures with large, but finite N, were reported. In contrast to TMA, for melem on Ag(111) structural control, *i.e.* deliberate and exclusive preparation of a specific polymorph could not be achieved by variation of experimentally accessible preparation parameters as surface coverage, deposition rate, or surface temperature. This distinct deviation from the TMA results is exemplified in Fig. 5.2 by the co-existence of three different melem structures for submonolayer coverage. Furthermore, for TMA only the densely packed structure for $N \rightarrow \infty$ was observed, whereas melem self-assembly yielded two different densely packed polymorphs.

Polymorphism is also abundant in monolayer self-assembly at the liquid-solid interface,[136, 67, 139] and has likewise been observed for nitrogen-containing building blocks. For instance, oligopyridines yield different hydrogen bonded networks, where all structures are based on C−H···N hydrogen bonds.[159] Albeit probably not fully understood, at the liquid-solid interface structural control of monolayers can be accomplished by the choice of solvent, concentration, and temperature.[160, 68]

A tentative model of the less complex trigonal densely packed polymorph with one molecule per unit cell is shown in Fig. 5.4(f). Intermolecular hydrogen bonds in this structure are exclusively based on the head-to-tail arrangement. Since in this hydrogen bond motif both molecules adopt the same azimuthal orientation, the trigonal densely packed structure contains only one molecule per unit cell. The mirror symmetry of the head-to-tail arrangement also results in the more symmetric *p3m1* plane symmetry group. The lattice parameter of 0.9 nm of the trigonal densely packed polymorph is equal to the center-to-center distance in the melem head-to-tail arrangement. It is noteworthy that this densely packed polymorph can also be

enqueued in the series of porous polymorphs as limiting case for $N \to \infty$. Since the unit cell becomes infinitely large, the side-by-side bonding motif at the boundaries and at the shorter diagonal of the unit cell of the porous polymorphs, does not occur anymore.

The second densely packed polymorph features a row like structure with two molecules per unit cell. Each row comprises melem molecules with alternating azimuthal orientations, where the baselines of the melem footprints are aligned parallel to the row direction. The monolayer structure consists of a dense packing of parallel rows, and melem molecules adjoin with parallel baselines of their triangular footprints. The tentative model of the structure including the unit cell and the hydrogen bond pattern is depicted in Fig. 5.7. The two melem molecules in the unit cell are rotated by 180° with respect to each other. Within the rows melem molecules are interconnected by the alternative side-by-side arrangement as illustrated in Fig. 5.5(c), where the amino groups do not interact with the heterocyclic nitrogen atoms next to the involved amino groups, but with the heterocyclic nitrogen atom next to the other amino group. The hydrogen bond pattern between the rows bears similarities with the regular side-by-side arrangement, however, the side of the melem molecules facing the boundaries between rows forms two side-by-side bonds with two melem molecules. This arrangement results in a geometrically slightly different, but still comparable, side-by-side motif.

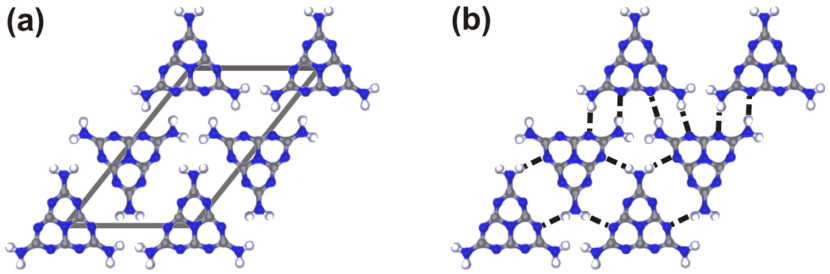

Figure 5.7: Tentative model of (a) the unit cell and (b) the hydrogen bond pattern of the densely packed row polymorph with two melem molecules per unit cell.

For melamine a rather similar densely packed polymorph was reported which is based on two different side-by-side arrangements.[142] Also a densely packed melem structure was previously observed by electrochemical STM on Au(111).[161] Although the reported structure also features two molecules per unit cell, the melem–melem arrangements are based on the two different binding motifs prevalent in the porous polymorphs of the present study, *i.e.* head-to-tail and side-by-side (*cf.* Fig. 5.5(a) and (b)). In summary the intermolecular hydrogen bonds in the more complex densely packed polymorph are still based on $N_{amino}{-}H{\cdots}N_{heptazine}$, yet the underlying melem–melem arrangements are different from those in the systematic series of polymorphs.

5.4 Summary and Outlook

In summary, we have shown that two-dimensional self-assembly of melem on Ag(111) is very versatile and yields a great structural variety of hydrogen bonded networks. In all structures melem molecules adsorb planar and are interconnected by N_{amino}−H···$N_{heptazine}$ hydrogen bonds. All structures, except for one densely packed polymorph, can be described as elements of a systematic series of structures. Thereby, the number N of melem molecules along the connection between adjacent pores increases in increments of one. Only two different intermolecular melem–melem hydrogen bond arrangements, denoted as side-by-side and head-to-tail, account for the observed versatility of porous melem structures. The higher porous polymorphs with $N =]1, \infty[$ feature both intermolecular bonding schemes, whereas both the trigonal densely packed polymorph ($N \to \infty$) and the simplest porous polymorph ($N = 1$) rely exclusively on the head-to-tail and side-by-side arrangement, respectively. Although the more complex densely packed polymorph is comprised of slightly different melem–melem arrangements, it is still stabilized by N_{amino}−H···$N_{heptazine}$ hydrogen bonds.

Polymorphism is abundant in surface-confined two-dimensional self-assembly and its origins are poorly understood. Commonly, the energetic equivalence of various structures on the scale of thermal energy contributes to the emergence of different polymorphs. In this respect increased structural versatility is expected for compounds with larger organic backbone like melem as opposed to melamine. The reason is that for larger compounds the molecule–substrate interaction increases, while the contribution of intermolecular hydrogen bonds to the overall binding energy remains similar. Thus, the delicate balance between molecule–molecule and molecule–substrate interactions changes, and optimization of hydrogen bonds is not the only and probably not the decisive criterion for structure selection anymore. In addition, larger molecules allow for various other interactions, as seen for melem in the possibility of an alternative side-by-side and head-to-tail arrangement. Both contributions promote polymorphism.

For monolayer self-assembly at the liquid-solid interface, the influence of concentration and solvent is understood at a level which allows deliberate preparation of a distinct polymorph. However, for monolayers at the liquid-solid interface the relation between preparation parameters and molecular structure is less well studied. In this regard nucleation and growth studies are very desirable. For the presented series of porous melem monolayers, being able to target a specific monolayer would be highly beneficial. All porous polymorphs feature similar pore size, but variable interpore spacing. Using these porous polymorphs as growth template for metal nanoparticles would thus allow tuning the spacing between nanoparticles with sub-nanometer precision in order to study distance-dependent effects. On the other hand, self-assembled melem monolayers might be promising precursor structures for the surface mediated polymerization into carbonitride polymers.[151]

Chapter 6

On-Surface Polymerization of 2D Nanostructures

6.1 On-Surface Coupling of 1,4-Diethynylbenzene on Cu(111)

J. Eichhorn, W. M. Heckl, and M. Lackinger. On-surface polymerization of 1,4-diethynylbenzene on Cu(111). *Chem. Commun.* 49 (2013), 2900-2902.

The polymerization of 1,4-diethynylbenzene was studied on a Cu(111) surface using scanning tunneling microscopy under UHV conditions. Thermal activation yielded disordered covalent networks, where distinct basic structural motifs indicated different coupling reactions.

6.1.1 Introduction

Covalent organic nanostructures are a topic of growing research interest. Organic materials possess remarkable properties facilitating novel and versatile applications. Covalent organic frameworks (COFs) such as porous bulk crystals are particularly promising for many applications in gas storage, catalysis, and as molecular sieves.[125] Implementation of boronate chemistry in a solvothermal synthesis yielded versatile COF structures,[17] including first demonstrations of the application potential in organic electronics.[162] In an attempt to synthesize low dimensional covalent nanostructures, boronic acid condensation was also successfully applied in a surface chemical approach.[130, 163, 164] However, boronate chemistry suffers from two limitations, *i.e.* limited stability of the covalent networks in humid atmospheres and poor electronic conjugation.[164, 97] The polymerization of ethynyl functionalized monomers is a promising alternative to overcome these limitations, because the resulting polymers exclusively feature stable C−C bonds and the high degree

of unsaturation facilitates π-electron delocalization. A further advantage over the meanwhile in 2D polymer synthesis established Ullmann reaction [101, 84, 165] is that the surface will not be covered by strongly adsorbing reaction byproducts.
Polymerization of aromatic ethynyl functionalized molecules is already exploited for the synthesis of conjugated microporous bulk polymers that are not crystalline in contrast to boronic acid derived COFs.[116] Interestingly, ditopic monomers such as 1,4-diethynylbenzene (DEB) can polymerize into highly porous three-dimensionally cross-linked poly(phenylene butadiynylene) (PPB) networks. Yet, polymerization of DEB in a confined geometry such as the Cu-functionalized channels of mesoporous silica and alumina materials exclusively yields one-dimensional, conjugated PPB wires.[166] In order to explore the versatile chemistry of monomers with terminal ethynyl groups, it is particularly interesting to study the polymerization of DEB on surfaces, *i.e.* in a two-dimensionally confined geometry. Cu(111) is chosen as a catalytically active and densely packed surface, where the influence of surface structure and anisotropy is minimized.

6.1.2 Experimental Details

All experiments were conducted with a scanning tunneling microscope (Omicron VT-STM) at room temperature under UHV conditions with a base pressure below 2×10^{-10} mbar. All STM images were recorded with a SPM 100 control electronics from RHK using the XPM Pro 2.0.1.3 software. Lattice parameters and intermolecular distances were derived from STM images with an accuracy of 5% after calibration with atomically resolved topographs of highly oriented pyrolytic graphite(001). Single crystal Cu(111) surfaces were prepared by cycles of Ar^+ ion-sputtering at 1 keV and annealing at 550 °C. The cleanliness of the substrate was verified by STM prior to molecular deposition.
The monomer 1,4-diethynylbenzene (DEB, Fig. 6.1) ($C_{10}H_6$, CAS 935-14-8, 95.5% purity) with a molecular weight of 126.15 amu was obtained from Sigma Aldrich Germany. DEB was deposited through a precision leak valve with a metal capillary connected to the outlet to guide the molecules to the sample. During deposition the Cu(111) substrate was either held at room temperature or heated to 300 °C. For RT deposited DEB, the polymerization was thermally activated by annealing at temperatures between 175 °C and 350 °C.

6.1.3 Room-Temperature Self-Assembly

Room temperature deposition of DEB onto Cu(111) results in well-ordered structures with one molecule per unit cell and lattice parameters of $a = (0.73 \pm 0.10)$ nm, $b = (0.80 \pm 0.10)$ nm, and $\gamma = (98.9 \pm 4.1)$ °. The STM images depicted in Fig. 6.1(a) and (b) clearly confirm that all molecules have similar azimuthal orientation. We propose that this structure is comprised of unreacted, intact DEB molecules;

a tentative model is given in Fig. 6.1(d). The regularly arranged bright spots correspond to the phenyl rings of DEB and their relatively loose packing provides enough space for the ethynyl groups. The self-assembled monolayer is additionally stabilized by weak intermolecular hydrogen bonds as indicated in Fig. 6.1(d). Parallel aligned ethynyl groups interact through two-fold cyclic C≡C−H···C≡C hydrogen bonds (grey), where the acidic hydrogen acts as a donor and the aromatic triple bond as an acceptor for hydrogen bonds.[69] Additional stabilization might arise from intermolecular interactions between ethynyl groups and adjacent phenyl rings (black).[167] Recent *ab initio* calculations suggested an attractive electrostatic contribution from the entire aromatic ring, introduced as proton acceptor ring interactions, whereas the direct dipole-dipole interaction between C−H and the proton acceptor is repulsive.[66] The experimental bond length of the cyclic hydrogen bonds of (0.3 ± 0.1) nm is consistent with literature values,[69, 167] whereas the experimental ethynyl-phenyl bond length of (0.4 ± 0.1) nm is slightly longer than the reported value of 0.3 nm. The self-assembled DEB structure on Cu(111) differs clearly from the layered bulk crystal structure where DEB forms zigzag chains within the layers.[168, 169] The bulk structure is likewise stabilized by C≡C−H···C≡C hydrogen bonds, yet with a perpendicular arrangement of the ethynyl groups to the C≡C triple bonds. A comparable surface arrangement would be conceivable, but is apparently impaired by the strong interaction of DEB with Cu(111).

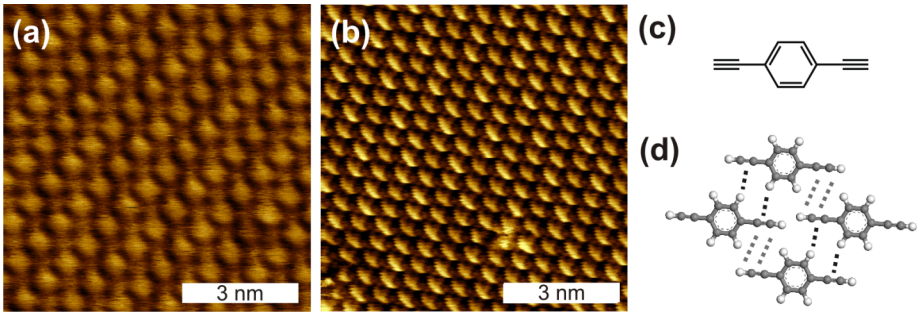

Figure 6.1: (a)+(b) STM image ((a) +18 mV, 3.2 pA, (b) +12 mV, 0.90 pA) of a self-assembled DEB monolayer deposited at RT onto Cu(111). (c) Chemical structure of DEB. (d) Tentative model showing the DEB arrangement and interactions. The structure is additionally stabilized by weak intermolecular hydrogen bonds as indicated by dashed lines.

6.1.4 On-Surface Polymerization

Upon room temperature deposition of DEB onto Cu(111) no indications of chemical reactions are observed. Yet, drastic structural changes occur after annealing the sample to 300 °C for 60 min. STM images obtained after cooling down to RT are depicted in Fig. 6.2. The disordered structures appear with uniform height and the contrast along the network does not exhibit any apparent depressions. Frequently observed structural motifs include threefold stars, dumbbells, and oblique crosses. Given the fact that the disordered structures are still observed after

thermal treatment up to 450 °C, one can conclude covalent interlinking of DEB. The adsorption energy of a relatively small molecule such as DEB on Cu(111) is too low for stable adsorption at higher temperatures. Thermal desorption of ethynylbenzene from Cu(111) for comparison is already observed at ∼140 °C.[170]

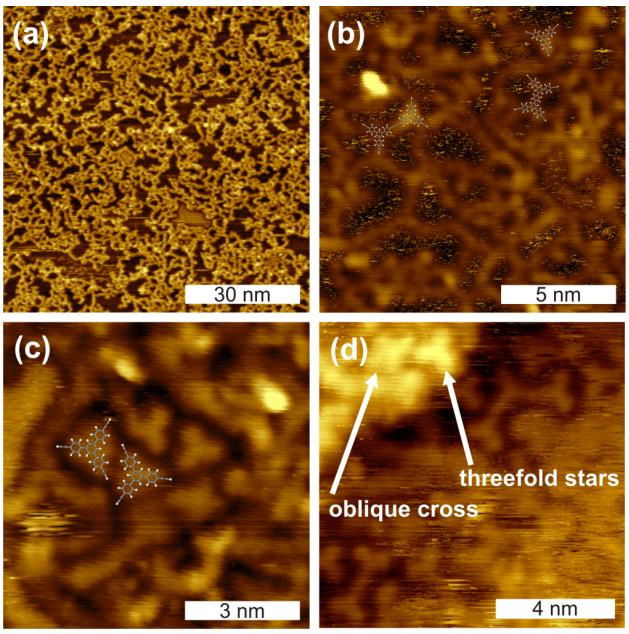

Figure 6.2: High-resolution STM images of annealed DEB monolayers on Cu(111). Thermally activated reactions yield covalent aggregates and networks. Overview (a) and close-up (b)-(d) STM images with overlaid DFT optimized geometries of candidate structures ((a) -0.70 V, 2.3 pA, (b) -0.60 V, 4.3 pA, (c) +1.1 V, 1.7 pA), (d) +0.40 V, 1.7 pA)

Hence, only aggregation into more extended covalently interconnected networks can stabilize the adsorbates at increased temperatures. Annealing to 450 °C for 60 min slightly reduces the surface coverage, but similar structures are still observed after cooling down. Disintegration upon annealing and reformation of the structures during cooling down can also be excluded, because separation into monomers inevitably leads to desorption. Moreover, complexation through coordination of deprotonated ethynyl groups by copper adatoms as observed for Ullmann coupling seems also to be conceivable.[84, 149] These radical-adatom complexes, however, are metastable, and even relatively mild heating at 230 °C is sufficient to expel the copper atoms,[171] whereby radical recombination yields covalent C−C bonds. Furthermore, radical-adatom complexes are notably larger than the corresponding covalent structures and their size does not match the STM data (*cf.* subsection 6.1.5 and 4.2.2, Fig. 4.5). Finally, the uniform STM contrast mentioned here is not compatible with the known appearance of these complexes, with either a clear protrusion or an apparent depression at the adatom position.[149] In order to reveal the nature of the surface reactions, first the reoccurring structural elements have to be resolved. In the literature different self-reactions are reported for ethynyls such as homo-coupling [116] and trimerization.[119, 172] Trimerization forms benzene whereas

homo-coupling (Glaser coupling) leads to butadiyne bridges (–C≡C−C≡C–) with enyenes as reaction side products in trace amounts.[118, 117] The polymerization of head-to-tail coupled enyenes can result in the formation of cross-linked polymers.[116]

While the solution chemistry of ethynyl functionalized molecules has already been studied, their cross-linking on surfaces remains largely unexplored. By analogy, surface reactions of acetylene may offer first insights. For instance, a combined temperature programmed reaction (TPR) and X-ray photoelectron spectroscopy (XPS) study reveals conversion of acetylene into benzene *via* trimerization on copper surfaces. The reaction is highly selective on Cu(100) and Cu(110), but yields butadiene and cyclooctatetraene as byproducts on Cu(111).[120] Ethynyl homo-coupling is observed in surface chemical studies of Sonogashira cross-coupling between co-deposited ethynylbenzene and iodobenzene on Au(111).[173] First covalent 2D networks are obtained through homo-coupling of triethynyls on Ag(111).[121] Evidently, different coupling reactions are required to explain the structurally versatile polymerization products of DEB on Cu(111). In the following, the distinct basic structural motifs are identified by scaled overlays of the STM data with density functional theory (DFT) optimized geometries of conceivable candidate structures. Chemical structures of all considered aggregates are summarized in Fig. 6.3 (see subsection 6.1.5 for DFT results). Obviously, the occurrence of threefold symmetric stars requires trimerization reactions, where three DEB molecules react into 1,3,5-tris(4'-ethynylphenyl)benzene (TEPB). The central benzene ring results from trimerization of three ethynyl groups, where no reaction byproduct is released. As shown in Fig. 6.2(b) and (c) the structural overlay perfectly matches the STM data.

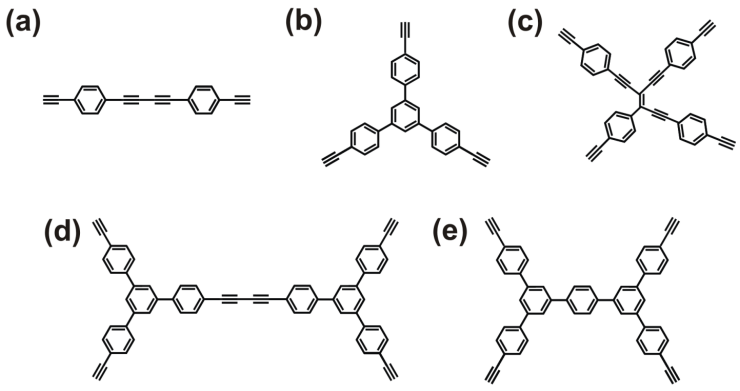

Figure 6.3: Structural models of experimentally observed reaction products of DEB: (a) homo-coupling, (b) trimerization, (c) cross-coupling, (d) combined trimerization and homo-coupling, (e) sequential double trimerization.

Detailed analysis of the STM data reveal two types of dumbbells that differ in the lengths of their axes, with the shorter one measuring (1.0 ± 0.1) nm and the longer one (1.9 ± 0.1) nm. Both dumbbell structures can be matched with DFT models as shown in Fig. 6.2(b). The longer dumbbell can be explained by homo-coupling of

two preformed TEPB molecules (Fig. 6.3(d)). Accordingly, its axis consists of two biphenyls interlinked by a structurally rigid butadiyne backbone. The homo-coupling releases H_2, in contrast to the trimerization. Similar homo-coupling reactions were recently observed for 1,3,5-triethynylbenzene and TEPB on Ag(111).[121] The shorter dumbbell can be matched with a *para*-terphenyl backbone (Fig. 6.3(e)). Such an aggregate can emerge from preformed TEPB through secondary trimerization of one of the free terminal ethynyl groups with two unreacted DEB monomers. Oblique crosses are the most complicated and least symmetric observed structures (Fig. 6.2(c)+(d) and Fig. 6.3(c)). They are formed by coupling of four DEB molecules and appear as an asymmetrical fourfold junction. In Fig. 6.2(d), a threefold star adjacent to an oblique cross can be recognized. In the threefold symmetric star all lobes have similar length, whereas the oblique cross features three similar lobes and one shorter lobe, in good agreement with the DFT simulation shown in Fig. 6.3(c). This more complex cross-coupling also includes formation of C=C double bonds. Based on NMR results, similar reactions are reported for DEB bulk polymerization,[116] but are here resolved in real space.
In an attempt to control DEB polymerization, different parameters and methods for the thermal activation are studied. The onset of polymerization is roughly determined at 175 °C. However, no structural changes are observed for different annealing temperatures up to 300 °C and different annealing times ranging from 20 to 105 min. Furthermore, the effect of deposition onto a pre-heated Cu(111) surface at 300 °C is investigated, but does not exhibit any apparent differences from post-deposition annealing.

6.1.5 DFT Calculations of the Reaction Products

Covalent Aggregates

Intramolecular distances derived from DFT calculations of threefold star, oblique cross, small and large dumbbell are summarized in Fig. 6.4. Optimized geometries were used for a precise structural comparison with the STM data. DFT calculations were conducted for isolated molecules using the Gaussian03 package with a B3LYP functional and a 6-31G* basis set applying standard convergence criteria.[174] To mimic the surface influence, the structures were constrained to a planar conformation by fixing the z-coordinates of all atoms to zero.

Organometallic Complexes

Additional DFT calculations were conducted for a direct size-comparison of the large covalent dumbbell with a copper coordinated 1,3,5-tris(4'-ethynylphenyl)benzene dimer, the closest matching organometallic complex. The latter is a hypothetical aggregate that might form on the surface between deprotonated ethynyl groups and copper adatoms. As before, DFT calculations were conducted for isolated

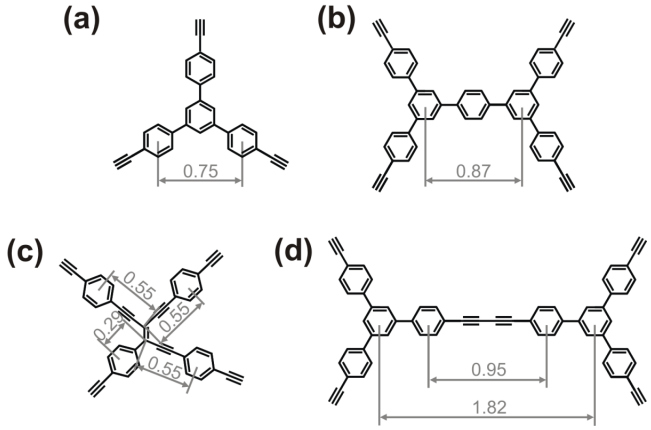

Figure 6.4: Intramolecular distances from DFT geometry optimized structures of experimentally observed reaction products of DEB (a) trimerization (b) sequential double trimerization (c) cross-coupling (d) combined trimerization and homo-coupling. All distances are given in nm. Based on these calculations, the size differences between (b) and (d) should be clearly distinguishable in STM measurements.

structures using the Gaussian03 package with a B3LYP functional and a 6-31G* basis for hydrogen and carbon, whereas a LanL2DZ basis set is used for copper applying standard convergence criteria.[174] Results are shown in Fig. 6.5. Straight organometallic bonds are 0.24 nm longer than the direct covalent carbon-carbon bond. This bond length difference is large enough to exclude the formation of organometallic structures based on distance measurements in STM data.

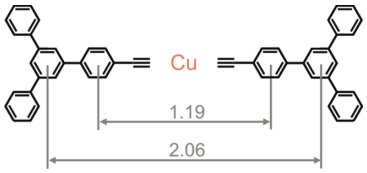

Figure 6.5: Intramolecular distances from DFT geometry optimized structure of copper coordinated (peripheral ethynyl groups discarded) DEB. All distances are given in nm.

6.1.6 Summary

In summary, on-surface polymerization of ethynyl functionalized DEB monomers was studied on Cu(111). RT deposition resulted in well-ordered self-assembled structures of intact molecules. After thermal activation, disordered covalent networks and aggregates were observed by means of STM. Structural analysis of the reoccurring basic motifs revealed several different underlying reaction schemes: trimerization, homo-, and cross-coupling. Emergence of more complex structures such as dumbbells can only be explained by a sequential combination of these basic reactions. Thus the surface chemistry of DEB is very versatile and different possible reaction pathways without a clear preference for a specific coupling reaction inevitably result in

disordered covalent networks, as similarly encountered in the synthesis of highly porous PPB-type bulk polymers.[116] On Cu(111) the polymerization cannot simply be controlled by process parameters such as annealing temperature or time. In this respect it would be highly interesting to explore the potential of different surface materials and crystallographic orientations with more pronounced anisotropy to selectively catalyze a specific coupling reaction and suppress side reactions as a route to highly ordered, covalent, and conjugated organic nanostructures.

6.2 On-Surface Ullmann Coupling

On-surface Ullmann coupling is a versatile and appropriate approach for the bottom-up fabrication of covalent organic nanostructures. In two-dimensional networks, however, the kinetically controlled and irreversible coupling leads to high defect densities and a lack of long-range order. To derive general guidelines for optimizing reaction parameters, the structural quality of 2D porous covalent networks was evaluated for different preparation protocols. For this purpose, polymerization of an iodine and bromine functionalized monomer was studied on Au(111) by scanning tunneling microscopy and X-ray photoelectron spectroscopy under UHV conditions. By taking advantage of the vastly different temperature thresholds for C−Br and C−I cleavage two different polymerization routes were compared - hierarchical and direct polymerization. The structural quality of the covalent networks was evaluated for different reaction parameters, such as surface temperatures, heating rates, and deposition rates by statistical analysis of STM data. Experimental results are compared to Monte Carlo simulations.

6.2.1 Introduction

Low-dimensional covalent organic nanostructures are promising novel functional materials for nanotechnological applications,[175, 176] as they combine unprecedented chemical and mechanical stability with the vast tunability of organic materials. Their adjustable electronic band gap renders these materials highly interesting for applications in (opto)electronic devices.[17, 18, 15] On-surface polymerization has become an established route for the tailored fabrication of covalent nanostructures. In recent years, various coupling reactions were applied for the fabrication of 1D and 2D covalent nanostructures including condensation reactions,[130, 177] homo-couplings

of terminal alkynes (Glaser-Hay-coupling),[121, 178, 135] and Ullmann coupling [106, 101, 179]. In the first step of the Ullmann coupling brominated [83, 20, 112] or iodinated [106, 56, 171] monomers are deposited onto metal surfaces, typically under UHV conditions, even though this was also demonstrated under ambient conditions.[180, 181] The weakly bound halogens are split off either directly upon adsorption or after additional thermal activation, and the resulting surface-stabilized radicals form kinetically inert C−C crosslinks. Two-fold halogenated monomers yield virtually defect-free 1D structures, such as poly(3,4-ethylenedioxythiophene) chains,[182] poly(para-phenylene),[19] and graphene nano-ribbons [20]. Similarly, 2D networks can be obtained with multiply halogenated monomers, yet with significantly lower structural quality, *i.e.* high defect densities and rather small domain sizes.[84, 97] The kinetic irreversibility of the newly formed C−C bonds impairs error correction.

The Ullmann coupling relies on the catalytic properties of the metal surface to activate the polymerization by splitting off the halogens. Accordingly, the surface plays an active chemical role and different influences arise in dependence on the metal. At room temperature, C−I bonds are spontaneously cleaved on Cu, Ag, and Au.[135, 56] Bromine, instead, is fully split off on copper,[83, 84] only partially on silver,[85, 108] but not all on gold, where additional thermal activation becomes necessary.[56] DFT simulations suggest that the energy barriers are around 0.3 eV smaller for deiodination than for debromination on Au(111), Ag(111), and Cu(111).[111] Subsequent to carbon–halogen cleavage organometallic networks based on carbon–metal bonds were observed; 1D organometallic chains are ordered,[19, 57] whereas 2D networks on copper remain disordered,[83, 84, 85] but can be partially ordered on silver.[108, 86] Even reorganization and equilibration of silver-based organometallic networks was demonstrated on Ag(111), indicating the reversibility of C−Ag bonds (*cf.* chapter 7, Ref. [108]). On gold organometallic networks are less common, but were occasionally observed.[87] A further important substrate influence arises from the surface mobility of the surface-stabilized radicals (SSRs), as exemplified in a combined STM and MC study of cyclohexa-*m*-phenylene (CHP), where improved networks were observed for an increasing ratio of diffusion to coupling.[56]

While the surface dependence of the Ullmann coupling has been thoroughly studied, the influence of controllable reaction parameters on the quality of 2D covalent networks remains largely unexplored. The present work tackles this open question by studying the polymerization of 1,3-bis(*p*-bromophenyl)-5-(*p*-iodophenyl)benzene (BIB, *cf.* Fig. 6.6(a)) on Au(111). The asymmetrical substitution with bromine and iodine as well as the particular choice of Au(111) facilitates comparative studies of direct versus hierarchical polymerization. Direct polymerization is realized by deposition onto a preheated surface, whereby both iodine and bromine are split off in the same polymerization step. Hierarchical polymerization is achieved by room temperature deposition, whereby iodine is selectively split off, whereas bromine remains stably bound. Only further thermal annealing activates C−Br cleavage and thereby the full polymerization. This principle was already exploited by Grill and Hecht *et al.* using *trans*-Br_2I_2 tetraphenyl-porphyrin.[107]

In the present work, influences of various reaction parameters on the morphology and quality of covalent networks were studied: for direct polymerization the surface temperature during deposition and the deposition rate were varied, while for hierarchical polymerization the heating rate and final surface temperature were investigated. The network quality was evaluated and quantified by statistical analysis of STM data. For enhanced insights the experiments were accompanied by XPS measurements and MC simulations.

6.2.2 Experimental Details

All experiments were carried out with a home-built scanning tunneling microscope at room temperature and under UHV conditions with a base pressure of 2×10^{-10} mbar. All STM images were acquired with a SPM 100 control electronics from RHK using the XPM Pro 2.0.1.5 software. The STM was calibrated with atomically resolved topographs of highly oriented pyrolytic graphite(0001). Distances were derived from STM topographs with an accuracy of $\sim 5\%$. Tunneling parameters of all STM images are summarized in Tab. 6.1.

Table 6.1: Tunneling parameters of the STM images in section 6.2.

Figure		Tunneling Parameter	
		Voltage (V)	Current (pA)
6.8	a)	+1.0	9.0
	a) inset	+1.5	8.7
	b)	+3.0	4.6
	b) inset	-0.20	3.1
	c)	+4.1	4.7
	d)	+1.8	11
6.10	a)	+3.0	4.6
	a) inset	-0.20	3.1
	b)	+0.50	7.2
	b) inset	-2.0	17
	c)	+2.0	4.8
	d)	+3.0	5.5
6.14	a)	+1.7	4.8
	b)	-1.7	4.8
	c)	+2.9	4.3
	d)	+3.1	5.9
6.16	a)	+2.9	4.3
	b)	+1.8	2.6
	b) inset	+0.40	8.2
	c)	+1.4	9.6
	c) inset	+1.5	9.9
	d)	+1.3	12

Au(111) single crystal surfaces were prepared by cycles of Ar^+ ion-sputtering and subsequent annealing at 500 °C. The cleanliness of the substrate was verified by STM imaging the well-known herringbone reconstruction prior to deposition. The monomer BIB was deposited by sublimation from a home-built Knudsen cell with crucible temperatures of 126 °C to 168 °C, yielding deposition rates of 0.3×10^{-3} ...0.2 monolayer min^{-1}. To precisely control the deposition rates and to verify their long term stability, a Knudsen cell with integrated QCMB was used.[35] During deposition, the surface was either held at room temperature or at elevated temperatures of 185 °C, 250 °C, and 375 °C, respectively. After RT deposition, the polymerization was activated by subsequent thermal annealing with different rates and final temperatures. All samples were characterized *in situ* by means of a home-built STM operating at room temperature.
Additionally, X-ray photoelectron spectroscopy (XPS) was conducted to investigate debromination and deiodination in detail. XPS measurements were carried out in a Prevac UHV system at the HE-SGM beamline at Helmholtz-Zentrum Berlin. The preparation chamber of the UHV system was equipped with facilities for sample sputtering and heating. For sample preparation similar parameters were used as in the corresponding STM experiments. Br 3d, I 3d and C 1s XP spectra were acquired with a Scienta R3000 electron analyzer at normal electron emission using an excitation energy of 450 eV and a pass energy of 50 eV. The binding energy of Au $4f_{7/2}$ at 84.0 eV was used as an internal energy reference. A linear background was subtracted from all spectra.

6.2.3 Hierarchical Polymerization of 1,3-bis(*p*-bromophenyl)-5-(*p*-iodophenyl)benzene

RT Deposition

Samples were prepared by deposition of BIB onto Au(111) at room temperature and subsequent thermal annealing. Prior to annealing STM revealed self-assembly of dumbbell shaped basic units (Fig. 6.6). The herringbone reconstruction of Au(111) is still discernible (Fig. 6.6(c)), indicating weak adsorbate–substrate interaction. The unit cell measures $a = (1.60 \pm 0.10)$ nm, $b = (1.64 \pm 0.10)$ nm, and $\gamma = (94.5 \pm 4.0)°$ and contains one dumbbell with additional dots at its corners.
The dumbbells appear with uniform height, *i.e.* without internal STM contrast. For room temperature deposition we anticipate the surface-assisted formation of BIB mono-radicals through C−I cleavage followed by direct covalent crosslinking to dimers, *i.e.* 3,3‴,5,5‴-tetra(*p*-bromophenyl)-1,1’:4’,1”:4”,1‴-quaterphenyl (TBQ, *cf.* Fig. 6.6(b)). Hence, the dots in the STM images can be assigned to surface-bound iodine. The coupling of two BIB to one TBQ releases two iodine atoms, whereas the self-assembled structure features only one iodine per TBQ. Yet, excess iodine was observed on terraces. In perfect agreement with STM, DFT gas phase geometry optimization of the dimer results in a length of 1.3 nm for the quaterphenyl backbone

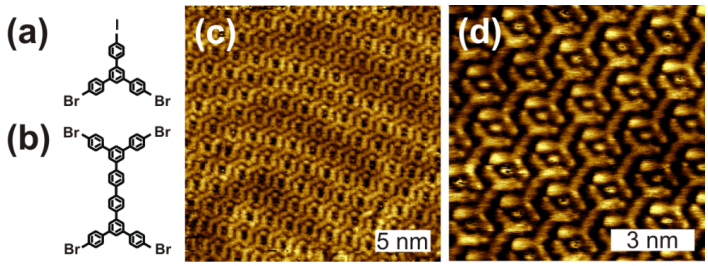

Figure 6.6: Chemical structures of BIB (a) and TBQ (b). Overview (-0.20 V, 35 pA) (c) and close-up STM images (+0.40 V, 3.5 pA) (d) of self-assembled TBQ structures acquired after room temperature deposition of BIB onto Au(111).

(*cf.* subsection 6.2.7). The formation of metastable organometallic complexes, as typically observed on copper and silver,[83, 85, 86] would elongate the backbone to 1.6 nm in contradiction to the experiment. The STM data clearly show that the dimers are formed by direct covalent coupling of the molecular building blocks at their previously iodinated sites without debromination. The STM results are also confirmed by XPS measurements, which are presented below.
Interestingly, self-assembled dimers were similarly reported for fully brominated 1,3,5-tris(*p*-bromophenyl)benzene (TBB) on Au(111) after heating to 110 °C.[112] Yet, in this case the coexistence of dimers (TBQ), disordered structures, and unreacted monomers indicates an incomplete reaction. Furthermore, drop-casting of TBB under ambient conditions onto preheated Au(111) at 200 °C results in self-assembled TBQ monolayers with similar lattice parameters.[181]

Subsequent On-Surface Polymerization

The full polymerization of *in situ* synthesized TBQ was activated by subsequent thermal annealing. The required temperature for C−Br bond cleavage on Au(111) is around 175 °C (Fig. 6.7). For lower annealing temperatures, only non-covalent self-assembly of TBQ was observed (Fig. 6.6). After annealing to 185 °C, however, no unreacted TBQ was observed anymore. Thus, we propose 175 °C corresponds to the minimum temperature required for sizable C−Br bond cleavage of BIB on Au(111). The covalent nature of the networks is unambiguously verified by an experimental center-to-center distance of interconnected monomers of 1.3 nm.

For hierarchical polymerization the influences of both surface temperature and heating rate were studied by (1) heating samples with comparable rates of 6.3 - 8.9 °C min^{-1} to 185 °C, 250 °C, and 375 °C (Fig. 6.8), and by (2) heating with variable rates of <0.1, 1.4, and 8.9 °C min^{-1} to a constant final temperature of 250 °C (Fig. 6.10). The initial coverages for all experiments were comparable and the samples were held at the final temperature for 15 or 70 min. Irrespective of the exact thermal treatment, all covalent networks were highly branched and composed of relatively small domains connected by filamentous structures of one-pore wide strings

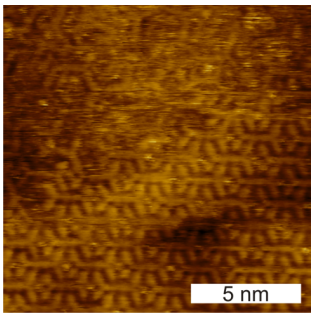

Figure 6.7: STM image acquired after RT deposition of BIB onto Au(111) and subsequent annealing to 175 °C (+0.60 V, 7.5 pA). The coexistence of the initially self-assembled TBQ structure and first covalently interlinked structures indicates the onset of C−Br bond cleavage.

or molecular chains (Fig. 6.8 and 6.10). Besides the ideal hexagonal pores, irregular pores - tetragonal, pentagonal, heptagonal, and octagonal - were frequently observed. To quantify the structural quality of the networks, STM data were statistically analyzed by pore counting. Thereby the pore geometry and the number of adjacent pores were taken into account. Open pores were only considered when they were more than halfway closed. For each parameter set the analysis encompassed at least 100 pores, typically 200 pores. Uncertainty values are given as the square root of counts. Macroscopically different sample areas were compared to reduce the influence of sample inhomogeneities.

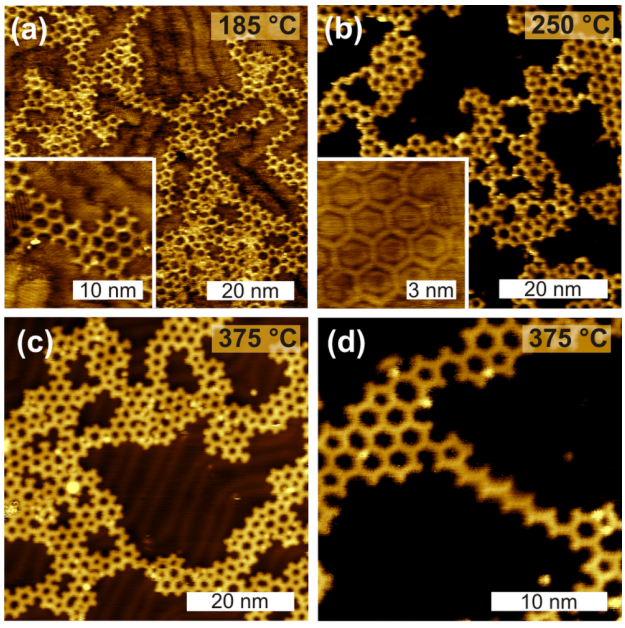

Figure 6.8: STM images of covalent networks prepared by RT deposition of BIB and subsequent thermal annealing (*cf.* subsection 6.2.2 for tunneling parameters). Due to preceding dimerization at RT, the actual monomer for the polymerization is the dumbbell shaped TBQ. Thermal annealing was performed at different final temperatures of 185 °C (a), 250 °C (b), and 375 °C (c)+(d) as also indicated in the upper right corners. All samples were annealed with comparable heating rates of 6.3 °C min^{-1}(a) or 8.9 °C min^{-1} (b)-(d).

The corresponding pore geometry distributions of tetragonal to octagonal pores obtained for different final temperatures are depicted in Fig. 6.9(a). The counts were normalized to the total number of closed pores ΣN_i, with N_i corresponding to the counts of i-gonal pores. The highest probability for hexagonal pores was found for 185 °C. All covalent networks feature significant amounts of pentagonal pores as well as lower amounts of heptagonal pores. Tetragonal and octagonal pores are less frequently observed and were fully absent for 185 °C. Especially at lower polymerization temperatures the network quality is significantly impaired by open, *i.e.* incomplete pores, (*cf.* inset Fig. 6.9(b)). This is considered in the histogram in Fig. 6.9(b) by renormalization of N_i to the sum of closed and open pores ($\Sigma N_i + N_0$). Direct comparison of both histograms indicates significant changes for polymerization at 185 °C, whereas the 250 °C and 375 °C distributions remain largely unaffected. In conclusion, the probability for irregular pores increases slightly with higher final temperatures, whereas polymerization at 185 °C results in a substantial amount of open pores.

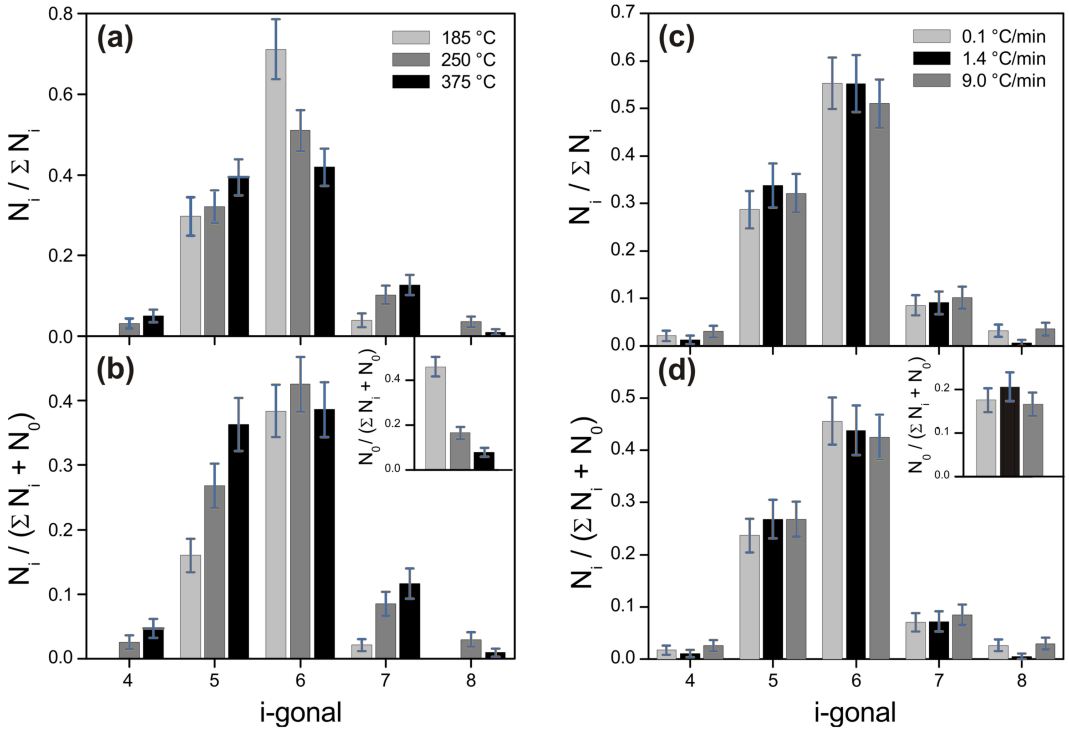

Figure 6.9: Pore geometry distributions of covalent networks prepared by hierarchical polymerization *via* RT deposition and subsequent annealing. (a)+(b) In all experiments the substrate was heated to different final temperatures (185 °C, 250 °C, and 375 °C) with similar heating rates of 6.3 °C min^{-1} or 8.9 °C min^{-1}. (c)+(d) The samples were prepared with a constant substrate temperature of 250 °C, whereas different heating rates of 0.1 °C min^{-1}, 1.4 °C min^{-1}, and 8.9 °C min^{-1} were applied. N_i and N_0 correspond to the number of i-gonal and open pores, respectively. Accordingly, the probabilities of i-gonal pores in (a) are referred to the total number of closed pores (ΣN_i), whereas in (b) N_i is normalized to the sum of closed and open pores ($\Sigma N_i + N_0$). The inset in (b) shows the relative amounts of open pores N_0 for the different final temperatures.

Besides the final substrate temperature, also the influence of the heating rate on the network quality was investigated. STM images of the resulting structures are summarized in Fig. 6.10. The statistical analysis for all heating rates yields almost identical pore geometry distributions (*cf.* Fig. 6.9), suggesting no decisive influence on the network quality.

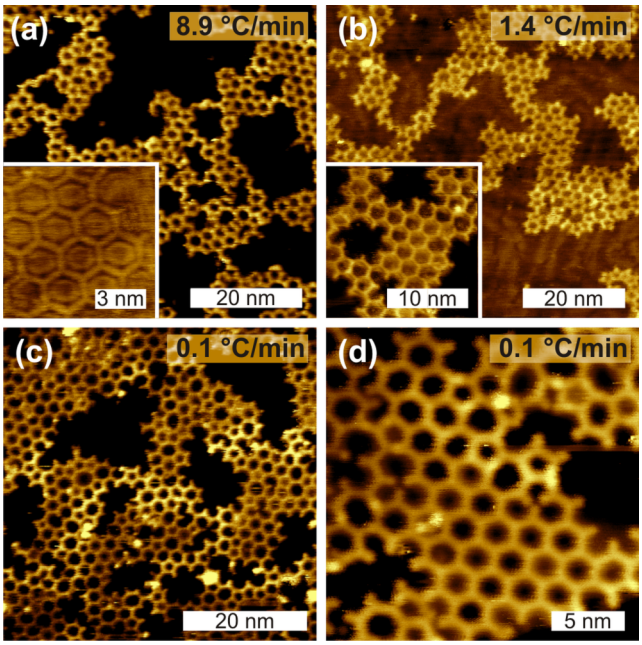

Figure 6.10: STM images of covalent networks prepared by RT deposition of BIB and subsequent thermal annealing (*cf.* subsection 6.2.2 for tunneling parameters). All samples were annealed at 250 °C whereas different heating rates of 8.9 °C min^{-1} (a), 1.4 °C min^{-1}(b) and 0.1 °C min^{-1} (c)+(d) were applied. The insets depict close-up STM images of the most regular sample areas.

Pore geometry distributions do not cover important structural aspects as the degree of compactness and the domain size. Respective structural information is contained in the pore coordination number, *i.e.* the number of next nearest neighbors of a closed pore, whereby only closed pores were considered. Hence, the average pore coordination number (APCN) is introduced as a further statistical indicator of the network quality. In a perfect hexagonal network the APCN is 6, whereas low values indicate the formation of branched networks. APCNs were evaluated for the different reaction parameters, the underlying PCN distributions are summarized in Fig. 6.11 for hierarchical ((a)+(b)) and direct polymerization ((c)+(d), *cf.* subsection 6.2.4 for discussion). For polymerization at 185 °C an APCN of 1.9 is found, which is even below the value of 2.0 for infinite 1D pore chains. For enhanced surface temperatures of 250 °C and 375 °C °C the APCNs increase to 3.0. Nevertheless, these comparatively low values underpin the branched and rugged nature of the covalent networks as already discernible in the STM images.

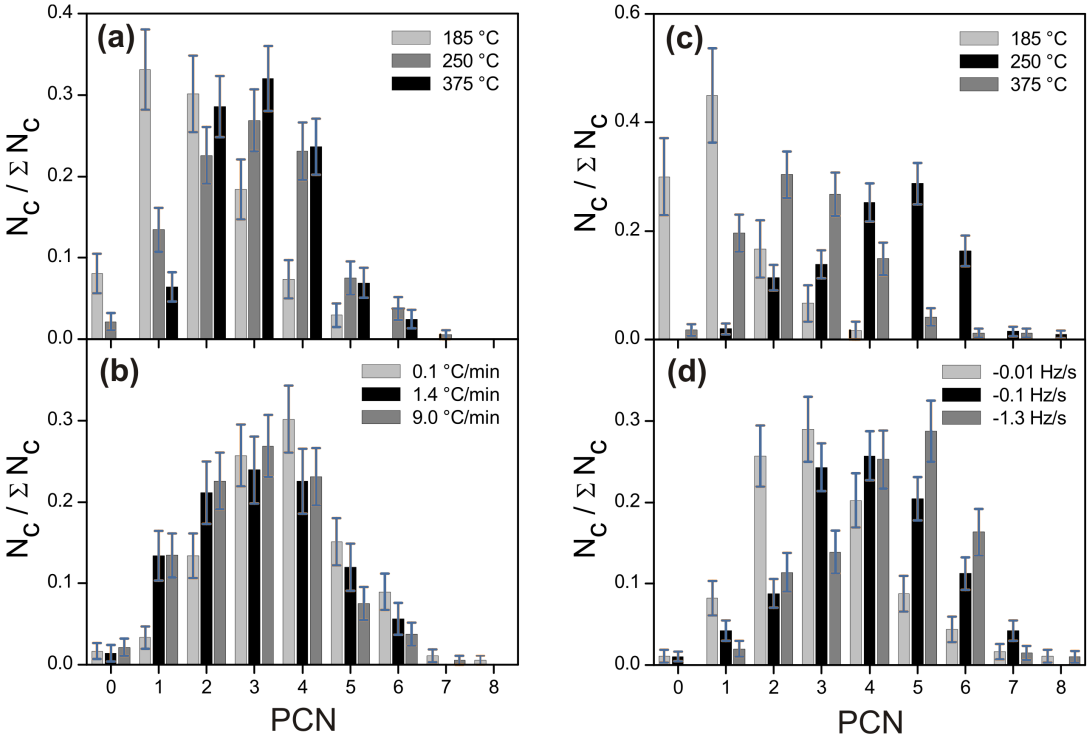

Figure 6.11: Pore coordination number (PCN) distributions of covalent networks obtained by hierarchical polymerization *via* RT deposition and subsequent annealing (a)+(b) or *via* high temperature deposition (c)+(d). Different reaction parameters were studied: for hierarchical polymerization (a) different surface temperatures for comparable heating rates of 6.3 °C min^{-1} or 8.9 °C min^{-1}, (b) different heating rates for a similar surface temperature of 250 °C; for direct polymerization (c) different surface temperatures for a similar deposition rate corresponding to 1.3 Hz min^{-1}, (d) different deposition rates for a similar surface temperature of 250 °C. The respective parameters are indicated in the legends. N_C corresponds to the number of adjacent closed pores.

XPS Measurements

In addition to the STM experiments, XPS measurements were conducted to monitor the chemical changes during on-surface Ullmann coupling of BIB on Au(111). XP spectra of Br 3d, I 3d and C 1s core levels were acquired either directly after RT deposition or after annealing at 250 °C (*cf.* Fig. 6.12 and 6.13).

In the XP spectra of iodine shown in Fig. 6.12(a), one spin-orbit doublet (I 3d$_{5/2}$ BE 618.8 eV) is observed directly after RT deposition on Au(111), which is attributed to split off iodine chemisorbed on Au(111).[180] This binding energy is in agreement with XPS measurements of purely iodine terminated Au(111) surfaces, where binding energies of 619.0 eV (I 3d$_{5/2}$) are reported.[180] After annealing at 250 °C, the I 3d spectra appear similar as at RT, indicating no further chemical changes of iodine. This suggests that iodine is already completely split off after RT deposition of BIB onto Au(111) and stably binds to the surface. After annealing at 250 °C the

I 3d spin-orbit doublet exhibits comparable peak intensities as obtained after RT deposition, indicating negligible iodine desorption from the surface at increased substrate temperatures. In accordance with STM observations, the deiodination is already completed after RT deposition.

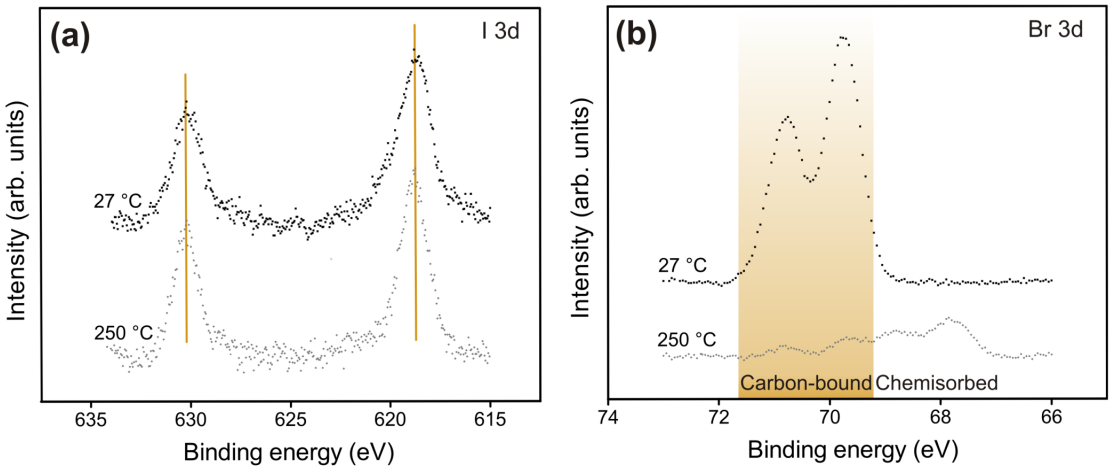

Figure 6.12: XP spectra of I 3d (a) and Br 3d (b) on Au (111) acquired either directly after RT deposition of BIB or after subsequent annealing to 250 °C. (a) The I 3d spectra exhibit a single spin-orbit doublet at the same binding energy for both temperatures. (b) For Br 3d after RT deposition only one spin-orbit doublet is obtained, whereas after annealing two chemically shifted doublets are observed indicating chemical changes.

The corresponding Br 3d spectrum after RT deposition is shown in Fig. 6.12(b). It clearly exhibits only one spin-orbit doublet (Br $3d_{5/2}$ BE 69.8 eV), which is assigned to carbon-bound bromine. Accordingly, no debromination takes place upon room temperature deposition. After annealing at 250 °C, two shifted spin-orbit doublets are obtained with binding energies of 69.8 eV and 67.8 eV (Br $3d_{5/2}$), respectively, resulting from two chemically distinct bromine species. Similar binding energies are also reported for 5-bromouracil on Au(111), where Br $3d_{5/2}$ BE 69.85 eV is referred to carbon-bound bromine and Br $3d_{5/2}$ BE 67.67 eV is assigned to surface-bound bromine.[183] In contrast to iodine, annealing at 250 °C already activates the bromine desorption from the surface, as indicated by the decreasing peak intensities.

Furthermore, C 1s core level spectra are acquired for BIB on Au(111) (Fig. 6.13). The C 1s RT spectrum is centered at 284.1 eV with a small shoulder at higher binding energy, which is attributed to bromine-bound carbon.[183] Subsequent annealing at 250 °C eliminates the small shoulder, confirming the assumption of intact C−Br bonds after RT deposition. A similar binding energy of 285.1 eV for C−Br bonds is also reported for 5-bromouracil on Au(111).[183] After annealing to 250 °C, the C 1s core level spectrum shifts slightly to lower binding energy. A similar behavior is theoretically predicted for Ullmann coupling of bromobenzene on Au(111).[111] Thereby, the conversion from bromobenzene to biphenyl is attributed

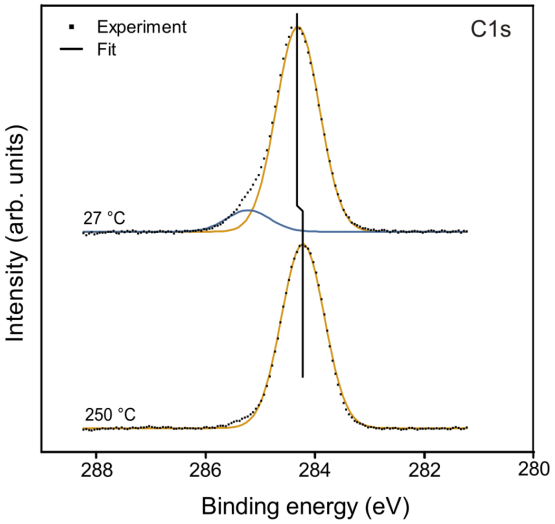

Figure 6.13: XP spectra of C 1s directly after RT deposition of BIB on Au(111) and after subsequent annealing to 250 °C. After RT deposition a main peak with a shoulder was observed. The shoulder vanishes after annealing at 250 °C. The C 1s spectra are fitted with Gaussian profiles.

to a chemical shift of ∼0.15 eV toward lower binding energies. The observation of core level shifts indicates an effect of bromine atoms on the binding energy of carbon atoms in the organic backbone.

The C 1s spectra on Au(111) differ significantly from the C 1s spectra for BIB on Ag(111) in Fig. 7.5 (chapter 7), where the main peak exhibits shoulders both at higher and lower binding energy. The shoulder at higher binding energy corresponds to C−Br bonds as on Au(111). The small shoulder at 283.5 eV, however, is attributed tonewly formed C−Ag bonds, in agreement with reported lower binding energies for metal-linked carbon.[57, 85, 4] Accordingly, the absence of a low energy shoulder on Au(111) excludes the occurrence of organometallic bonds and indicates the direct formation of covalent bonds.

The XPS measurements of BIB on Au(111) confirm the STM data discussed before. The XP spectra of I 3d and Br 3d clearly demonstrate that iodine cleavage already occurs at room temperature, whereas bromine remains still stably bound to the organic backbone. Furthermore, the absence of a low binding energy shoulder in the C 1s spectra allow to exclude the formation of organometallic structures on Au(111). Accordingly, covalently linked dimers with stably bound bromine substituents are formed after RT deposition as already concluded from the STM data. Subsequent annealing at 250 °C activates the debromination and the formation of covalent bonds. Furthermore, the Br 3d spectra reveal the presence of still carbon-bound bromine after annealing in small amounts, which might influence the network growth process of the covalent network.

6.2.4 Direct Polymerization of 1,3-bis(*p*-bromophenyl)-5-(*p*-iodophenyl) benzene

In further experiments, direct polymerization was studied by depositing BIB onto preheated Au(111) at temperatures above the debromination threshold. Upon adsorption, both iodine and bromine substituents are readily split off, resulting in surface-stabilized triradicals that subsequently undergo polymerization. Yet, also for high temperature deposition a sequential polymerization with preceding dimerization can not *a priori* be excluded, because both debromination and deiodination rates become enhanced. Hence, we postulate that the dissociation of both bromine and iodine is completed before coupling, *i.e.* triradicals are the relevant species in direct polymerization. This hypothesis is supported by an experimental comparison of BIB versus TBB (the fully brominated analogue) polymerization. Statistical analysis of networks obtained by deposition of either monomer onto Au(111) held at 250 °C yield similar pore geometry distributions within experimental error (*cf.* subsection 6.2.6). For direct polymerization the influences of surface temperature and deposition rate were independently studied in two series of experiments. The eigenfrequency decline $\Delta f/\Delta t$ of a quartz crystal microbalance (QCMB) serves as a quantitative measure of the deposition rate, whereby 1 Hz s^{-1} corresponds to about 0.1 monolayer min^{-1}.

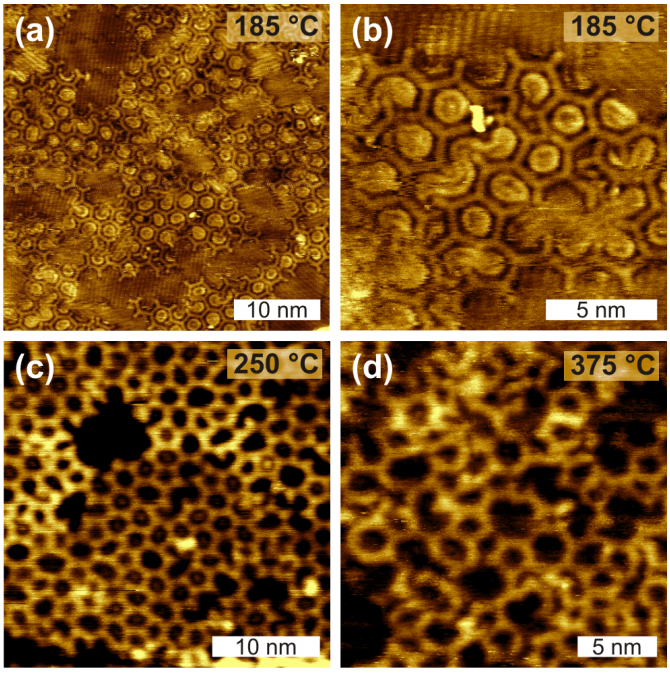

Figure 6.14: STM images of covalent networks prepared by RT deposition of BIB onto Au(111) held at 185 °C (a)+(b), 250 °C (c), and 375 °C (d) (*cf.* subsection 6.2.2 for tunneling parameters). The deposition rate corresponded to $\sim 1.3\,\mathrm{Hz\,s^{-1}}$ for all experiments. After deposition the samples were kept at the respective temperature for ~ 15 min.

The temperature influence was studied by depositing BIB with a constant rate onto preheated Au(111) held at 185 °C, 250 °C, and 375 °C, respectively. As already

evident from the STM images in Fig. 6.14, polymerization at either lower (185 °C) or higher (375 °C) temperature results in lower quality networks as compared to an intermediate temperature of 250 °C. The corresponding pore geometry distributions in Fig. 6.15(a) reveal clear trends: The probability of pentagonal pores increases markedly with increasing substrate temperature, whereas the probability of regular hexagonal pores decreases. Similar to hierarchical polymerization this behavior changes when the probabilities are renormalized to $\Sigma N_i + N_0$ (Fig. 6.15(b)), especially for low temperature polymerization. The high amount of open pores obtained for 185 °C significantly reduces the probability of hexagonal pores. For 250 °C and 375 °C, instead, the renormalization causes only minor changes.

Similar to the hierarchical polymerization, APCNs were evaluated for the different reaction parameters, the underlying PCN distributions are summarized in Fig. 6.11. The APCN yields very low value of 1.1 for 185 °C, which can be attributed to the high number of open pores. Surface temperatures of 250 °C and 375 °C result in increased APCNs of 4.3 and 2.6, respectively.

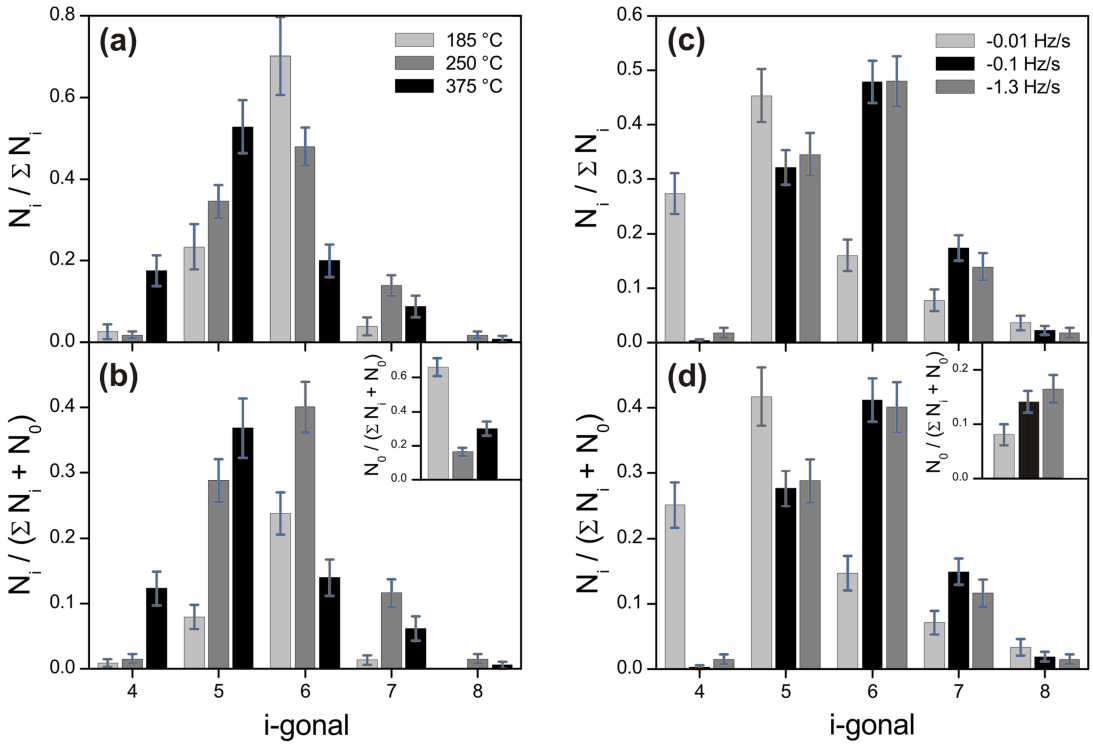

Figure 6.15: Pore geometry distributions of covalent networks prepared by direct polymerization *via* high temperature deposition. (a)+(b) In all experiments the substrate was heated to 185 °C, 250 °C, and 375 °C and the deposition rates corresponded to ∼1.3 Hz s^{-1}. (c)+(d) The substrate was held at 250 °C, whereas different deposition rates corresponding to 0.01 Hz s^{-1}, 0.1 Hz s^{-1}, and 1.3 Hz s^{-1} were applied. N_i and N_0 have similar meaning as in Fig. 6.9, *i.e.* the probabilities of i-gonal pores in (a) are referred to ΣN_i, whereas in (b) N_i is normalized to $\Sigma N_i + N_0$. The inset in (b) shows N_0 for the different temperatures.

The influence of deposition rate in direct polymerization was studied by a further set of experiments where the deposition rates were varied over two orders of magnitude from $<0.01\,\mathrm{Hz\ s^{-1}}$ to $1.3\,\mathrm{Hz\ s^{-1}}$. The surface temperature was kept constant at 250 °C. In order to exclude an additional influence of surface coverage, the deposition times were adjusted to yield comparable coverages. Representative STM images are summarized in Fig. 6.16. Deposition with intermediate and high rates results in comparable network qualities with no statistically significant differences. Counterintuitively, extremely slow deposition ($<0.01\,\mathrm{Hz\ s^{-1}}$) results in drastically impaired network quality as already discernible in the STM images (Fig. 6.16(c)+(d)).

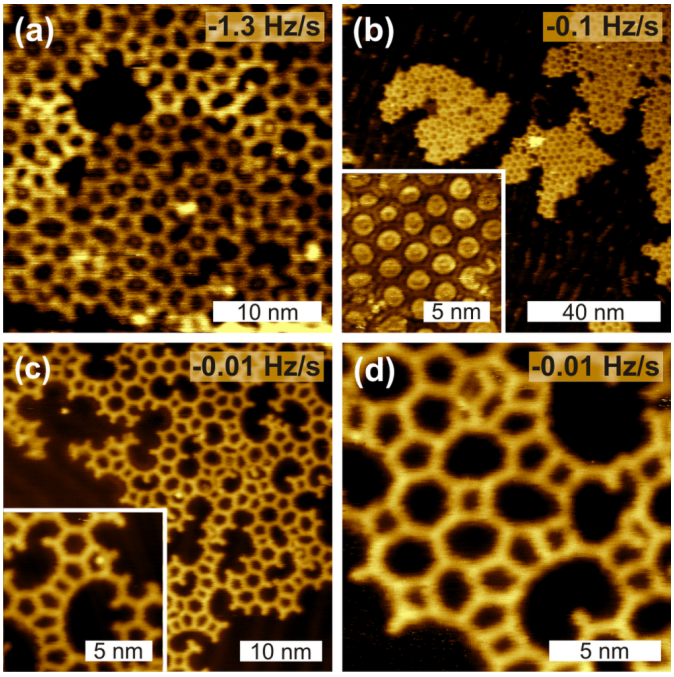

Figure 6.16: STM images of covalent networks prepared by deposition of BIB with varying deposition rates corresponding to $1.3\,\mathrm{Hz\,s^{-1}}$ (a), $0.1\,\mathrm{Hz\,s^{-1}}$ (b), and $0.01\,\mathrm{Hz\,s^{-1}}$ (c)+(d) (*cf.* subsection 6.2.2 for tunneling parameters). In each experiment the surface was held at a constant temperature of 250 °C.

Consequently, the pore geometry distributions in Fig. 6.15 show extraordinary high probabilities of pentagonal and even tetragonal pores. On the other hand, slower deposition aids in decreasing the relative amount of open pores. Slight differences were also found in the APCN, where deposition with a rate of $<0.01\,\mathrm{Hz\ s^{-1}}$ leads to a value of 3.2, whereas the two higher deposition rates result in APCN values of 4.0 ($0.1\,\mathrm{Hz\ s^{-1}}$) and 4.3 ($1.3\,\mathrm{Hz\ s^{-1}}$).

To improve the network quality, fundamental insights into defect formation and the influence of kinetic reaction parameters are required. A clear experimental result is the increased number of open pores at lower polymerization temperatures (185 °C), similarly observed for both hierarchical and direct polymerization. Two different reasons account for this observation: incomplete debromination and

insufficient lateral mobility of the building blocks. At domain boundaries dangling molecular lobes with a length of (0.8 ± 0.1) nm can be inferred from STM images, indicating still brominated phenyl rings (*cf.* Fig. 6.17). In this case, the polymerization can only proceed along the reactive sites and these pores cannot be completed.

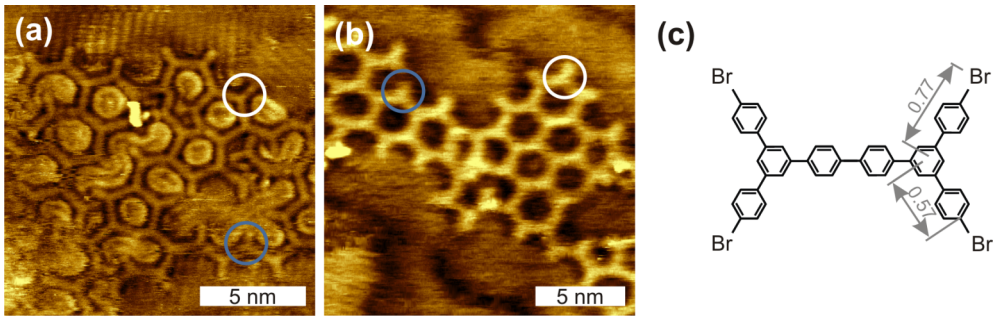

Figure 6.17: STM images of covalent networks obtained by (a) direct (-1.7 V, 4.8 pA) and (b) hierarchical (+1.5 V, 8.7 pA) polymerization at 185 °C. (c) DFT geometry optimized structure of TBQ exemplifying the length difference between brominated and debrominated molecules. Debromination would lead to ∼0.2 nm shorter molecular lobes, a length difference that can be safely identified in the STM images (white versus blue circles).

Previously, Fasel *et al.* studied the influence of surface mobility by comparing the polymerization of iodinated CHP on the (111) facets of Cu, Ag, and Au.[56] On Cu(111) branched networks were observed, the compactness was improved for Au(111), and densely packed networks were obtained on Ag(111). In accompanying MC simulations the network morphology similarly changed from branched to compact for lower ratios of coupling to diffusion. Analogously, we observe more compact networks for higher surface temperature, both in our experiments and Monte Carlo simulations (*vide infra*). By analogy with the results for different surfaces, we conclude that the limited lateral monomer mobility at lower temperatures and the presence of still not fully activated, *i.e.* debrominated sites account for the large amount of open pores. In this respect, higher surface temperatures should be advantageous. On the other hand, higher temperatures similarly enhance the probabilities for irregular pores, as statistically deduced for both direct and hierarchical polymerization.

In the following, kinetic arguments are used to rationalize irregular pore formation. The enhanced amount of pentagonal pores with increasing temperature may be explained by postulating a highly strained and thus high energy transition state.[106] During the course of polymerization each pentamer unit can either become a regular hexagonal pore by adding one more monomer in a bimolecular reaction or an irregular pentagonal pore through an unimolecular macro-ring closure. The bimolecular reaction rate is proportional to the concentration of activated, *i.e.* dehalogenated monomers which increases with deposition rate. On the other hand, the unimolecular ring-closing requires only thermal energy to overcome the barrier. Accordingly, the reaction rate increases with temperature. As a result, the network

morphology is determined by the competition between bimolecular and unimolecular reactions, in full agreement with the experimental findings, where either higher surface temperatures or extremely low deposition rates promote the formation of irregular pores.

6.2.5 Direct *versus* Hierarchical Polymerization

Comparison of directly and hierarchically polymerized networks reveals certain morphological differences. Hierarchical polymerization leads to small densely packed domains that are frequently interconnected by molecular chains and single pore wide strings, while comparable motifs have never been observed for direct polymerization. Differences regarding irregular pore formation are more subtle: Direct polymerization exhibits a steeper temperature gradient for the probability of pentagonal pores than hierarchical polymerization. Irregular pores are also crucial for hierarchical polymerization, but are less prone to thermal activation. Furthermore, at 185 °C the APCN for hierarchical polymerization at 185 °C of 1.9 is even higher than 1.1 for direct polymerization. For higher surface temperatures, instead, the APCN of hierarchical polymerization does not exceed 3.0, occupying an intermediate position between 4.3 for direct polymerization at 250 °C and 2.6 for 375 °C.

6.2.6 Direct Polymerization of 1,3,5-tris(*p*-bromophenyl)benzene

Additionally to BIB as molecular building block also the direct polymerization was studied for the fully brominated analogue 1,3,5-tris(*p*-bromophenyl)benzene (TBB) at 250 °C (*cf.* Fig. 6.18). In the experiments the surface coverage and deposition rates of BIB and TBB were comparable. Therefore the Knudsen cell temperature was adjusted to 166 °C for TBB deposition.

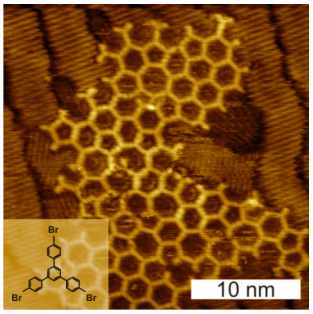

Figure 6.18: STM image (+0.90 V, 5.1 pA) of a covalent network obtained by direct polymerization of TBB at 250 °C. In the inset the chemical structure of TBB is shown.

The corresponding pore geometry distributions of TBB are depicted in Fig. 6.19. For comparison the pore geometry distributions of BIB are also shown. Within

experimental error the pore geometry distributions of BIB and TBB for a surface temperature of 250 °C are similar, but distinct from those of BIB for lower and higher surface temperature. These additional results support the working hypothesis that in direct polymerization, *i.e.* upon high temperature deposition both iodine and bromine substituents are readily dissociated before coupling.

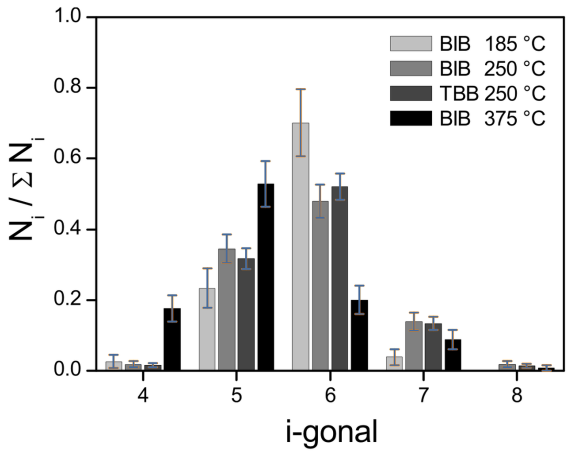

Figure 6.19: Pore geometry distribution of covalent networks obtained by direct polymerization *via* high temperature deposition. The histogram compares data of fully brominated TBB deposited at 250 °C and data of BIB deposited at 185 °C, 250 °C, and 375 °C (same data set as in Fig. 6.9). N_i correspond to the number of i-gonal pores. The probabilities of i-gonal pores is referred to the total number of closed pores (ΣN_i).

6.2.7 DFT Calculations of Molecular Structures

To obtain structural data of TBQ (*i.e.* dimerized BIB) for comparison with STM data, DFT calculations were conducted using Gaussian03 with a B3LYP functional and a 6-31G* basis set for carbon and hydrogen, applying standard convergence criteria.[174] Additionally, the geometry of a hypothetic organometallic dimer (Fig. 6.20(b)) was optimized, using a LanL2DZ basis set for gold. The surface was not explicitly taken into account, but the structures were constrained to a planar conformation by fixing the z-coordinates of all atoms to zero. The results in Fig. 6.20 indicate markedly different lengths for the fully covalent quaterphenyl and the organometallic backbones, respectively.

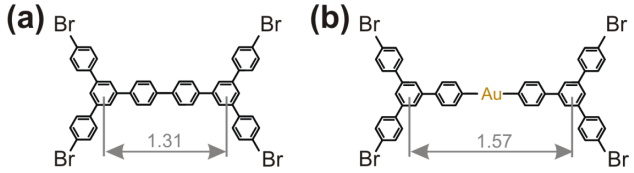

Figure 6.20: DFT optimized structures of (a) TBQ and (b) a hypothetic organometallic complex comprised of two deiodinated BIB molecules and one gold atom.

6.2.8 Conclusion

The influence of different kinetic reaction parameters on the morphology and defect density of covalent networks obtained by on-surface Ullmann coupling was studied on Au(111) using an iodine and bromine functionalized aromatic precursor. At room temperature iodine is selectively split off, whereas bromine dissociation requires further thermal activation. This well documented temperature dependence of C−Br and C−I bond cleavage is confirmed by the present study and utilized for a comparative study of different polymerization protocols. Both hierarchical and direct polymerization resulted in covalent networks with open and irregular (tetragonal, pentagonal, heptagonal, and octagonal) pores as the most common defects. The effect of different reaction parameters was identified by a quantitative comparison of the network quality based on a statistical analysis of STM data.

For both polymerization protocols similar temperature effects were observed: Lower surface temperatures result in a relatively large amount of open pores. In accordance with Monte Carlo simulations (*cf.* subsection 4.2.1) this can be attributed to the limited lateral mobility of building blocks. Furthermore, not yet completed debromination may also play an important role at lower temperatures. Increased surface temperatures do not only reduce the amount of open pores, but also improve the compactness of the networks as expressed in increased APCNs. On the other hand, irregular pores dominate at higher surface temperature, an effect that is more pronounced for direct polymerization. Interestingly, direct polymerization with very slow deposition rates, *i.e.* deposition over the course of several hours, slightly improves the APCN, but results in the highest observed amounts of pentagonal and tetragonal pores. Both experimentally observed dependencies can consistently be explained by a kinetic competition between bimolecular reactions that result in regular hexagonal pores and unimolecular ring-closing reactions that result in irregular tetragonal or pentagonal pores. The unimolecular reaction is associated with a notable activation barrier, hence becomes favored at higher temperatures, whereas the bimolecular reaction rate depends on the availability of monomers and increases with deposition rate. These on-surface polymerization results bear a noteworthy analogy to solution chemistry: In a kinetic competition between polymerization and cyclization, the latter becomes favored under high-dilution conditions,[184] which corresponds to low deposition rates in on-surface chemistry.

Based on the statistical analysis we propose mutually exclusive structure optimization criteria for covalent networks: lower surface temperatures reduce irregular pore formation; however, by the same token limited diffusivity and incomplete debromination at lower temperatures result in dendritic morphologies and more open pores. Consequently, surfaces that promote high diffusivity of SSRs would be the better choice. Yet, this implementation of on-surface Ullmann coupling still requires the catalytic activity of surfaces for initiating the polymerization by carbon-halogen bond cleavage, which limits this approach to metals. In this respect, Au(111) might still be the best compromise in terms of sufficient catalytic activity and low diffusion barriers for activated monomers.

The differences between on-surface Ullmann coupling of BIB and TBQ, *i.e.* direct and hierarchical polymerization are surprisingly small. Even though both protocols result in networks with relatively high defect densities, the preceding dimerization step in hierarchical polymerization aids in reducing the amount of irregular pores, especially at higher surface temperatures. It is particularly instructive to compare the present results to the hierarchical polymerization of *trans*-Br_2I_2 tetraphenyl-porphyrin.[107] In direct comparison to the fully brominated analogue, Grill *et al.* infer an overall improvement of the structural quality with notably enhanced domain size and postulate this to be a direct consequence of low defect densities. Indeed, in the present case high amounts of irregular pores coincide with low APCN, possibly indicating a correlation between defect densities and domain sizes. An important difference between the two systems is that in the first step *trans*-Br_2I_2 tetraphenyl-porphyrin can already polymerize into 1D chains that are subsequently interlinked into 2D networks. Thereby, a templating molecular zipper effect of the 1D chain, which is however absent in the present system, appears to be a key ingredient for improving the structural quality. This molecular zipper effect was also observed in a metal-directed polymerization by Lin *et al.* on Au(111), where the presence of extrinsic copper adatoms was found to induce a templating effect that leads to structural improvement.[185] In summary, hierarchical polymerization based on the different activation barriers of deiodination and debromination on gold surfaces is a reliable approach to either initiate and study different polymerization pathways or to sequentially build up more complex structures in on-surface Ullmann coupling.

Chapter 7

On-Surface Ullmann Coupling *via* Organometallic Intermediates

J. Eichhorn, T. Strunskus, A. Rastgoo-Lahrood, D. Samanta, M. Schmittel, and M. Lackinger. On-Surface Ullmann Polymerization *via* Intermediate Organometallic Networks on Ag(111). *Chem. Commun.* 50 (2014), 7680-7682.

The influence of organometallic intermediates for on-surface polymerization *via* Ullmann coupling was studied on Ag(111). The polymerization progress was monitored by X-ray photoelectron spectroscopy (XPS). Scanning-Tunneling-Microscopy (STM) was used to characterize organometallic and covalent networks and to identify the temperature regimes for organometallic and covalent bond formation.

7.1 Introduction

In recent years, low-dimensional organic covalent materials gained significant research interest due to unprecedented chemical and mechanical stability. In combination with their adjustable electronic properties, 2D polymers are perfectly suited for applications in (opto)electronic devices.[18, 17] On-surface Ullmann polymerization has become an established route for the tailored fabrication of covalent nanostructures.[85, 106, 101, 180] The observed low structural quality of 2D networks originates from the irreversibility of the newly formed C−C cross-links, inhibiting error correction processes. On the other hand, non-covalent self-assembly is well known to yield highly ordered structures. In this respect, the formation of metastable organometallic chains [57, 19] and even 2D networks as established intermediates in on-surface Ullmann couplings may be used for improving the structural quality of 2D covalent networks. A necessity therefore is the reversibility of the organometallic bonds. Since C−Cu bonds are relatively strong, silver appears to be the most promis-

ing metal due to its intermediate reactivity. In this context, detailed knowledge about the temperature regimes where organometallic C−Ag−C bonds may become reversible and where they are irreversibly converted into covalent C−C bonds is required.

Herein, we use finely-tuned tempering protocols to demonstrate a stepwise on-surface Ullmann polymerization leading to 2D porous covalent networks on Ag(111) *via* intermediate organometallic networks. On-surface Ullmann coupling relies on the catalytic properties of the metal surface for cleavage of weakly bound halogen substituents. Thereby, the halogen side groups play a decisive role: at room temperature, deiodination takes place spontaneously on Cu, Ag, and Au.[106, 56] On the other hand, bromine is fully split off on copper,[84, 83] partially on silver,[85] and not at all on gold [112]. On copper and silver surfaces, the surface-bound radicals directly form metastable organometallic structures based on carbon–metal–carbon bonds. On gold, however, organometallic bonds are only occasionally observed.[87] An important difference is the formation of disordered organometallic networks on copper as opposed to partly ordered structures on silver.[86] These observations suggest irreversibility of C−Cu bonds that are normally stronger than C−Ag bonds. On the other hand, the relatively low binding energy of the C−Ag bond promotes its reversibility. This enables the possibility of structural rearrangements during the organometallic intermediate of the polymerization. Accordingly, self-assembly of organometallic precursor networks may be used to improve the structural quality of subsequently formed covalent networks. One requirement, however, is that the organometallic network can undergo equilibration and error correction prior to the formation of irreversible covalent bonds by releasing the interlinking silver atom. Interestingly, on copper this conversion is not always possible, because the required temperature for breaking C−Cu bonds can exceed the thermal stability of the monomer.[186]

7.2 Experimental Details

All experiments were conducted with a home-built scanning tunneling microscope under UHV conditions with a base pressure below 2×10^{-10} mbar. Lattice parameters and intermolecular distances were derived from STM images with an accuracy of 5% after calibration with atomically resolved topographs of highly oriented pyrolytic graphite(001). Single crystal Ag(111) surfaces were prepared by cycles of Ar^+ ion-sputtering at 500 eV and annealing at 500 °C for 40 minutes. The cleanliness of the substrate was verified by STM imaging prior to deposition.

To study potential differences between I and Br functionalization, 1,3-bis(*p*-bromophenyl)-5-(*p*-iodophenyl)benzene (BIB, *cf.* inset Fig. 7.1(c)) was chosen as monomer. BIB was deposited by means of a Knudsen cell onto Ag(111) either held at room temperature (RT) or heated above 125 °C. The resulting structures and the influence of different preparation protocols - RT deposition and heating vs. high temperature deposition - were studied by STM.

Additionally, X-ray photoelectron spectroscopy (XPS) was conducted for detailed insights into the temperature dependence of debromination. XPS measurements were carried out in a Prevac UHV system at the HESGM beamline at Helmholtz-Zentrum Berlin. The preparation chamber of the UHV system was equipped with facilities for sample sputtering and heating. The sample preparation was similar to the STM experiments. Bromine 3d XP spectra were acquired with a Scienta R3000 electron analyzer at normal electron emission using an excitation energy of 450 eV and a pass energy of 50 eV. The binding energy of Ag $3d_{5/2}$ at 368.3 eV was used as an internal energy reference. A linear background was subtracted from all spectra.

7.3 From Organometallic Intermediates to Covalent Networks

RT deposition of BIB onto Ag(111) results in a great variety of coexisting partly ordered arrangements that range from close packed to porous structures (Fig. 7.1). The three-fold structure of BIB is clearly recognizable in the STM images. The STM data feature two different contrasts, whereby the molecules are either interconnected by clearly discernible bright (Fig. 7.1(a)) or by barely visible faint dots (Fig. 7.1(b)-(d)). In both cases, the center–to–center distance of adjacent molecules is (1.62 ± 0.1) nm. In accordance with DFT calculations, this length is characteristic for organometallic complexes with straight intermolecular C−Ag−C bonds (*cf.* Fig. 7.6). The formation of these complexes at RT indicates the availability of a sufficient amount of Ag adatoms. For the unconnected molecular lobes of BIB, STM reveals clear length differences, suggesting the coexistence of intact brominated and already debrominated molecular side groups (Fig. 7.1(b), highlighted by circles). Deiodinated and debrominated side groups, however, are indistinguishable in the organometallic complexes. For RT deposition iodine cleavage is well documented on Ag(111),[56] whereas the temperature progression of the debromination is less clear. To obtain detailed insights, XP spectra of Br 3d core levels were acquired after each step of successive heating (*cf.* Fig. 7.2(a)). Directly after RT deposition, two chemically shifted spin-orbit doublets were observed, confirming the coexistence of carbon-bound (Br $3d_{5/2}$ BE 69.8 eV) and chemisorbed bromine (Br $3d_{5/2}$ BE 68.2 eV).[187] Accordingly, after RT deposition ∼38 % of the bromine is split off, and the debromination is completed to ∼92 % after annealing at 260 °C. A similar behavior, yet with a substantially higher amount of initial RT debromination was already reported for brominated tetrathienoanthracene on Ag(111).[85]

Guided by the XPS data, the temperature dependent formation of fully cross-linked organometallic structures was studied by tempering at 125 °C to activate almost complete debromination. The corresponding STM image in Fig. 7.2(b) shows rather regular hexagonal porous networks based on straight intermolecular bonds as

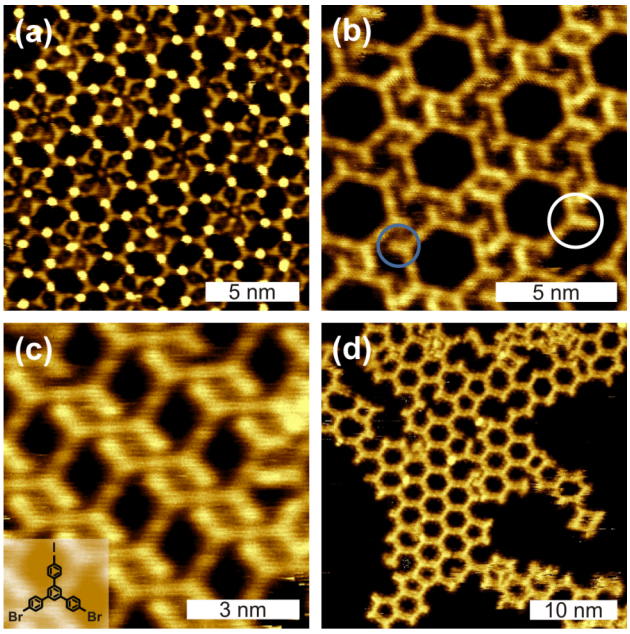

Figure 7.1: STM images of self-assembled structures directly obtained after RT deposition of BIB onto Ag(111). In (b) intact as well as debrominated side groups can be distinguished (white/grey circle). The inset in (c) depicts the chemical structure of BIB. ((a) − 0.9 V, 8.0 pA, (b) + 1.1 V, 3.9 pA, (c) − 0.3 V, 10.0 pA, (d) + 4.0 V, 5.5 pA,)

commonly observed for Ag^+ complexes. Both the bond length and the faint dots between the molecules indicate organometallic networks. Upon heating, further debromination initiates the reorganization of the partly ordered RT arrangements and results in the formation of regular porous organometallic networks. In contrast to RT deposition, the obtained networks largely feature fully debrominated monomers. Some defects, however, can be attributed to still intact brominated molecular lobes (Fig. 7.2(b)). The rearrangement processes inevitably require breaking and reorganization of organometallic bonds, confirming the dynamic properties of C−Ag bonds on Ag(111) below ∼125 °C. Newly formed covalent bonds have never been observed in this temperature range.

To investigate the effect of the preparation protocol samples were also prepared by depositing BIB directly onto preheated substrates. The resulting organometallic networks exhibit comparable structural quality (*cf.* Fig. 7.2(c)/(d)). However, now monomers can also become trapped within the pores, *i.e.* even at the elevated deposition temperature monomers cannot escape the pores by diffusing below or above the organic framework. A further intention of these experiments was to determine the temperature threshold for conversion of organometallic into covalent bonds. In this context, the question arises whether the organometallic networks can be equilibrated before the irreversible formation of covalent networks sets in. Therefore, a series of experiments with increasing substrate temperatures was performed, the corresponding STM data for BIB deposition onto preheated Ag(111) at 170 °C are shown in Fig. 7.2(c) and (d). Both images depict the same sample

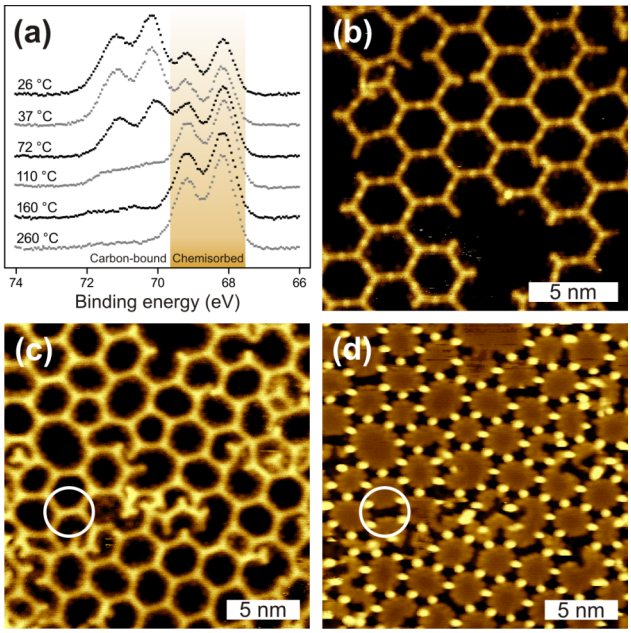

Figure 7.2: (a) XP spectra of Br 3d on Ag(111) after RT deposition and successive tempering steps up to 260 °C. STM images of BIB deposited on Ag(111) (b) at RT with subsequent heating to 125 °C (+ 0.8 V, 11.0 pA) and (c)+(d) preheated to 170 °C (7.8 pA, (c) + 0.90 V, (d) +0.23 V). The white circles highlight individual already formed covalent bonds.

area, however, with different STM contrasts, originating from different bias voltages. In Fig. 7.2(c) the silver atoms are barely visible, whereas in (d) they are clearly resolved as protrusions while the organic backbones of the network appear as depressions. Most intermolecular bonds are mediated by silver atoms and can thus be assigned to organometallic bonds. On the other hand, few interconnections do not exhibit any internal STM contrast and are (0.26 ± 0.1) nm shorter in length, indicating the formation of covalent bonds. In conclusion, the conversion from organometallic to covalent bonds becomes noticeable at ∼170 °C, while individual covalent bonds can already form at ∼155 °C (*cf.* Fig. 7.4(a)). The coexistence of both types of bonds suggests a gradual conversion, where by the molecules retain their original arrangement. Remarkably, the temperature regimes for the reversible equilibration of the C−Ag bonds and the final irreversible C−C bond formation are well separated. This opens up the possibility to employ self-assembly and error correction of organometallic networks prior to conversion into covalent networks. The potential of this approach was further explored by tempering samples with extremely slow heating rates (0.07 or 0.31 °C min^{-1}) with the intention to establish and retain organometallic equilibrium structures before covalent bond formation occurs.

Again, room vs. high temperature deposition was compared. In both approaches, polymerization was initiated by slow tempering to 250 °C. The resulting networks shown in Fig. 7.3 exhibit decreased intermolecular distances of 1.3 nm and a lattice parameter of 2.3 nm, indicating covalent interlinks. RT deposition with subsequent

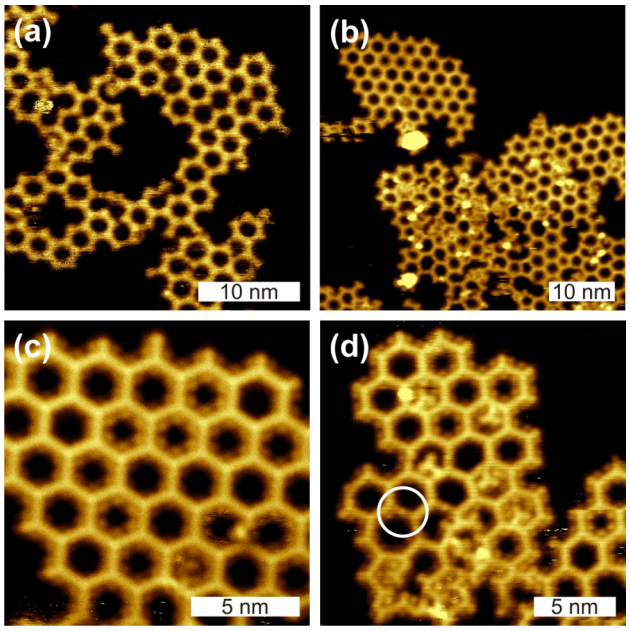

Figure 7.3: STM images of covalent networks on Ag(111). BIB was deposited at RT ((a) +1.9 V, 24.7 pA) or deposited onto a preheated sample at 150 °C (b)-(d). Subsequently, both samples were tempered up to 250 °C ((b)+(c) +3.9 V, 4.6 pA, (d) +2.6 V, 5.5 pA). The circle in (d) marks a still present organometallic bond in a disordered domain.

tempering results in branched networks with predominantly hexagonal pores and only few irregular pentagonal pores (*cf.* Fig. 7.3(a)). Samples prepared by deposition on a preheated surface (150 °C) and subsequent tempering up to 250 °C, instead, feature more compact networks (Fig. 7.3(b)-(d)), whereby highly ordered and more disordered domains can be distinguished. The close-up image in Fig. 7.3(d) provides a detailed view of a more irregular domain. Although the relative amount of regular hexagonal pores is still relatively high, irregular single pentagonal pores can be recognized and molecules trapped within the pores are frequently observed. Surprisingly, few organometallic bonds are still present, but were only observed in disordered regions (*cf.* Fig. 7.3(d)).

In STM images of both organometallic and covalent networks regularly arranged bright dots are clearly discernible within the pores. The bright dots can be assigned to split off halogen atoms (Fig. 7.4(b)-(d)), yet a distinction between Br and I based on the STM contrast is not possible. The STM images in Fig. 7.4 depict adsorbed halogens in the pores of an (b) organometallic and (c)/(d) covalent network, respectively. The STM images in Fig. 7.4(c) and (d) were acquired from the same sample area, yet with different tunneling parameters. The differences in STM contrast especially of the halogen atoms suggest a distinct dependence on the imaging parameters.

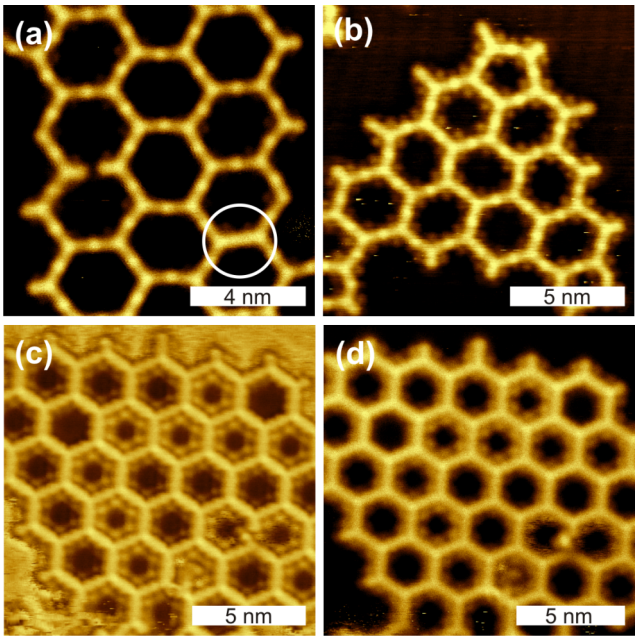

Figure 7.4: STM images of BIB derived (a)+(b) organometallic and (c)+(d) covalent networks on Ag(111). (a) was acquired after RT deposition of BIB onto Ag(111) and subsequent tempering at 155 °C and (b) after deposition at 125 °C. Most of the molecules are interconnected by organometallic bonds, where the silver atom appears as small protrusion. Yet, single covalent bonds with reduced length are already observed, an example is indicated by the white circle. The sample in (b)+(c) was prepared by deposition at 150 °C and subsequent tempering to 250 °C. In both networks the split off halogens are clearly discernible at defined positions within the pores. ((a) + 0.88 V, 7.4 pA, (b) + 0.5 V, 6.2 pA, (c) + 1.6 V, 9.2 pA, (d) + 3.9 V, 4.6 pA)

7.4 Additional XPS Measurements

In addition to the Br 3d spectra in Fig. 7.2, the XP spectra of I 3d and C 1s core levels are acquired directly after RT deposition as well as after subsequent annealing at 250 °C. The I 3d spectra in Fig. 7.5(a) show a single spin-orbit doublet(I $3d_{5/2}$ BE 619.1 eV) for both sample treatments with similar binding energy. In agreement with previous studies,[188, 189] the doublet is assigned to chemisorbed iodine on Ag(111). Additionally, the absence of chemical changes between RT deposition and subsequent annealing indicates the complete cleavage of C−I bonds already at RT, followed by the chemisorption of iodine on the surface.

The C 1s RT spectrum in Fig. 7.5(b) is centered at 284.6 eV with small shoulders at higher and lower binding energy, respectively. Similar to the XPS measurements on Au(111) in section 6.2, the peak at higher binding energy is assigned to bromine-bound carbon. The small shoulder at 283.5 eV is attributed to C−Ag bonds, in agreement with a reported lowering of binding energy for metal-linked carbon.[57, 85, 4] After subsequent annealing at 250 °C, the C 1s core level spectrum is shifted toward higher binding energy and contains only a single component at 284.8 eV. A similar chemical shift of 0.2 eV was also observed for Ullmann coupling of 1,4-dibromobenzene

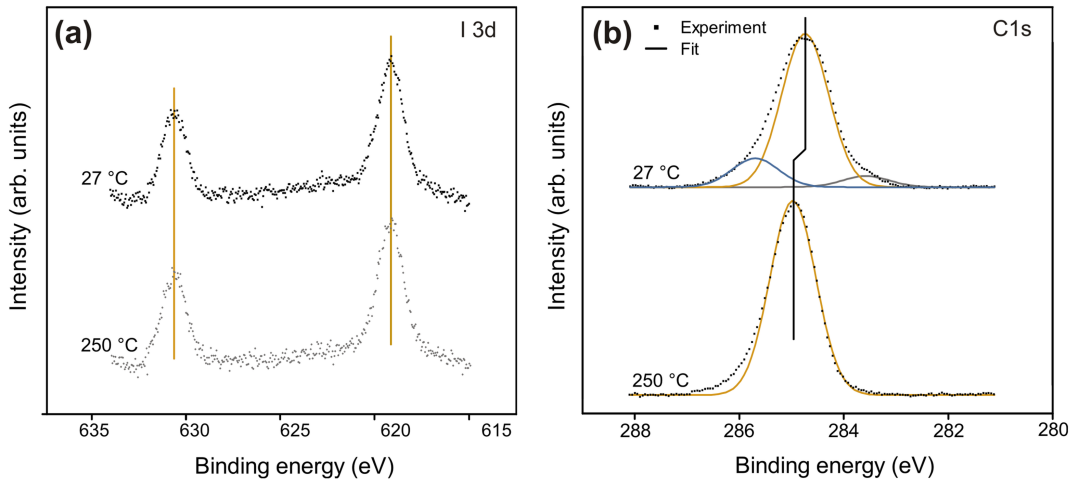

Figure 7.5: XP spectra of I 3d (a) and C 1s (b) directly after RT deposition of BIB onto Ag(111) and after subsequent annealing at 250 °C. (a) For I 3d a single spin-orbit doublet is obtained at both temperatures, respectively, with similar binding energies for I $3d_{5/2}$ and I $3d_{3/2}$. (b) After RT deposition the C 1s spectra exhibit two shoulders at lower and higher binding energy. After annealing at 250 °C, however, the two shoulders have vanished. The C 1s spectra are fitted with Gaussian profiles.

on Cu(110) after annealing the organometallic RT structure to ∼230 °C.[57, 190] Thereby, the chemical shift is attributed to the different types of atoms *i.e.* copper or carbon, which are bound at the previously halogenated sites of the molecular building block. These effect is typical for conjugated aromatic systems, where charge delocalization occurs over the entire molecule. Moreover, for Ullmann coupling of bromobenzene on Ag(111), C 1s core-level shifts are calculated by Björk *et al.* [111]. Thereby, chemical shift to higher binding energies are reported for the transition from C−Ag to C−C bonds. Both studies indicate that the small chemical shift of about 0.2 eV may arise from the conversion of organometallic intermediates to covalent networks.

Accordingly, the XPS measurements corroborate the STM data, where the formation of organometallic structures is similarly observed at RT. The disappearance of both bromine- and Ag-bound carbon shoulders after annealing at 250 °C indicates covalent interlinking of the molecular building blocks.

7.5 DFT Calculations of the Reaction Intermediates and Products

DFT gas phase calculations were conducted for comparing the bond lengths of anticipated structures with experimental data. Therefore, the geometries of covalent dimers and organometallic complexes were optimized with Gaussian03 applying standard convergence criteria. For hydrogen, carbon, and bromine a B3LYP functional and a 6-31G* basis set were used, whereas a LanL2DZ basis set was chosen for silver.[174]

The substrate's influence was mimicked by fixing the z-coordinates of all atoms to zero and constraining the structures to a planar conformation. In accordance with these calculations, the bond length difference between covalent and organometallic cross-links amounts to 0.27 nm (Fig. 7.6). This length difference is large enough to unambiguously distinguish organometallic from covalent bonds in STM experiments.

Figure 7.6: DFT geometry optimized structures of covalent dimers (a)+(c) and the corresponding organometallic complex (b) in the gas phase. All distances are given in nm.

The fully brominated covalent dimer was optimized to estimate length differences between still brominated and already debrominated molecular lobes. The distance from the outermost phenyl ring of the quarterphenyl backbone to the peripheral bromine atom is 0.77 nm. This is 0.20 nm longer than the distance to the outermost carbon atom (Fig. 7.6(c)). Based on these calculations, we anticipate that brominated and debrominated molecular lobes can be clearly distinguished in STM images by the apparent length of the respective molecular lobe.

7.6 Summary

In summary, we studied the formation of 2D covalent networks by on-surface Ullmann coupling on Ag(111) with focus on intermediate organometallic networks. In contrast to the polymerization of the comparable monomer 1,3,5-tris(4-bromophenyl)benzene (TBB) on Au(111),[112] and Cu(111),[84] the covalent networks on Ag(111) exhibit a higher degree of regularity with structurally perfect domains extending up to 10 nm (*cf.* Fig. 7.3(c)). Fasel et al. account differences in monomer mobility as important surface influence on the structural quality of 2D polymers.[56] Additionally, we propose a decisive role of organometallic intermediates, in particular, on Ag(111). By moderate tempering at ∼125 °C highly ordered organometallic networks could be stabilized, while a sizable conversion to covalent networks sets in at markedly higher temperatures of ∼170 °C.

Chapter 8

Summary and Outlook

In this thesis, the synthesis of 2D organic nanostructures is studied on metal surfaces under ultra-high vacuum conditions. The molecular assemblies are characterized by means of scanning tunneling microscopy and X-ray photoelectron spectroscopy. The combination of a local, real-space probe technique and space-averaging spectroscopy allows the complementary determination of molecular structures and of chemical states. The identification of bond types and binding configurations is supported by density functional theory calculations of geometry optimized building blocks.

Non-Covalent Assembly
In the first part, 2D organic nanostructures are fabricated by means of supramolecular self-assembly of melem, a triply amino substituted heptazine ring, on Ag(111) (chapter 5). Melem self-assembly yields various coexisting, mostly porous polymorphs. Apart from one densely packed structure, all porous polymorphs can be described as a systematic series of structures, where the distance between adjacent pores increases in increments of one melem molecule. Interestingly, only two different hydrogen bond motifs, namely side-by-side and head-to-tail, account for the versatility of the melem structures. Various polymorphs feature both intermolecular bonding schemes, but also exclusively head-to-tail and side-by-side stabilized arrangements are obtained. The origin of the polymorphism is attributed to increased molecule–substrate interactions arising from the larger heptazine backbone as compared to the s-triazine backbone of melamine. The contribution of intermolecular hydrogen bonds to the overall binding energy is similar for both backbones. However, the increased backbone size changes the delicate balance between molecule–molecule and molecule–substrate interactions. Under these conditions, optimization of hydrogen bonds may not be the decisive criterion for structure selection anymore. Additionally, the occurrence of polymorphism for melem self-assembly is also promoted by the greater versatility of melem to form various different intermolecular interactions.

On-Surface Polymerization
The main part of the presented thesis focuses on the synthesis of low-dimensional covalent nanostructures by means of on-surface polymerization. To this end, different coupling reactions and substrate materials, but also different reaction parameters are

investigated. First, coupling of terminal alkynes is studied in section 6.1 on Cu(111). Thereby, different polymerization pathways are observed such as trimerization, homo-, and cross-coupling, but also sequential combinations of these basic reactions are obtained. During the trimerization of three ethynyl groups to benzene no byproduct is released, whereas homo-coupling forms butadiyne bridges under the release of hydrogen. Accordingly, the surface will not be contaminated by adsorbed byproducts, which can hamper the network growth on the surface. Nevertheless, the formation of regular, long-range ordered networks is limited by the occurrence of a multitude of different polymerization pathways without any indication for regioselectivity. Inevitably, disordered covalent structures with distinct basic motifs are observed. The investigation of different reaction parameters reveals that the regioselectivity of the coupling reaction cannot be improved by the optimization of annealing temperature or time. For the improvement of the network quality and morphology, however, it would be highly interesting to explore different surface materials and crystallographic orientations with more pronounced anisotropy to suppress undesirable side reactions.

In contrast to on-surface coupling of terminal alkynes, Ullmann coupling is highly selective on gold, silver and copper substrates. Nevertheless, the covalent networks suffer from high defect densities, a lack of long-range order, and small domain sizes. The low network quality can be attributed to the kinetic irreversibility of newly formed covalent bonds impairing rearrangement and error correction processes.

For on-surface Ullmann coupling on Au(111) (section 6.2), the influence of different reaction parameters on the morphology of covalent networks is investigated. As a measure for the network quality, defect densities are evaluated and quantified by statistical analysis of STM data, whereby open pores, ideal hexagonal and closed irregular (tetragonal, pentagonal, heptagonal, octagonal) pores are considered. Thereby, direct as well as hierarchical polymerization are comparatively studied using an asymmetrically functionalized precursor with iodine and bromine as functional groups (1,3-bis(*p*-bromophenyl)-5-(*p*-iodophenyl)benzene, BIB). In both polymerization pathways similar temperature effects are observed, however, with slightly different characteristics. In principle, lower surface temperatures reduce the amount of irregular pores within the covalent network. Yet, limited diffusivity and incomplete dehalogenation can promote the formation of dendritic morphologies and higher amounts of open pores. Increased surface temperatures, on the other hand, reduce the amount of open pores and improve the compactness of the covalent networks, but the network's quality is impaired by high amounts of irregular pores. In addition to the surface temperature, the influence of heating and deposition rates on the network quality is investigated for hierarchical and direct polymerization, respectively. Thereby, no significant changes of the network quality are observed for different heating rates. However, extremely slow deposition significantly increases the amount of closed irregular pores, especially pentagonal and tetragonal pores. Accordingly, the quality of covalent networks depends on the reaction parameters and can be improved by their optimization. The best network qualities are obtained at intermediate substrate temperatures for both hierarchical and direct polymerization.

On-surface Ullmann coupling of BIB is also studied on Ag(111) (chapter 7). Compared to Au(111), the covalent networks exhibit a higher degree of regularity with structurally perfect domains extending up to 10 nm. The main difference is attributed to the formation of metastable organometallic intermediates during on-surface Ullmann coupling, which is commonly observed on silver and copper surfaces. The formed organometallic structures are usually disordered on copper and partly ordered on silver. This suggest irreversibility of C−Cu bonds in organometallic intermediates, whereas the lower binding energy of C−Ag bonds promotes reversibility and allows error correction processes as already known from non-covalent self-assembly. This opens up the possibility to employ reversible equilibration and error correction of organometallic networks prior to irreversible C−C bond formation in the final polymerization step. On Ag(111) highly ordered organometallic networks are formed after moderate annealing at ∼125 °C for complete dehalogenation, while a sizable conversion to covalent networks sets in at markedly higher temperatures of ∼170 °C. Accordingly, the formation of organometallic intermediates plays the decisive role for the improved network quality as observed on Ag(111).
The results presented in this work enhance the understanding of structure formation on Au(111), Ag(111), and Cu(111). Especially, for the on-surface polymerization of covalent networks, different strategies are contributed to improve the network quality towards long-range ordered structures. In this respect, the most promising approach is to perform molecular self-assembly prior to the final polymerization step.

Outlook

As shown in chapter 7, metal adatoms play a decisive role in on-surface Ullmann coupling. Thus, the application of metal adatoms in on-surface polymerization is highly interesting for the synthesis of tailored molecular nanostructures. It is a promising strategy to enable molecular self-assembly and to control on-surface Ullmann coupling, simultaneously. A systematic implementation of metal atoms in on-surface Ullmann coupling, however, requires a deeper understanding of their catalytic reactivity and properties, but also of error correction processes in organometallic networks in general.
For on-surface Ullmann coupling of BIB on Au(111), for example, preliminary experiments show that the reaction pathway can be significantly influenced by controlled co-deposition of Ag atoms. The adsorbed Ag atoms form an extrinsic two-dimensional adatom gas on the Au(111) surface. The co-deposition of Ag atoms on Au(111) may open up new possibilities to guide the network formation process by the tailored combination of materials with different properties. To investigate the influence of Ag atoms on the Ullmann coupling of BIB, first small amounts of Ag adatoms are deposited on Au(111) and subsequently the BIB molecules are added with submonolayer coverage. After RT deposition, two different, coexisting molecular assemblies are observed, which exhibit a similar appearing molecular arrangement (Fig. 8.1(a)). Both structures base on different dumbbell shape building blocks namely covalently and organometallically linked dimers, which can clearly be distinguished by the length of the organic backbone. For BIB on Au(111), instead,

only covalently linked dimers are observed after RT deposition (*cf.* Fig. 6.6, section 6.2). Accordingly, the formation of organometallic structures can be attributed to the presence of Ag atoms on the surface.

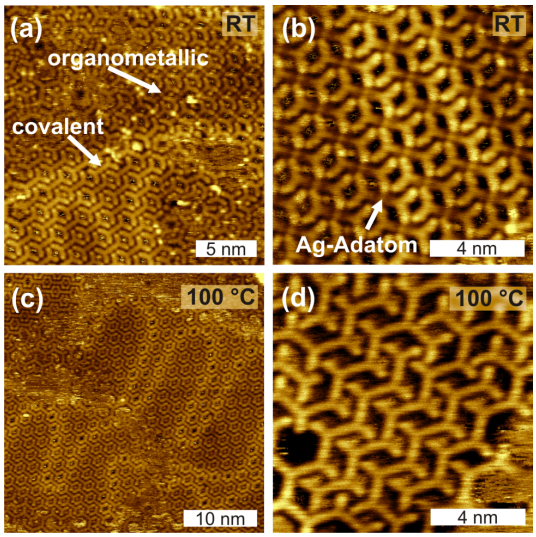

Figure 8.1: STM images of molecular structures obtained for co-deposition of Ag atoms and BIB onto Au(111) (a)+(b) and after annealing to 100 °C (c)+(d). RT deposition results in two self-assembled structures based on organometallic and covalent dimers (a)+(b) ((a) +1.0 V, 7.7 pA, (b) +0.61 V, 4.7 pA). Subsequent annealing at 100 °C already activates debromination and interlinking to covalent chains (c)+(d) ((c) +5.7 V, 16.4 pA, (d) +0.8 V, 4.3 pA).

Subsequent annealing to 100 °C already activates the dehalogenation leading to the formation of covalent chains (Fig. 8.1 (c)+(d)). Furthermore, self-assembled structures of covalently linked dimers are still present, however, no organometalic dimer structures are observed anymore. These results clearly differ from the observations of BIB on pristine Au(111), where debromination occurs only above 175 °C. Interestingly, the temperature progression for dehalogenation is similar to the observation on Ag(111), where $\sim 50\%$ of the bromine is split off at around 72 °C. These preliminary experimental results indicate, that the reaction pathway and the dehalogenation process is significantly influenced by co-deposition of Ag atoms. On the other hand, the mobility of the molecular building blocks on the surface is still determined by the substrate material. Accordingly, the interplay of different material properties can be used to design a specific reaction test bed for on-surface polymerization.
The catalytic reactivity of the Ag atoms opens up the possibility to perform the on-surface polymerization at significantly lower temperatures. Ullmann coupling of BIB on Au(111) has already shown, that reduced substrate temperature facilitates the formation of covalent networks with relatively high amounts of hexagonal pores. Accordingly, the application of Ag atoms in on-surface Ullmann coupling is a promising strategy to hamper the formation of irregular pores and to improve the network quality by reducing the required temperature for dehalogenation.

List of Figures

References

[1] Geim, A. K. and Novoselov, K. S. The rise of graphene. *Nat. Mater.* **6**, 183–191 (2007).

[2] Novoselov, K. S. Nobel lecture: Graphene: materials in the flatland. *Rev. Mod. Phys.* **83**, 837–849 (2011).

[3] Novoselov, K. S., Geim, A. K., Morozov, S. V., Jiang, D., Zhang, Y., Dubonos, S. V., Grigorieva, I. V. and Firsov, A. A. Electric field effect in atomically thin carbon films. *Science* **306**, 666–669 (2004).

[4] Cardenas, L. *et al.* Synthesis and electronic structure of a two-dimensional π-conjugated polythiophene. *Chem. Sci.* **4**, 3263–3268 (2013).

[5] Yusoff, A. R. b. M. *Graphene optoelectronics: synthesis, characterization, properties, and applications* (John Wiley & Sons, 2014).

[6] Luryi, S., Xu, J. and Zaslavsky, A. *Future trends in microelectronics: frontiers and innovations* (John Wiley & Sons, 2013).

[7] Irudayaraj, J. *Biomedical nanosensors* (CRC Press, 2012).

[8] Lackinger, M. and Heckl, W. M. Carboxylic acids: versatile building blocks and mediators for two-dimensional supramolecular self-assembly. *Langmuir* **25**, 11307–11321 (2009).

[9] Griessl, S., Lackinger, M., Edelwirth, M., Hietschold, M. and Heckl, W. M. Self-assembled two-dimensional molecular host-guest architectures from trimesic acid. *Single Mol.* **3**, 25–31 (2002).

[10] Pham, T. A., Song, F., Nguyen, M.-T. and Stohr, M. Self-assembly of pyrene derivatives on Au(111): substituent effects on intermolecular interactions. *Chem. Commun.* (2014).

[11] Gutzler, R., Fu, C., Dadvand, A., Hua, Y., MacLeod, J. M., Rosei, F. and Perepichka, D. F. Halogen bonds in 2D supramolecular self-assembly of organic semiconductors. *Nanoscale* **4**, 5965–5971 (2012).

[12] Gutzler, R., Cardenas, L. and Rosei, F. Kinetics and thermodynamics in surface-confined molecular self-assembly. *Chem. Sci.* **2**, 2290–2300 (2011).

[13] Barth, J. V. Molecular architectonic on metal surfaces. *Annu. Rev. Phys. Chem.* **58**, 375–407 (2007).

[14] Eder, G., Kloft, S., Martsinovich, N., Mahata, K., Schmittel, M., Heckl, W. M. and Lackinger, M. Incorporation dynamics of molecular guests into two-dimensional supramolecular host networks at the liquid-solid interface. *Langmuir* **27**, 13563–13571 (2011).

[15] Gutzler, R. and Perepichka, D. F. π-Electron conjugation in two dimensions. *J. Am. Chem. Soc.* **135**, 16585–16594 (2013).

[16] Sakamoto, J., van Heijst, J., Lukin, O. and Schlüter, D. Two-dimensional polymers: just a dream of synthetic chemists? *Angew. Chem., Int. Ed.* **48**, 1030–1069 (2009).

[17] Perepichka, D. F. and Rosei, F. Extending polymer conjugation into the second dimension. *Science* **323**, 216–217 (2009).

[18] Colson, J. W. and Dichtel, W. R. Rationally synthesized two-dimensional polymers. *Nat. Chem.* **5**, 453–465 (2013).

[19] Wang, W., Shi, X., Wang, S., Van Hove, M. A. and Lin, N. Single-molecule resolution of an organometallic intermediate in a surface-supported Ullmann coupling reaction. *J. Am. Chem. Soc.* **133**, 13264–13267 (2011).

[20] Cai, J. *et al.* Atomically precise bottom-up fabrication of graphene nanoribbons. *Nature* **466**, 470–473 (2010).

[21] Meyer, E., Hug, H. J. and Bennewitz, R. *Scanning probe microscopy: the lab on a tip* (Springer, 2004).

[22] van de Leemput, L. E. C. and van Kempen, H. Scanning tunnelling microscopy. *Rep. Prog. Phys.* **55**, 1165 (1992).

[23] Yao, N. and Wang, Z. *Handbook of microscopy for nanotechnology* (Springer, 2005).

[24] Stroscio, J. A. and Kaiser, W. J. *Scanning tunneling microscopy* (Academic Press, 1993).

[25] Binnig, G., Rohrer, H., Gerber, C. and Weibel, E. Tunneling through a controllable vacuum gap. *Appl. Phys. Lett.* **40**, 178–180 (1982).

[26] Binnig, G., Rohrer, H., Gerber, C. and Weibel, E. Surface studies by scanning tunneling microscopy. *Phys. Rev. Lett.* **49**, 57–61 (1982).

[27] Bardeen, J. Tunnelling from a many-particle point of view. *Phys. Rev. Lett.* **6**, 57–59 (1961).

[28] Tersoff, J. and Hamann, D. R. Theory and application for the scanning tunneling microscope. *Phys. Rev. Lett.* **50**, 1998–2001 (1983).

[29] Tersoff, J. and Hamann, D. R. Theory of the scanning tunneling microscope. *Phys. Rev. B* **31**, 805–813 (1985).

[30] Feuchtwang, T. E. and Cutler, P. H. Tunneling and scanning tunnel microscopy: a critical review. *Phys. Scr.* **35**, 132–140 (1987).

[31] Waser, R. *Nanoelectronics and information technology* (Wiley-VCH Verlag, 2012).

[32] Chen, C. J. Origin of atomic resolution on metal surfaces in scanning tunneling microscopy. *Phys. Rev. Lett.* **65**, 448–451 (1990).

[33] Ochs, O. M. *Entwicklung eines ultrahochvakuumtauglichen Raster-Tunnel-Mirkroskops und Integration in eine bestehende Vakuumanlage.* Master thesis, University of applied sciences Munich (2013).

[34] Eder, G., Schlögl, S., Macknapp, K., Heckl, W. M. and Lackinger, M. A combined ion-sputtering and electron-beam annealing device for the *in vacuo* postpreparation of scanning probes. *Rev. Sci. Instrum.* **82**, 033701 (2011).

[35] Gutzler, R., Heckl, W. M. and Lackinger, M. Combination of a Knudsen effusion cell with a quartz crystal microbalance: *in situ* measurement of molecular evaporation rates with a fully functional deposition source. *Rev. Sci. Instrum.* **81**, 015108 (2010).

[36] Berner, S. *Molecular diffusion and self-organization on metal surfaces: subphthalocyanine on Ag (111).* Ph.D. thesis, University of Basel (2002).

[37] Chusuei, C. C. and Goodman, D. W. X-Ray photoelectron spectroscopy. *Encyclopedia of Physical Science and Technology* **17**, 921–938 (2002).

[38] Moulder, J. F., Stickle, W. F., Sobol, P. E. and Bomben, K. D. *Handbook of X-ray photoelectron spectroscopy* (Perkin Elmer Eden Prairie, 1992).

[39] Hüfner, S. *Photoelectron spectroscopy: principles and applications.* Advanced Texts in Physics (Springer, 2003).

[40] Lee, S. M. *Reference book for composites technology, Band 2* (CRC Press, 1989).

[41] Hubbard, A. T. *The handbook of surface imaging and visualization* (CRC Press, 1995).

[42] Niemantsverdriet, J. *Spectroscopy in catalysis: an introduction* (Wiley-VCH Verlag, 2008).

[43] Briggs, D. *Surface analysis of polymers by XPS and static SIMS.* Cambridge Solid State Science Series (Cambridge University Press, 1998).

[44] Demtröder, W. *Atoms, molecules and photons: an introduction to atomic-, molecular- and quantum physics.* Graduate Texts in Physics (Springer, 2010).

[45] Van der Heide, P. *X-ray photoelectron spectroscopy: an introduction to principles and practices* (John Wiley & Sons, 2011).

[46] De Groot, F. and Kotani, A. *Core level spectroscopy of solids* (CRC press, 2008).

[47] Schädel, M. *The chemistry of superheavy elements* (Springer, 2003).

[48] Helmholtz Center Berlin for Materials and Energy GmbH. *HE-SGM beamline*. http://www.helmholtz-berlin.de (2014/08/04).

[49] Bracco, G. and Holst, B. *Surface science techniques* (Springer, 2013).

[50] VG Scienta. *R3000 XPS/UPS/ARPES*. http://www.vgscienta.com (2014/08/04).

[51] Alfassi, Z. *Determination of trace elements* (John Wiley & Sons, 2008).

[52] Billè, F. *et al.* *Atomic calculation of photoionization cross-sections and asymmetry parameters* . Scientific Computing Sincrotrone Trieste S.C.p.A.: http://ulisse.elettra.trieste.it/services/elements/WebElements.html (2014/08/06).

[53] Kudernac, T., Lei, S. B., Elemans, J. A. A. W. and De Feyter, S. Two-dimensional supramolecular self-assembly: nanoporous networks on surfaces. *Chem. Soc. Rev.* **38**, 402–421 (2009).

[54] Kühnle, A. Self-assembly of organic molecules at metal surfaces. *Curr. Opin. Colloid Interface Sci.* **14**, 157–168 (2009).

[55] Bartels, L. Tailoring molecular layers at metal surfaces. *Nat. Chem.* **2**, 87–95 (2010).

[56] Bieri, M. *et al.* Two-dimensional polymer formation on surfaces: insight into the roles of precursor mobility and reactivity. *J. Am. Chem. Soc.* **132**, 16669–16676 (2010).

[57] Di Giovannantonio, M. *et al.* Insight into organometallic intermediate and its evolution to covalent bonding in surface-confined Ullmann polymerization. *ACS Nano* **7**, 8190–8198 (2013).

[58] Atwood, J. L. and Steed, J. W. *Encyclopedia of supramolecular chemistry* (CRC Press, 2004).

[59] McNaught, A. D. and Wilkinson, A. *IUPAC. Compendium of chemical terminology, 2nd ed.* (Blackwell Scientific Publications, Oxford, 1997).

[60] Desiraju, G. R. The C-H$\cdots$O hydrogen bond: structural implications and supramolecular design. *Acc. Chem. Res.* **29**, 441–449 (1996).

[61] Arunan, E., Desiraju, G. R., Klein, R. A., Sadlej, J., Scheiner, S., Alkorta, I., Clary, D. C., Crabtree, R. H., Dannenberg, J. J. and Hobza, P. Definition of the hydrogen bond (IUPAC Recommendations 2011). *Pure Appl. Chem.* **83** (2011).

[62] Desiraju, G. R. Hydrogen bridges in crystal engineering: Interactions without borders. *Acc. Chem. Res.* **35**, 565–573 (2002).

[63] Desiraju, G. R. Chemistry beyond the molecule. *Nature* **412**, 397–400 (2001).

[64] Israelachvili, J. N. *Intermolecular and surface forces* (Academic press, 2011).

[65] Jeffrey, G. A. *An introduction to hydrogen bonding* (Oxford University Press, 1997).

[66] Arras, E., Seitsonen, A. P., Klappenberger, F. and Barth, J. V. Nature of the attractive interaction between proton acceptors and organic ring systems. *Phys. Chem. Chem. Phys.* **14**, 15995–16001 (2012).

[67] Lackinger, M., Griessl, S., Heckl, W. A., Hietschold, M. and Flynn, G. W. Self-assembly of trimesic acid at the liquid-solid interface - a study of solvent-induced polymorphism. *Langmuir* **21**, 4984–4988 (2005).

[68] Gutzler, R., Sirtl, T., Dienstmaier, J. F., Mahata, K., Heckl, W. M., Schmittel, M. and Lackinger, M. Reversible phase transitions in self-assembled monolayers at the liquid-solid interface: temperature-controlled opening and closing of nanopores. *J. Am. Chem. Soc.* **132**, 5084–5090 (2010).

[69] Steiner, T., Starikov, E. B., Amado, A. M. and Teixeiradias, J. J. C. Weak hydrogen-bonding. Part 2. The hydrogen-bonding nature of short C-H$\cdots$Pi contacts - crystallographic, spectroscopic and quantum-mechanical studies of some terminal alkynes. *J. Chem. Soc., Perkin Trans. 2* 1321–1326 (1995).

[70] Chung, K.-H., Park, J., Kim, K. Y., Yoon, J. K., Kim, H., Han, S. and Kahng, S.-J. Polymorphic porous supramolecular networks mediated by halogen bonds on Ag(111). *Chem. Commun.* **47**, 11492–11494 (2011).

[71] Politzer, P., Murray, J. S. and Clark, T. Halogen bonding: an electrostatically-driven highly directional noncovalent interaction. *Phys. Chem. Chem. Phys.* **12**, 7748–7757 (2010).

[72] Clark, T., Hennemann, M., Murray, J. and Politzer, P. Halogen bonding: the s-hole. *J. Mol. Model.* **13**, 291–296 (2007).

[73] Metrangolo, P., Meyer, F., Pilati, T., Resnati, G. and Terraneo, G. Halogen bonding in supramolecular chemistry. *Angew. Chem., Int. Ed.* **47**, 6114–6127 (2008).

[74] Lommerse, J. P. M., Stone, A. J., Taylor, R. and Allen, F. H. The nature and geometry of intermolecular interactions between halogens and oxygen or nitrogen. *J. Am. Chem. Soc.* **118**, 3108–3116 (1996).

[75] Politzer, P., Murray, J. S. and Clark, T. Halogen bonding and other sigma-hole interactions: a perspective. *Phys. Chem. Chem. Phys.* **15**, 11178–11189 (2013).

[76] Metrangolo, P., Pilati, T. and Resnati, G. Halogen bonding and other noncovalent interactions involving halogens: a terminology issue. *CrystEngComm* **8**, 946–947 (2006).

[77] Metrangolo, P., Murray, J. S., Pilati, T., Politzer, P., Resnati, G. and Terraneo, G. Fluorine-centered halogen bonding: a factor in recognition phenomena and reactivity. *Cryst. Growth Des.* **11**, 4238–4246 (2011).

[78] Bosch, E. and Barnes, C. L. Triangular halogen-halogen-halogen interactions as a cohesive force in the structures of trihalomesitylenes. *Cryst. Growth Des.* **2**, 299–302 (2002).

[79] Politzer, P., Lane, P., Concha, M., Ma, Y. and Murray, J. An overview of halogen bonding. *J. Mol. Model.* **13**, 305–311 (2007).

[80] Behr, A. *Organometallic compounds and homogeneous catalysis* (Wiley-VCH Verlag, 2000).

[81] Pruchnik, F. P. *Organometallic chemistry of the transition elements*. Modern Inorganic Chemistry (Springer, 1990).

[82] Crabtree, R. H. *The organometallic chemistry of the transition metals* (John Wiley & Sons, 2014).

[83] Walch, H., Gutzler, R., Sirtl, T., Eder, G. and Lackinger, M. Material- and orientation-dependent reactivity for heterogeneously catalyzed carbon-bromine bond homolysis. *J. Phys. Chem. C* **114**, 12604–12609 (2010).

[84] Gutzler, R., Walch, H., Eder, G., Kloft, S., Heckl, W. M. and Lackinger, M. Surface mediated synthesis of 2D covalent organic frameworks: 1,3,5-tris(4-bromophenyl)benzene on graphite(001), Cu(111), and Ag(110). *Chem. Commun.* 4456–4458 (2009).

[85] Gutzler, R. *et al.* Ullmann-type coupling of brominated tetrathienoanthracene on copper and silver. *Nanoscale* **6**, 2660–2668 (2014).

[86] Bieri, M., Blankenburg, S., Kivala, M., Pignedoli, C. A., Ruffieux, P., Müllen, K. and Fasel, R. Surface-supported 2D heterotriangulene polymers. *Chem. Commun.* **47**, 10239–10241 (2011).

[87] Saywell, A., Gren, W., Franc, G., Gourdon, A., Bouju, X. and Grill, L. Manipulating the conformation of single organometallic chains on Au(111). *J. Phys. Chem. C* **118**, 1719–1728 (2013).

[88] Clayden, J., Greeves, N. and Warren, S. *Organic chemistry* (Oxford University Press, 2012).

[89] Berg, J., Tymoczko, J. and Stryer, L. *Biochemistry* (W. H. Freeman, 2002).

[90] Sivakumar, P., Kodolov, V., Zaikov, G. and Haghi, A. *Nanostructure, nanosystems, and nanostructured materials: theory, production and development* (Apple Academic Press Inc., CRC Press, 2013).

[91] Chi, L. *Nanotechnology: nanostructured surfaces* (WILEY-VCH Verlag, 2010).

[92] Riedel, E. *Allgemeine und Anorganische Chemie* (De Gruyter, 1999).

[93] Zumdahl, S. and Zumdahl, S. *Chemistry* (Cengage Learning, 2013).

[94] Wulfsberg, G. *Inorganic chemistry* (University Science Books, 2000).

[95] Okuyama, T. and Maskill, H. *Organic chemistry: a mechanistic approach* (OUP Oxford, 2013).

[96] Vollhardt, K. P. C. and Schore, N. E. *Organische Chemie (4. Auflgage)* (WILEY-VCH Verlag, 2005).

[97] Schlögl, S., Sirtl, T., Eichhorn, J., Heckl, W. M. and Lackinger, M. Synthesis of two-dimensional phenylene-boroxine networks through *in vacuo* condensation and on-surface radical addition. *Chem. Commun.* **47**, 12355–12357 (2011).

[98] Müller, U. *Inorganic structural chemistry* (John Wiley & Sons, 2007).

[99] Barth, J. V., Costantini, G. and Kern, K. Engineering atomic and molecular nanostructures at surfaces. *Nature* **437**, 671–679 (2005).

[100] Ullmann, F. and Bielecki, J. Über Synthesen in der Biphenylreihe. *Ber. Dtsch. Chem. Ges.* **34**, 2174–2185 (1901).

[101] Grill, L., Dyer, M., Lafferentz, L., Persson, M., Peters, M. V. and Hecht, S. Nano-architectures by covalent assembly of molecular building blocks. *Nat. Nanotech.* **2**, 687–691 (2007).

[102] Xi, M. and Bent, B. E. Mechanisms of the Ullmann coupling reaction in adsorbed monolayers. *J. Am. Chem. Soc.* **115**, 7426–7433 (1993).

[103] Blake, M. M., Nanayakkara, S. U., Claridge, S. A., Fernandez-Torres, L. C., Sykes, E. C. H. and Weiss, P. S. Identifying reactive intermediates in the Ullmann coupling reaction by scanning tunneling microscopy and spectroscopy. *J. Phys.Chem. A* **113**, 13167–13172 (2009).

[104] Björk, J., Zhang, Y.-Q., Klappenberger, F., Barth, J. V. and Stafström, S. Unraveling the mechanism of the covalent coupling between terminal alkynes on a noble metal. *J. Phys. Chem. C* **118**, 3181–3187 (2014).

[105] Chen, M., Xiao, J., Steinrück, H.-P., Wang, S., Wang, W., Lin, N., Hieringer, W. and Gottfried, J. M. Combined photoemission and scanning tunneling microscopy study of the surface-assisted Ullmann coupling reaction. *J. Phys. Chem. C* **118**, 6820–6830 (2014).

[106] Schlögl, S., Heckl, W. M. and Lackinger, M. On-surface radical addition of triply iodinated monomers on Au(111) - the influence of monomer size and thermal post-processing. *Surf. Sci.* **606**, 999–1004 (2012).

[107] Lafferentz, L., Eberhardt, V., Dri, C., Africh, C., Comelli, G., Esch, F., Hecht, S. and Grill, L. Controlling on-surface polymerization by hierarchical and substrate-directed growth. *Nat. Chem.* **4**, 215–220 (2012).

[108] Eichhorn, J., Strunskus, T., Rastgoo-Lahrood, A., Samanta, D., Schmittel, M. and Lackinger, M. On-surface Ullmann polymerization *via* intermediate organometallic networks on Ag(111). *Chem. Commun.* **50**, 7680–7682 (2014).

[109] Kittelmann, M., Nimmrich, M., Lindner, R., Gourdon, A. and Kühnle, A. Sequential and site-specific on-surface synthesis on a bulk insulator. *ACS Nano* **7**, 5614–5620 (2013).

[110] Blanksby, S. J. and Ellison, G. B. Bond dissociation energies of organic molecules. *Acc. Chem. Res.* **36**, 255–263 (2003).

[111] Björk, J., Hanke, F. and Stafström, S. Mechanisms of halogen-based covalent self-assembly on metal surfaces. *J. Am. Chem. Soc.* **135**, 5768–5775 (2013).

[112] Blunt, M. O., Russell, J. C., Champness, N. R. and Beton, P. H. Templating molecular adsorption using a covalent organic framework. *Chem. Commun.* **46**, 7157–7159 (2010).

[113] Glaser, C. Beiträge zur Kenntniss des Acetenylbenzols. *Ber. Dtsch. Chem. Ges.* **2**, 422–424 (1869).

[114] Siemsen, P., Livingston, R. C. and Diederich, F. Acetylenic coupling: a powerful tool in molecular construction. *Angew. Chem., Int. Ed.* **39**, 2632–2657 (2000).

[115] Hay, A. S. Oxidative Coupling of Acetylenes. II. *J. Org. Chem.* **27**, 3320–3321 (1962).

[116] Jiang, J. X., Su, F., Niu, H., Wood, C. D., Campbell, N. L., Khimyak, Y. Z. and Cooper, A. I. Conjugated microporous poly(phenylene butadiynylene)s. *Chem. Commun.* 486–488 (2008).

[117] Batsanov, A. S., Collings, J. C., Fairlamb, I. J. S., Holland, J. P., Howard, J. A. K., Lin, Z. Y., Marder, T. B., Parsons, A. C., Ward, R. M. and Zhu, J. Requirement for an oxidant in Pd/Cu co-catalyzed terminal alkyne homocoupling to give symmetricale 1,4-sisubstituted 1,3-diynes. *J. Org. Chem.* **70**, 703–706 (2005).

[118] Fairlamb, I. J. S., Bäuerlein, P. S., Marrison, L. R. and Dickinson, J. M. Pd-catalysed cross coupling of terminal alkynes to diynes in the absence of a stoichiometric additive. *Chem. Commun.* 632–633 (2003).

[119] Yuan, S. W., Dorney, B., White, D., Kirklin, S., Zapol, P., Yu, L. P. and Liu, D. J. Microporous polyphenylenes with tunable pore size for hydrogen storage. *Chem. Commun.* **46**, 4547–4549 (2010).

[120] Kyriakou, G., Kim, J., Tikhov, M. S., Macleod, N. and Lambert, R. M. Acetylene coupling on Cu(111): formation of butadiene, benzene, and cyclooctatetraene. *J. Phys. Chem. B* **109**, 10952–10956 (2005).

[121] Zhang, Y.-Q. *et al.* Homo-coupling of terminal alkynes on a noble metal surface. *Nat. Commun.* **3**, 1286 (2012).

[122] Gao, H.-Y., Wagner, H., Zhong, D., Franke, J.-H., Studer, A. and Fuchs, H. Glaser coupling at metal surfaces. *Angew. Chem., Int. Ed.* **52**, 4024–4028 (2013).

[123] Zhou, H., Liu, J., Du, S., Zhang, L., Li, G., Zhang, Y., Tang, B. Z. and Gao, H.-J. Direct visualization of surface-assisted two-dimensional diyne polycyclotrimerization. *J. Am. Chem. Soc.* **136**, 5567–5570 (2014).

[124] Cirera, B., Zhang, Y.-Q., Björk, J., Klyatskaya, S., Chen, Z., Ruben, M., Barth, J. V. and Klappenberger, F. Synthesis of extended graphdiyne wires by vicinal surface templating. *Nano Lett.* **14**, 1891–1897 (2014).

[125] Cote, A. P., Benin, A. I., Ockwig, N. W., O'Keeffe, M., Matzger, A. J. and Yaghi, O. M. Porous, crystalline, covalent organic frameworks. *Science* **310**, 1166–1170 (2005).

[126] Cote, A. P., El-Kaderi, H. M., Furukawa, H., Hunt, J. R. and Yaghi, O. M. Reticular synthesis of microporous and mesoporous 2D covalent organic frameworks. *J. Am. Chem. Soc.* **129**, 12914–12915 (2007).

[127] Feng, X., Ding, X. and Jiang, D. Covalent organic frameworks. *Chem. Soc. Rev.* **41**, 6010–6022 (2012).

[128] Ding, S.-Y., Gao, J., Wang, Q., Zhang, Y., Song, W.-G., Su, C.-Y. and Wang, W. Construction of covalent organic framework for catalysis: Pd/COF-LZU1 in Suzuki-Miyaura coupling reaction. *J. Am. Chem. Soc.* **133**, 19816–19822 (2011).

[129] Uribe-Romo, F. J., Hunt, J. R., Furukawa, H., Klöck, C., O'Keeffe, M. and Yaghi, O. M. A crystalline imine-linked 3D porous covalent organic framework. *J. Am. Chem. Soc.* **131**, 4570–4571 (2009).

[130] Zwaneveld, N. A. A., Pawlak, R., Abel, M., Catalin, D., Gigmes, D., Bertin, D. and Porte, L. Organized formation of 2D extended covalent organic frameworks at surfaces. *J. Am. Chem. Soc.* **130**, 6678–6679 (2008).

[131] Mortimer, M. and Taylor, P. *Chemical kinetics and mechanism* (Royal Society of Chemistry, 2002).

[132] Kepcija, N., Zhang, Y.-Q., Kleinschrodt, M., Björk, J., Klyatskaya, S., Klappenberger, F., Ruben, M. and Barth, J. V. Steering on-surface self-assembly of high-quality hydrocarbon networks with terminal alkynes. *J. Phys. Chem. C* **117**, 3987–3995 (2013).

[133] Kolasinski, K. W. *Surface science: foundations of catalysis and nanoscience* (John Wiley & Sons, 2008).

[134] Eichhorn, J., Nieckarz, D., Ochs, O., Samanta, D., Schmittel, M., Szabelski, P. J. and Lackinger, M. On-surface Ullmann coupling: the influence of kinetic reaction parameters on the morphology and quality of covalent networks. *ACS Nano* **8**, 7880–7889 (2014).

[135] Eichhorn, J., Heckl, W. M. and Lackinger, M. On-surface polymerization of 1,4-diethynylbenzene on Cu(111). *Chem. Commun.* **49**, 2900–2902 (2013).

[136] Dienstmaier, J. F., Mahata, K., Walch, H., Heckl, W. M., Schmittel, M. and Lackinger, M. On the scalability of supramolecular networks - high packing density *vs* optimized hydrogen bonds in tricarboxylic acid monolayers. *Langmuir* **26**, 10708–10716 (2010).

[137] Dmitriev, A., Lin, N., Weckesser, J., Barth, J. V. and Kern, K. Supramolecular assemblies of trimesic acid on a Cu(100) surface. *J. Phys. Chem. B* **106**, 6907–6912 (2002).

[138] Li, Z., Han, B., Wan, L. J. and Wandlowski, T. Supramolecular nanostructures of 1,3,5-benzene-tricarboxylic acid at electrified Au(111)/0.05 M H_2SO_4 interfaces: an *in situ* scanning tunneling microscopy study. *Langmuir* **21**, 6915–6928 (2005).

[139] Kampschulte, L., Lackinger, M., Maier, A. K., Kishore, R. S. K., Griessl, S., Schmittel, M. and Heckl, W. M. Solvent induced polymorphism in supramolecular 1,3,5-benzenetribenzoic acid monolayers. *J. Phys. Chem. B* **110**, 10829–10836 (2006).

[140] Ruben, M., Payer, D., Landa, A., Comisso, A., Gattinoni, C., Lin, N., Collin, J. P., Sauvage, J. P., De Vita, A. and Kern, K. 2D supramolecular assemblies of benzene-1,3,5-triyl-tribenzoic acid: temperature-induced phase transformations and hierarchical organization with macrocyclic molecules. *J. Am. Chem. Soc.* **128**, 15644–15651 (2006).

[141] Matthey, D., Wang, J. G., Wendt, S., Matthiesen, J., Schaub, R., Laegsgaard, E., Hammer, B. and Besenbacher, F. Enhanced bonding of gold nanoparticles on oxidized TiO_2(110). *Science* **315**, 1692–1696 (2007).

[142] Silly, F., Shaw, A. Q., Castell, M. R., Briggs, G. A. D., Mura, M., Martsinovich, N. and Kantorovich, L. Melamine structures on the Au(111) surface. *J. Phys. Chem. C* **112**, 11476–11480 (2008).

[143] Schmitz, C. H., Ikonomov, J. and Sokolowski, M. Two commensurate hydrogen-bonded monolayer structures of melamine on Ag(111). *Surf. Sci.* **605**, 1–6 (2011).

[144] Theobald, J. A., Oxtoby, N. S., Phillips, M. A., Champness, N. R. and Beton, P. H. Controlling molecular deposition and layer structure with supramolecular surface assemblies. *Nature* **424**, 1029–1031 (2003).

[145] Perdigao, L. M. A., Perkins, E. W., Ma, J., Staniec, P. A., Rogers, B. L., Champness, N. R. and Beton, P. H. Bimolecular networks and supramolecular traps on Au(111). *J. Phys. Chem. B* **110**, 12539–12542 (2006).

[146] Madueno, R., Räisanen, M. T., Silien, C. and Buck, M. Functionalizing hydrogen-bonded surface networks with self-assembled monolayers. *Nature* **454**, 618–621 (2008).

[147] Eddaoudi, M., Kim, J., Rosi, N., Vodak, D., Wachter, J., O'Keeffe, M. and Yaghi, O. M. Systematic design of pore size and functionality in isoreticular MOFs and their application in methane storage. *Science* **295**, 469–472 (2002).

[148] Schlickum, U. *et al.* Metal-organic honeycomb nanomeshes with tunable cavity size. *Nano Lett.* **7**, 3813–3817 (2007).

[149] Walch, H., Maier, A. K., Heckl, W. M. and Lackinger, M. Isotopological supramolecular networks from melamine and fatty acids. *J. Phys. Chem. C* **113**, 1014–1019 (2009).

[150] Sattler, A., Pagano, S., Zeuner, M., Zurawski, A., Gunzelmann, D., Senker, J., Müller-Buschbaum, K. and Schnick, W. Melamine-melem adduct phases: investigating the thermal condensation of melamine. *Chem. Eur. J.* **15**, 13161–13170 (2009).

[151] Lotsch, B. V. and Schnick, W. Thermal conversion of guanylurea dicyanamide into graphitic carbon nitride via prototype CN_x precursors. *Chem. Mater.* **17**, 3976–3982 (2005).

[152] Jürgens, B., Irran, E., Senker, J., Kroll, P., Müller, H. and Schnick, W. Melem (2,5,8-triamino-tri-s-triazine), an important intermediate during condensation of melamine rings to graphitic carbon nitride: synthesis, structure determination by X-ray powder diffractometry, solid-state NMR, and theoretical studies. *J. Am. Chem. Soc.* **125**, 10288–10300 (2003).

[153] Schlickum, U. *et al.* Chiral kagome lattice from simple ditopic molecular bricks. *J. Am. Chem. Soc.* **130**, 11778–11782 (2008).

[154] Klappenberger, F. *et al.* Does the surface matter? Hydrogen-bonded chain formation of an oxalic amide derivative in a two- and three-dimensional environment. *ChemPhysChem* **9**, 2522–2530 (2008).

[155] Sattler, A. and Schnick, W. On the crystal structure of melem $C_6N_7(NH_2)_3$. *Z. Anorg. Allg. Chem.* **632**, 238–242 (2006).

[156] Mura, M., Martsinovich, N. and Kantorovich, L. Theoretical study of melamine superstructures and their interaction with the Au(111) surface. *Nanotechnology* **19**, 465704 (2008).

[157] Ye, Y. C., Sun, W., Wang, Y. F., Shao, X., Xu, X. G., Cheng, F., Li, J. L. and Wu, K. A unified model: self-assembly of trimesic acid on gold. *J. Phys. Chem. C* **111**, 10138–10141 (2007).

[158] Xiao, W. D., Feng, X. L., Ruffieux, P., Groning, O., Müllen, K. and Fasel, R. Self-Assembly of chiral molecular honeycomb networks on Au(111). *J. Am. Chem. Soc.* **130**, 8910–8912 (2008).

[159] Meier, C., Roos, M., Künzel, D., Breitruck, A., Hoster, H. E., Landfester, K., Gross, A., Behm, R. J. and Ziener, U. Concentration and coverage dependent adlayer structures: from two-dimensional networks to rotation in a bearing. *J. Phys. Chem. C* **114**, 1268–1277 (2010).

[160] Lei, S. B., Tahara, K., De Schryver, F. C., Van der Auweraer, M., Tobe, Y. and De Feyter, S. One building block, two different supramolecular surface-confined patterns: concentration in control at the solid-liquid interface. *Angew. Chem., Int. Ed.* **47**, 2964–2968 (2008).

[161] Uemura, T., Aono, M., Komatsu, T. and Kunitake, M. Two-dimensional self-assembled structures of melamine and melem at the aqueous solution-Au(111) interface. *Langmuir* **27**, 1336–1340 (2011).

[162] Wan, S., Guo, J., Kim, J., Ihee, H. and Jiang, D. L. A belt-shaped, blue luminescent, and semiconducting covalent organic framework. *Angew. Chem., Int. Ed.* **47**, 8826–8830 (2008).

[163] Dienstmaier, J. F., Medina, D. D., Dogru, M., Knochel, P., Bein, T., Heckl, W. M. and Lackinger, M. Isoreticular two-dimensional covalent organic frameworks synthesizedby on-surface condensation of diboronic acids. *ACS Nano* **6**, 7234–7242 (2012).

[164] Guan, C. Z., Wang, D. and Wan, L. J. Construction and repair of highly ordered 2D covalent networks bychemical equilibrium regulation. *Chem. Commun.* **48**, 2943–2945 (2012).

[165] Bieri, M. *et al.* Porous graphenes: two-dimensional polymer synthesis with atomic precision. *Chem. Commun.* 6919–6921 (2009).

[166] Lin, V. S. Y., Radu, D. R., Han, M. K., Deng, W. H., Kuroki, S., Shanks, B. H. and Pruski, M. Oxidative polymerization of 1,4-diethynylbenzene into highly conjugated poly(phenylene butadiynylene) within the channels of surface-functionalized mesoporous silica and alumina materials. *J. Am. Chem. Soc.* **124**, 9040–9041 (2002).

[167] Suzuki, H., Yamada, T., Kamikado, T., Okuno, Y. and Mashiko, S. Deposition of thermally unstable molecules with the spray-jet technique on Au(111) surface. *J. Phys. Chem. B* **109**, 13296–13300 (2005).

[168] Weiss, H. C., Blaser, D., Boese, R., Doughan, B. M. and Haley, M. M. C-H$\cdots\pi$ interactions in ethynylbenzenes: the crystal structures of ethynylbenzene and 1,3,5-triethynylbenzene, and a redetermination of the structure of 1,4-diethynylbenzene. *Chem. Commun.* 1703–1704 (1997).

[169] Robinson, J. M. A., Kariuki, B. M., Harris, K. D. M. and Philp, D. Interchangeability of halogen and ethynyl substituents in the solid state structures of di- and tri-substituted benzenes. *J. Chem. Soc., Perkin Trans. 2* 2459–2469 (1998).

[170] Sohn, Y., Wei, W. and White, J. M. Phenylacetylene on Cu(111): adsorption geometry, interfacial electronic structures and thermal chemistry. *J. Phys. Chem. C* **111**, 5101–5110 (2007).

[171] Lipton-Duffin, J. A., Ivasenko, O., Perepichka, D. F. and Rosei, F. Synthesis of polyphenylene molecular wires by surface-confined polymerization. *Small* **5**, 592–597 (2009).

[172] Tang, B. Z. Construction of functional polymers from acetylenic triple-bond building blocks. *Macromol. Chem. Phys.* **209**, 1304–1307 (2008).

[173] Kanuru, V. K., Kyriakou, G., Beaumont, S. K., Papageorgiou, A. C., Watson, D. J. and Lambert, R. M. Sonogashira coupling on an extended gold surface *in vacuo*: reaction of phenylacetylene with iodobenzene on Au(111). *J. Am. Chem. Soc.* **132**, 8081–8086 (2010).

[174] Frisch, M. J. *et al.* Gaussian 03 (2004).

[175] Gourdon, A. On-surface covalent coupling in ultrahigh vacuum. *Angew. Chem., Int. Ed.* **47**, 6950–6953 (2008).

[176] Martin-Gago, J. A. POLYCYCLIC AROMATICS On-surface molecular engineering. *Nat. Chem.* **3**, 11–12 (2011).

[177] Ourdjini, O. *et al.* Substrate-mediated ordering and defect analysis of a surface covalent organic framework. *Phys. Rev. B* **84**, 125421 (2011).

[178] Gao, H.-Y., Franke, J.-H., Wagner, H., Zhong, D., Held, P.-A., Studer, A. and Fuchs, H. Effect of metal surfaces in on-surface Glaser coupling. *J. Phys. Chem. C* **117**, 18595–18602 (2013).

[179] Fan, Q., Wang, C., Han, Y., Zhu, J., Kuttner, J., Hilt, G. and Gottfried, J. M. Surface-assisted formation, assembly, and dynamics of planar organometallic macrocycles and zigzag shaped polymer chains with C–Cu–C Bonds. *ACS Nano* **8**, 709–718 (2013).

[180] Eder, G., Smith, E. F., Cebula, I., Heckl, W. M., Beton, P. H. and Lackinger, M. Solution preparation of two-dimensional covalently linked networks by polymerization of 1,3,5-tri(4-iodophenyl)benzene on Au(111). *ACS Nano* **7**, 3014–3021 (2013).

[181] Russell, J. C., Blunt, M. O., Garfitt, J. M., Scurr, D. J., Alexander, M., Champness, N. R. and Beton, P. H. Dimerization of tri(4-bromophenyl)benzene by Aryl-Aryl coupling from solution on a gold Surface. *J. Am. Chem. Soc.* **133**, 4220–4223 (2011).

[182] Lipton-Duffin, J. A., Miwa, J. A., Kondratenko, M., Cicoira, F., Sumpter, B. G., Meunier, V., Perepichka, D. F. and Rosei, F. Step-by-step growth of epitaxially aligned polythiophene by surface-confined reaction. *Proc. Natl. Acad. Sci.* **107**, 11200–11204 (2010).

[183] Plekan, O., Feyer, V., Tsud, N., Vondrácek, M., Cháb, V., Matolín, V. and Prince, K. Adsorption of 5-halouracils on Au(111). *Surf. Sci.* **606**, 435–443 (2012).

[184] Ziegler, K. Über Ringschluß-Reaktionen. *Berichte der deutschen chemischen Gesellschaft (A and B Series)* **67**, 139–149 (1934).

[185] Lin, T., Shang, X. S., Adisoejoso, J., Liu, P. N. and Lin, N. Steering on-surface polymerization with metal-directed template. *J. Am. Chem. Soc.* **135**, 3576–3582 (2013).

[186] Villagómez, C. J., Sasaki, T., Tour, J. M. and Grill, L. Bottom-up assembly of molecular wagons on a surface. *J. Am. Chem. Soc.* **132**, 16848–16854 (2010).

[187] Wu, Y.-J., Wang, W.-H. and Chiang, C.-M. Identification of surface allenyl and its transformation into propargyl with C_3H_3Br adsorption by RAIRS on Ag(111). *Langmuir* **18**, 1449–1452 (2002).

[188] Castro, M. E., Pressley, L. A., Kiss, J., Pylant, E. D., Jo, S. K., Zhou, X. L. and White, J. M. Adsorption and decomposition of trifluoroiodomethane on clean and iodine-precovered silver(111). *J. Phys. Chem.* **97**, 8476–8484 (1993).

[189] Bushell, J., Carley, A. F., Coughlin, M., Davies, P. R., Edwards, D., Morgan, D. J. and Parsons, M. The reactive chemisorption of alkyl iodides at Cu(110) and Ag(111) surfaces: a combined STM and XPS study. *J. Phys. Chem. B* **109**, 9556–9566 (2005).

[190] Di Giovannantonio, M. *et al.* Reply to "Comment on 'Insight into organometallic intermediate and its evolution to covalent bonding in surface-confined Ullmann polymerization'". *ACS Nano* **8**, 1969–1971 (2014).

Publications

1. On-surface Ullmann polymerization *via* intermediate organometallic networks on Ag(111)

   J. Eichhorn, T. Strunskus, A. Rastgoo-Lahrood, D. Samanta, M. Schmittel, and M. Lackinger, *Chem. Commun.* 50, 7680-7682, 2014.

2. On-surface Ullmann coupling: the influence of kinetic reaction parameters on the morphology and quality of covalent networks

   J. Eichhorn, D. Nieckarz, O. Ochs, D. Samanta, M. Schmittel, P. Szabelski, and M. Lackinger, *ACS Nano* 8(8), 7880-7889, 2014.

3. From benzenetrithiolate self-assembly to copper sulfide adlayers on Cu(111): temperature-induced irreversible and reversible phase transitions

   T. Sirtl, M. Lischka, J. Eichhorn, A. Rastgoo-Lahrood, T. Strunskus, W. M. Heckl, and M. Lackinger, *J. Phys. Chem. C* 118(7), 3590-3598, 2014.

4. On-surface polymerization of 1,4-diethynylbenzene on Cu(111)

   J. Eichhorn, W. M. Heckl, and M. Lackinger, *Chem. Commun.* 49, 2900-2902, 2013.

5. Synthesis of two-dimensional phenylene-boroxine networks through *in vacuo* condensation and on-surface radical addition

   S. Schlögl, T. Sirtl, J. Eichhorn, W. M. Heckl, and M. Lackinger, *Chem. Commun.* 47, 12355-12357, 2011.

6. Self-assembly of melem on Ag(111) - emergence of porous structures based on amino-heptazine hydrogen bonds

   J. Eichhorn, S. Schlögl, B. V. Lotsch, W. Schnick, W. M. Heckl, and M. Lackinger, *CrystEngComm* 13(18), 5559-5565, 2011.